Tuning apico-basal polarity and junctional recycling in the hemogenic endothelium orchestrates pre-hematopoietic stem cell emergence complexity

Léa Torcq,[1,2] Sara Majello,[1] Catherine Vivier,[1] and Anne A. Schmidt [1,6,*]

[1] Institut Pasteur, Université Paris Cité, CNRS UMR3738, Department of Developmental and Stem Cell Biology, F-75015 Paris, France

[2] Sorbonne Université, Collège doctoral, F-75005 Paris, France

[6] Lead contact

* Correspondence: anne.schmidt@pasteur.fr

Abstract

Hematopoietic stem cells emerge in the embryo from an aortic-derived tissue called the hemogenic endothelium (HE). The HE appears to give birth to cells of different nature and fate but the molecular principles underlying this complexity are largely unknown. Here we show, in the zebrafish embryo, that two cell types emerge from the aortic floor with radically different morphodynamics. With the support of live imaging, we bring evidence suggesting that the mechanics underlying the two emergence types rely, or not, on apicobasal polarity establishment. While the first type is characterized by reinforcement of apicobasal polarity and maintenance of the apical/luminal membrane until release, the second type emerges via a dynamic process reminiscent of trans-endothelial migration. Interfering with Runx1 function suggests that the balance between the two emergence types depends on tuning apicobasal polarity at the level of the HE. In addition, using new transgenic fish lines that express Junctional Adhesion Molecules and functional interference, we bring evidence for the essential role of ArhGEF11/PDZ-RhoGEF in controlling the HE-endothelial cell dynamic interface, including cell-cell intercalation, which is ultimately required for emergence completion. Overall, we highlight critical cellular and dynamic events of the endothelial-to-hematopoietic transition that support emergence complexity, with a potential impact on cell fate.

Major subject areas: Developmental Biology and Stem cells, Cell Biology.

Keywords: hematopoiesis, stem cell, cell extrusion, endothelial-to-hematopoietic transition, apico-basal polarity, hemogenic endothelium, tight junctions, JAMs, zebrafish.

36 ## Introduction

37

38 Hematopoietic stem cells (HSCs) endowed with full regenerative potential in adult vertebrates
39 are generated during a narrow-time window of few days during embryonic development. These
40 cells, at the root of all blood and immune cells in the body, emerge from intra-embryonic aortic
41 vessels and, more specifically, from a specialized type of vascular tissue called the hemogenic
42 endothelium (HE, (Wu and Hirschi 2021)). A series of seminal studies have evidenced the
43 autonomous production of repopulating HSCs within an intraembryonic region called the Aorta-
44 Gonad-Mesonephros (AGM), before their appearance in other hematopoietic organs (A. L.
45 Medvinsky et al. 1993; Müller et al. 1994; Garcia-Porrero, Godin, and Dieterlen-Lièvre 1995;
46 A. Medvinsky and Dzierzak 1996; Cumano, Dieterlen-Lievre, and Godin 1996). Thereafter, the
47 endothelial origin of HSCs was evidenced (Jaffredo et al. 1998; de Bruijn et al. 2002; T. E.
48 North et al. 2002). The direct visualization, in real-time, of the emergence of precursors of
49 hematopoietic stem and progenitor cells (HSPCs) from the dorsal aorta, termed the
50 Endothelial-to-Hematopoietic Transition (EHT), was finally achieved *in vitro* (Eilken, Nishikawa,
51 and Schroeder 2009), *ex-vivo* from mouse sections (Boisset et al. 2010), and *in vivo* in the
52 zebrafish embryo (Bertrand et al. 2010; Kissa and Herbomel 2010), using live microscopy. This
53 opened the way to a more detailed analysis of the characteristics of the HE at the
54 transcriptional level, revealing its transient nature and its early hematopoietic commitment
55 (Swiers et al. 2013).

56 The HE is characterized by inherent heterogeneity and is not only contributing to the formation
57 of precursors to long-term HSCs (pre-HSCs) but also to more restricted progenitors (Hadland
58 and Yoshimoto 2018). These progenitors can be born from HE sub-types that are found in
59 extra-embryonic source such as the yolk-sac – in which case it gives rise to erythro-myeloid
60 progenitors that will sustain erythro-myelopoiesis until birth (Frame et al. 2016) -, or both from
61 extra and intra-embryonic sources (the yolk sac and the dorsal aorta) in which cases

62 progenitors are biased, such as for example in the mouse, toward T- and B- innate-type
63 lymphoid progenitors (Yoshimoto et al. 2011; 2012) or toward less restricted, multipotent
64 progenitors (Hadland and Yoshimoto 2018; Dignum et al. 2021). Importantly, while some of
65 the non-HSC derived progenitors born during embryonic life only support the functions of the
66 immune system during embryonic/ fetal life, others can persist in the adult to exert tissue-
67 resident functions, as has been mainly described in the mouse (Ghosn et al. 2019). However,
68 studies in human embryos support the idea that developmental hematopoiesis is highly similar
69 in mice and humans (Ivanovs et al. 2011; 2017).
70 A key question regarding the issue of the capacity of the HE to give birth to cells endowed with
71 different hematopoietic potential is whether this comes from HE cells of distinct origin (in which
72 case the HE would be a mosaic of precursors with distinct potential) or if this results from
73 extrinsic environmental cues that impose variability in the constantly evolving developmental
74 context (for a discussion, see (Barone et al. 2022)).
75 To address this type of question, high-resolution experimental settings need to be developed,
76 if possible at the single-cell resolution. Along this line, recent developments of transcriptomics,
77 including single cell RNAseq, spatially resolved in situ transcriptomic approaches, and in situ
78 barcoding, have been invaluable (Weijts, Yvernogeau, and Robin 2021). Among those high-
79 resolution approaches, cell fate mapping and lineage tracing approaches that include imaging
80 technologies have been very instrumental, particularly when performed with the zebrafish
81 model that reproduces many aspects of developmental hematopoiesis in higher vertebrates
82 (Orkin and Zon 2008). Recently, work performed in the zebrafish embryo has brought evidence
83 for heterogeneity of hematopoietic stem cell precursors being born from the HE, in the ventral
84 floor of the dorsal aorta and independently from HSCs, including a wave of transient T-
85 lymphocytes (using temporally-spatially resolved fate-mapping, (Tian et al. 2017)) and lympho-
86 myeloid biased progenitors born from a myeloid-lymphoid biased Spi2+ HE that appears to co-
87 exist with an erythroid-biased HE (using single-cell RNA-sequencing, (Xia et al. 2023)).

88 While light starts to be shed on the molecular and signaling cues that appear to regulate HE
89 sub-specification and a continuum from arterial endothelium, HE maturation, and subsequent
90 heterogeneity in HSPCs (Zhu et al. 2020), the essential molecular and cell biological properties
91 that support HE functional plasticity remain to be determined.

92 Here, using the zebrafish embryo as a model, we complement our previous work describing
93 essential molecular and mechanistic features of EHT cell emergence (Lancino et al. 2018).
94 With the support of high-resolution live imaging and image analysis, the generation of new
95 transgenic fish lines that express functional markers of cell polarity (podocalyxin) and of inter-
96 cellular adhesion (Junctional Adhesion Molecules - JAMs), as well as functional and genetic
97 interference, we bring insight into additional key features of the EHT process that take their
98 root in the differentiation and maturation of the HE.

99 # Results

100

101 **Apicobasal polarity determines emergence types**

102 Our previous work describing the morphodynamic evolution of cells emerging from the aortic
103 floor through the EHT (hereafter designated as "EHT cells"), in the zebrafish embryo, revealed
104 the unusual feature of a cell extruding from the plane of a tissue while maintaining its
105 luminal/apical membrane until the very end of the release process, thus contributing to its
106 peculiar crescent-shaped morphology (Kissa and Herbomel 2010; Lancino et al. 2018, and
107 see the cartoons in ***Figure 1A***). However, to our knowledge, the polarity status of EHT cells
108 has not been investigated so far and the maintenance of a *bona fide* apical domain has never
109 been proven (with the luminal membrane enriched in apically targeted proteins and physically
110 delimited by apical polarity factors and tight junction complexes (Rodriguez-Boulan, Müsch,
111 and Le Bivic 2004; Buckley and St Johnston 2022)). Importantly, the fate of this apical-luminal
112 membrane, after the release, may lead to cells potentially endowed with specific functional
113 features. For example, this membrane surface may be directly and fully exposed to the
114 extracellular space or released in the cytoplasm of EHT cells for recycling and/or degradation,
115 after emergence completion (for examples of different scenarios, see ***Figure 1A***). Overall, this
116 could lead to precursors of hematopoietic stem cells that, ultimately, may be differentially fated.
117 To address the polarity status of EHT cells, we raised transgenic fish lines that express
118 endogenous Podocalyxin (Podxl2, (Herwig et al. 2011)), a sialomucin of the CD34 family
119 (Nielsen and McNagny 2008). Podocalyxin was shown to take part in the formation of the
120 preapical domain during polarization and in the regulation of its oriented organization, in tissue
121 culture (Meder et al. 2005; Bryant et al. 2014). Its contribution to lumenization *in vivo*, in the
122 mouse aorta, has been described and it involves negative charge repulsion induced by their
123 glycosyl residues (Strilić et al. 2009; 2010).

124 We first attempted to express transiently, in the vascular system, the full-length Podxl2
125 zebrafish protein fused to eGFP at its extreme N-terminus. We failed to detect the fusion
126 protein at any time point relevant for observing easily the EHT process (a time window ranging
127 from 48 to 60 hpf (hours post-fertilization)); therefore we designed a N-ter truncated form
128 deleted of the mucin domain and that retains amino-acids 341-587 fused to eGFP at its N-
129 terminus (***Figure 1B*** *and see* ***Materials and Methods***). Transient transgenesis revealed that
130 this truncated version is detected and is targeted to the luminal membranes of EHT cells. We
131 then raised 2 transgenic (*Tg*) fish lines that express the N-ter truncated form of Podxl2 fused
132 to either eGFP (thereafter abbreviated eGFP-Podxl2) and under the control of the Kdrl:Gal4
133 driver (*Tg(Kdrl:Gal4;UAS:RFP; 4xNR:eGFP-Podxl2)*), or to mKate2 and under the control of
134 the Kdrl promoter (*Tg(Kdrl:mKate2-Podxl2))*. We observed that eGFP-Podxl2 is enriched at
135 the luminal side of crescent-shaped EHT undergoing cells (see ***Figure 1C, Figure 1 - figure***
136 ***supplement 1A*** and ***Figure 1 – video 1*** (z-stack at t=0) and their legends for the details of the
137 luminal/apical membrane evolution through time). Thereafter, these cells will be referred to as
138 EHT pol+ cells.
139 We also followed the cell after emergence and observed the evolution of the luminal/apical
140 membrane appearing as internal pseudo-vacuoles. We illustrate the reduction of their volume
141 via membrane retrieval and, ultimately, their remanence as an intracellular membrane
142 compartment which we define as a post-EHT signature (***Figure 1- figure supplement 1A*** and
143 ***Figure 1- video 2*** (z-stack at t=80 min)); we propose a model for the intracellular evolution of
144 the luminal/apical membrane which, unfortunately, cannot be traced after 2-3 hrs post-
145 emergence because of the apparent short half-life of eGFP-Podxl2 and of the drop in activity
146 of the Kdrl promoter (***Figure 1- figure supplement 1B***). Of notice, the pseudo-vacuoles are
147 reminiscent of the cystic formations observed in EHT cells in the mouse and visualized by
148 electron-microscopy (T. North et al. 1999; Marshall and Thrasher 2001) and also of the
149 vacuolar structures recently described in EHT cells in avian embryos (Sato et al. 2023); in both
150 cases, these vacuoles appear to emanate from the abluminal membrane (facing the sub-aortic

151 space) and not from the lumen. In the latter case, they disappear before EHT completion,
152 suggesting that they contribute to exert mechanical force to initiate the detachment of the cell
153 from the endothelial layer. In addition, their dynamics appears to depend on the activity of
154 aquaporins and it is very possible that aquaporins are active in zebrafish too, although rather
155 in EHT cells late in their emergence and/or in post-EHT cells, for water chase and vacuolar
156 regression as proposed in our model (***Figure 1 – figure supplement 1B***).

157 While imaging the EHT using the Podxl2 expressing lines that clearly delimitate the luminal
158 membrane, we unambiguously identified a second type of emergence. This second cell type
159 is primarily characterized by a round-to-ovoid morphology (cells never bend as crescent-
160 shaped EHT pol+ cells, see ***Figure 1D*** and ***Figure 1 – video 3*** for a time-lapse sequence).
161 Importantly, these cells do not show any enrichment of eGFP-Podxl2 at the luminal membrane
162 and will be referred to as EHT pol- cells. EHT pol- cells were observed in all other *Tg* fish lines
163 that we are routinely imaging, including the *Tg(Kdrl:Gal4;UAS:RFP)* parental line that was used
164 for transgenesis, thus excluding the possibility that these cells result from an artefact due to
165 the expression of a deleted form of Podxl2 and/or to its overexpression.
166 Finally, we have estimated that the ratio between EHT pol+ and EHT pol- cells is of
167 approximately 2/1, irrespective of the imaging time window and of the localization of
168 emergence along the aortic antero-posterior axis (starting from the most anterior part of the
169 AGM (at the limit between the balled and the elongated yolk) down to the caudal part of the
170 aorta facing the CHT). We observed that both EHT pol+ and EHT pol- cells divide during the
171 emergence and remain with their respective morphological characteristics after completing
172 abscission (hence appearing as pairs of cells that exit the aortic wall sequentially, as shown
173 ***Figure 1C, D***). We also observed that both EHT pol+ and EHT pol- cells express reporters
174 driven by the hematopoietic marker CD41 (data not shown), which indicates that they are both
175 endowed with hematopoietic potential.

176 Altogether, our results show that hemogenic cells emerging from the aortic floor do so with
177 heterogeneity in their morphodynamic characteristics. This suggests that this may be one of
178 the sources underlying the complexity of pre-hematopoietic stem cell identity and of their
179 downstream cell fate.

180

181 **The immature HE is not polarized**

182 EHT pol+ and EHT pol- cells appear to emerge from the hemogenic endothelium (HE), the
183 latter constituting the virtually exclusive cell population of the aortic floor just prior to the
184 initiation of the EHT time-window (around 28 hpf, see (Zhao et al. 2022)). In this context, we
185 addressed the polarity status of HE cells. Surprisingly, confocal microscopy using the *eGFP-*
186 *Podxl2* expressing fish line revealed that HE cells do not appear to be polarized, based on the
187 absence of eGFP-Podxl2 enrichment at luminal membranes, at the initiation of the EHT time-
188 window (at approximately 28 - 30 hpf, ***Figure 2 – figure supplement 1***). Interestingly, the
189 cytoplasm of characteristic elongated HE cells located on the aortic floor is filled with more-or-
190 less large membrane vesicles that carry eGFP-Podxl2 (the largest vesicles reaching
191 approximately 30μm in diameter). This suggests that HE cells contain a reservoir of eGFP-
192 Podxl2 membranes that may be subjected to exocytose; as such, HE cells may be comparable
193 to endothelial cells organizing a vascular lumen and that have been proposed to exocytose
194 large intracellular macropinocytic-like vacuoles when cultured in 3D extracellular matrices
195 (Bayless and Davis 2002; Davis, Bayless, and Mavila 2002) or, *in vivo*, in the zebrafish model
196 (Kamei et al. 2006; Lagendijk, Yap, and Hogan 2014). This finding is unexpected since HE
197 cells are assumed to possess aortic cell characteristics (i.e exhibit an apicobasal polarity) as
198 they are supposedly integrated in the aortic wall contemporarily to aortic precursors (Jin et al.
199 2005) and may have been taking part in the lumenization of the ancestral vascular cord, a
200 process that takes place around 18-20 hpf. Consequently, loss of apicobasal polarity features
201 of HE cells at 28-30 hpf may be part of the programme that initiates the EHT process.

202 Although technically difficult for long hours (because of important variations in the volume of
203 the balled yolk that trigger drifting of embryos), we have been able to follow through time non-
204 polarized HE cells and to visualize the evolution of their vesicular content, starting at the
205 initiation of the EHT time-window (around 35 hpf, see ***Figure 2*** and ***Figure 2 – figure***
206 ***supplement 2***). Interestingly, we could follow a dividing HE cell for which the vesicular content
207 labelled with the polarity marker Podxl2 (eGFP-Podxl2) appeared to partition unequally
208 between daughter cells (***Figure 2A,*** EHT cell 1' inherits the largest macropinocytic-like vacuole
209 and emerges unambiguously as an EHT pol+ cell). This suggests that asymmetric inheritance
210 of cytosolic vesicles containing apical proteins may contribute, presumably after delivery to the
211 luminal membrane, to the acquisition of apicobasal polarity by EHT pol+ cells.

212 Altogether, these results support the idea that the HE, at the initiation of the EHT time-window,
213 is not polarized. Subsequently, HE cells establish – or not – apicobasal polarity, thus leading
214 to the emergence of either EHT pol+ or EHT pol- cell types (see our model ***Figure 2B***). In the
215 case of EHT pol+ cells and while emergence is proceeding, apicobasal polarity is maintained
216 (if not reinforced) until the release.

217

218 **Tuning of apicobasal polarity is sensitive to interfering with the Runx1 transcription**
219 **factor and with blood flow**

220 To substantiate our findings on the significance of controlling apicobasal polarity establishment
221 on EHT sub-types, we explored the potential involvement of proteins of the Pard3 family; these
222 proteins, recruited by transmembrane receptors via their PSD-95/Dlg/ZO-1 (PDZ) domains
223 (Buckley and St Johnston 2022), are at the root of apicobasal polarity initiation and are
224 essential for the maintenance of apical membrane functional properties (Román-Fernández
225 and Bryant 2016). We anticipated that interfering directly with Pard3 proteins would hamper
226 the development of the aorta (in addition to other functions of polarized tissues that are
227 essential for embryonic development) and rather searched for correlative evidence for the

228 differential expression of Pard3 isoforms - including natural loss or gain of function variants -,
229 at critical time windows of the EHT process (i.e between 30-32 hpf (the timing at which the HE,
230 as we show, does not appear to be polarized) and 48-50 hpf (the timing at which, as we show,
231 part of HE cells have become competent to undergo emergence)). In addition, to provide
232 functional support to this analysis and ensure that differences relate to what is taking place in
233 hemogenic cells, our experimental conditions also included interfering with the gradual
234 maturation of the HE (we have estimated that HE cells represent approximately 30% of total
235 aortic cells at 48 hpf and others have estimated that they reach up to approximately 50% of
236 total aortic cells at 28 hpf (Zhao et al. 2022)). We altered the maturation of the HE by abrogating
237 blood flow and, more restricted to the EHT biological process *per se*, by interfering with the
238 function of the Runx1 transcription factor whose expression is sensitive to fluid sheer stress
239 (Adamo et al. 2009) and whose function is essential for EHT completion (Kissa and Herbomel
240 2010) and for regulating HSC number (Adamo et al. 2009; T. E. North et al. 2009).
241 Firstly, to reach these objectives, we sought to identify Pard3 isoforms that may be functionally
242 relevant during EHT progression, using whole-mount *in situ* hybridization (WISH), RT-PCR
243 and cloning. WISH performed at approximately 35 hpf allowed us to detect, in the aorta,
244 mRNAs encoding for all Pard3 members, including Pard3ab, b, ba and bb, with prominent
245 detection of Pard3ab and bb isoforms (see ***Figure 3A*** and ***Materials and Methods***).
246 Messenger RNAs, in the trunk region and encoding for all four isoforms, were also detected
247 by qRT-PCR during the 30-32 and 48-50 hpf time windows (data not shown). We also obtained
248 and cloned partial or complete cDNAs encoding for all four members after reverse transcription
249 of mRNAs expressed in the trunk region of 48 hpf embryos. Sequencing unveiled yet
250 unreferenced variants and, of relevance regarding our objectives, potential loss of function
251 proteins for Pard3ab and Pard3bb (see ***Figure 3B*** and ***Materials and Methods***); these
252 include, for Pard3ab, a deletion of most of the sequence but that retains the amino-terminus
253 containing the conserved region 1 (CR1) as well as the PDZ1 domain and, for Pard3bb, a

254 carboxy-terminal truncation of the PDZ3 domain that nonetheless maintains the carboxy-
255 terminal sequence of the protein (see ***Figure 3B*** and its legend for more details).

256 Secondly, to interfere with Runx1 function, we generated a *Tg* fish line that expresses a
257 truncated form of Runx1 (dt-runx1; fish line *Tg(Kdrl:Gal4;UAS:RFP;4xNR:dt-runx1-eGFP)*
258 thereafter abbreviated *Tg(dt-runx1)*) deleted from its transactivation domain and carboxy-
259 terminus but retaining its DNA-binding domain (the Runt domain (aa 55-183 (Kataoka et al.
260 2000; Burns et al. 2002; Kalev-Zylinska et al. 2002), see ***Figure 3C)***. Importantly, in this *Tg*
261 fish line, dt-runx1 expression is restricted to the vascular system, hence excluding expression
262 in the brain region that express Runx1 endogenously (see the aforementioned articles) and
263 preventing biases owing to potential interference with neuronal functions. In addition, owing to
264 the expression of eGFP concomitantly to dt-runx1 (eGFP is cleaved from dt-runx1 via a T2a
265 site for endopeptidase), this fish line allows for the easy selection of embryos for imaging and
266 for phenotypic analysis. In preliminary experiments aimed at addressing the localization of dt-
267 runx1 as well as its stability, we expressed it transiently and measured its proper targeting to
268 the nucleus, see ***Figure 3C)***.

269 To characterize further the *Tg(dt-runx1)* fish line, we performed time-lapse experiments using
270 spinning disk confocal microscopy (with some of the experiments addressing apicobasal
271 polarity performed with embryos obtained from outcrossing the *Tg(dt-runx1) and*
272 *Tg(Kdrl:mKate2-Podxl2)* fish lines). Overall, we made the following observations: (i)
273 hematopoiesis is affected, as attested by the significant increase in the number of
274 hematopoietic cells in the thymus, at 5 dpf (days post-fertilization), in comparison to control
275 siblings (***Figure 3- figure supplement 1***); (ii) at 30-32 hpf and contrarily to what we observed
276 with our fish lines expressing either eGFP-Podxl2 or mKate2-Podxl2, HE cells appear to be
277 polarized, based on enrichment of the polarity marker at luminal membranes. In addition, HE
278 cells do not appear to contain any visible intra-cytosolic Podxl2-containing vesicles (***Figure 3-***
279 ***figure supplement 2,*** compare with ***Figure 2 and Figure 2- figure supplement 1***); (iii) at 48-

280 55 hpf, we observe an accumulation of EHT pol+ cells both in the aortic floor and in the lateral
281 sides of the aortic wall as well as of cells of uncharacterized nature (the latter may,
282 hypothetically, represent EHT cells at an early phase of their emergence, including cells that
283 should have evolved as EHT pol- cells (see ***Figure 3 - figure supplement 3A***)); (iv)
284 occasionally, we observe - for EHT cells exhibiting invagination of the luminal membrane -,
285 scattered cytosolic and sub-plasmalemmal pools of Podxl2-containing membranes and,
286 consistently, the apparent decrease of Podxl2 enrichment at the apical/luminal membrane (see
287 ***Figure 3 - figure supplement 3B*** and compare with ***Figure 1C***). In addition and occasionally
288 as well, we observe the reversion of apparent EHT pol+ cells into apparent EHT pol- cells (data
289 not shown). These two last observations suggest that perturbing the tuning of apicobasal
290 polarity in the HE alters the morphodynamic characteristics of emergence types, particularly in
291 the case of EHT pol- cells whose biomechanical features appear to require turning down
292 apicobasal polarity establishment.
293 Altogether, the results obtained upon expression of dt-runx1 show impairment of
294 hematopoiesis and suggest that, for both EHT cell types, the progression throughout EHT is
295 perturbed, and so until the release. The accumulation of morphologically characterized EHT
296 pol+ like cells that we observe may result from the sustained apicobasal polarity of the HE at
297 early time points (around 30 hpf). Consistently, this appears to be detrimental to the emergence
298 of EHT pol- cells that we could not identify unambiguously and that may be part of the cells
299 that are of uncharacterized morphologically. In addition, our results suggest that precursors of
300 HE cells are polarized, as is expected to be the case for non-hemogenic aortic cells, and that
301 Runx1 is involved in controlling the molecular events that are tuning apico-basal polarity,
302 starting at the initiation of the EHT time-window.

303 We then pursued our aim to correlate, using qRT-PCR, the expression levels of Pard3 isoforms
304 with the apicobasal polarity status of the hemogenic tissue during the EHT critical time windows
305 (30-32 versus 48-50 hpf). To complement interference with Runx1 function upon expression

306 of dt-Runx1, we also prevented blood flow initiation using the well characterized *silent heart*
307 *(sih)* morpholino which inhibits the expression of cardiac troponin T (Sehnert et al. 2002).

308 In a first series of 3 independent experiments performed with cDNAs obtained from dissected
309 trunk regions of embryos at 30-32 and 48-50 hpf (***Figure 4A***), we measured the expression
310 levels of the four Pard3 isoforms using heterozygous *Tg(dt-runx1)* fishes that were incrossed
311 so as to obtain embryos expressing the highest possible amounts of dt-runx1, based on eGFP
312 fluorescence resulting from proteolytic cleavage of the dt-runx1-eGFP fusion. To validate the
313 efficiency of our interference conditions, we also measured expression levels of cmyb (an early
314 marker of hematopoiesis) and of Scrib (a polarity protein involved in the functional delimitation
315 of the cellular basal domain (Buckley and St Johnston 2022)). The qRT-PCR results show, for
316 all Pard3 isoforms, a reproducible tendency for opposite effects of dt-runx1 expression
317 between the 30-32 and 48-50 hpf time-windows, with the significant decrease of values for
318 Pard3ab and bb at 48-50 hpf in comparison to controls. This suggests that the expression
319 levels of Pard3 polarity proteins are differentially controlled between the two time-windows,
320 indicating that the expression level of Pard3 polarity proteins is positively controlled in the wild
321 type situation when emergence is proceeding at 48-50 hpf, but that it is rather negatively
322 controlled, and thus decreased, at early time points (during HE maturation, at 30-32 hpf).
323 These data and conclusions are also supported by results obtained with Scrib, with a
324 comparable outcome. Importantly, cmyb expression was significantly decreased for both time-
325 windows, consistently with the impairment in Runx1-dependent control of hematopoiesis.

326 In a second set of 3 independent experiments, we interfered with blood flow using the
327 *Tg(Kdrl:Gal4;UAS:RFP)* fish line after injection of the *sih* morpholino (MO) in 1 cell stage
328 embryos. We focused on Pard3ab and Pard3bb isoforms (***Figure 4B***). We reproduced the
329 results obtained for Pard3ab and Pard3bb upon dt-runx1 expression, with less variability and
330 consistently with the function of blood flow in controlling Runx1 expression (Adamo et al. 2009).

331 Finally, we also investigated expression levels of the +/- PDZ2 and +/- PDZ3 variants of
332 Pard3ab and Pard3bb, respectively (using, as for experiments reported in ***Figure 4B***,
333 incrosses of heterozygous *Tg(dt-runx1)* fishes, see ***Figure 4C -*** *left*). We found that, at 48-50
334 hpf and for both proteins, isoforms including the full-length PDZ domains are the most
335 decreased, hence being positively controlled in the wild type Runx1 context. This reinforces
336 the consistency of our findings as well as the importance of controlling expression levels of
337 fully active polarity proteins when emergence is proceeding. We also confirmed our results
338 using *sih* MO injections, at least for the Pard3ab +/-PDZ2 variants (***Figure 4C –*** *right).*
339 Interestingly, the ratios between the Pard3ab +/-PDZ2 variants are opposite between the 30-
340 32 hpf and 48-50 hpf time windows, reinforcing the idea of a fine tuning of apicobasal polarity
341 functions mediated by aortic environmental constraints imposed by blood flow.
342

343 **Junctional recycling is differentially controlled between EHT cell types**

344 To investigate the functional links between apicobasal polarity and the peculiarities of EHT
345 pol+ and EHT pol- emergence processes, we sought to follow the dynamics of Junctional
346 Adhesion Molecules (JAMs) that belong to tight junction complexes (Garrido-Urbani, Bradfield,
347 and Imhof 2014). During apicobasal polarity establishment in epithelial and endothelial tissues,
348 these molecules recruit the Pard3/aPKC complex, via a PDZ-binding peptide located at their
349 extreme carboxy-terminus (***Figure 5A*** and (Itoh et al. 2001; Ebnet et al. 2001; 2018)). In
350 addition, JAMs are expressed in the vascular system and, in relation to this work, JAM3b is
351 expressed in the aorta of the zebrafish embryo and promotes endothelial specification and
352 hematopoietic development (Kobayashi et al. 2020).
353 We envisaged a scenario whereby EHT pol+ cells, whose longitudinal interface with
354 endothelial neighbours shrinks along the X axis of the X, Y 2D-plane, may have less mobile
355 junctional pools than EHT pol- cells whose entire junctional interface moves along the X, Y, Z
356 3D-axes (***Figure 5 - figure supplement 1)***. In the case of EHT pol- cells, the consumption of

357 the junctional interface with adjoining endothelial cells appears to result from the converging
358 migration of endothelial neighbours crawling over the luminal membrane, based on
359 interpretation of our time-lapse sequences (***Figure 1- video 3***). In this context, we favoured
360 the analysis of junctional pools localized at antero-posterior sites of emerging cells as we have
361 shown that they are enriched with tight junction components (Lancino et al., 2018). In addition
362 and in the case of EHT pol+ cells, it is conceivable that these adhesion pools – spatially
363 restricted owing to apicobasal polarity –, contribute to anchoring the emerging cell in the 2D-
364 plane (***Figure 5 - figure supplement 1****).*

365 To achieve our goal, we designed 2 constructs in which eGFP is introduced in the extracellular
366 domains of the two JAM2a and JAM3b molecules (***Figure 5A***). To investigate their localization
367 and proper targeting at junctional interfaces, these constructs were expressed transiently and
368 ubiquitously, using the *Hsp70* heat shock promoter. We observed that the 2 fusion proteins
369 are efficiently targeted at cellular contacts and, more specifically, at the apical side of polarized
370 epithelia such as for example cells of the ependymal canal (***Figure 5 - figure supplement 2***).
371 We then established Tg fish lines expressing eGFP-Jam2a and eGFP-Jam3b under the control
372 of the vascular kdrl promoter (*Tg(kdrl:eGFP-Jam2a)* and *Tg(kdrl:eGFP-Jam3b)*). Using these
373 fish lines and spinning disk confocal microscopy, we observe a remarkable efficiency of
374 targeting to intercellular junctions, for both proteins (data not shown for eGFP-Jam2a; for
375 eGFP-Jam3b, see ***Figure 5B, C***). Deployment of the aortic wall into 2D cartographies allows
376 to point precisely at junctional pools established at the interface between endothelial and EHT
377 cells and emphasizes on the enrichment of eGFP-Jam3b at antero-posterior poles of EHT pol+
378 and EHT pol- cells (***Figure 5B, C*** *bottom*).

379 Using double transgenic *Tg(kdrl:eGFP-Jam3b; kdrl:nls-mKate2)* embryos at 48-55 hpf, we
380 addressed the recycling capacity of junctional pools using Fluorescence Recovery After
381 Photobleaching (FRAP). The labelling of nuclei with nls-mKate2 allowed to point at EHT pol+
382 and EHT pol- cells unambiguously because eGFP-Jam3b is essentially targeted to junctional

383 contours and not labelling peripheral membranes, except in few cases (and nuclei of EHT pol+
384 cells have a crescent shape, see ***Figure 6A***).
385 First and to set up our protocol, we spotted bi- and tri-junctional contacts between endothelial
386 cells (***Figure 6 – figure supplement 1***). Recycling parameters (fluorescence intensity
387 recovery with time and maximum recovery amplitude (that addresses the mobile pool), ***Figure***
388 ***6C***) showed that bi-junctional contacts are less mobile than tri-junctions, with a higher
389 dispersion of maximum recovery amplitude values for the latter (***Figure 6E***); this introduced a
390 clear limitation for statistical significance of the results, although clear tendencies were
391 observed for mean fluorescence intensity recovery ***(Figure 6C)*** and median values for
392 maximum recovery amplitude ***(Figure 6E)***. We then focused at antero-posterior sites of EHT
393 pol+ and EHT pol- cells and more specifically in the region of tricellular junctions (shared by 1
394 EHT cell and 2 endothelial neighbours, see ***Figure 6 – figure supplement 1***) that are clearly
395 the most enriched with eGFP-Jam3b. In each experiment, eGFP-Jam3b pools at tricellular
396 junctions between endothelial cells were also spotted for a comparative analysis.
397 Measurements of fluorescence recovery intensities revealed a significant increase in the
398 mobile fraction of eGFP-Jam3b at EHT pol+ – EC versus EHT pol- – EC junctional interfaces
399 (median values of 50% and 39% maximum recovery amplitudes after 10 min, respectively;
400 ***Figure 6E***)). Differences in recovery were also measured between EHT pol+ – EC and EHT
401 pol- – EC junctional interfaces when focusing on the earliest time points (the first 30 seconds,
402 ***Figure 6F***), although with smaller significance, with the median value of early recovery slopes
403 for the EHT pol+ - EC versus EHT pol- – EC junctional interfaces increased by 128% (***Figure***
404 ***6G***).
405 Altogether and unexpectedly regarding our initial scenario, these results indicate that tri-
406 junctional pools localized at antero-posterior poles of EHT cells and enriched with eGFP-
407 Jam3b molecules are significantly more dynamic for EHT pol+ cells in comparison to EHT pol-
408 cells. Since EHT pol+ cells - by virtue of apicobasal polarity establishment possibly assemble

409 an apical endosome -, this should favour the rapid recycling of eGFP-Jam molecules (Ebnet
410 et al. 2003). This recycling may entertain a certain rate of delivery of Pard3 proteins at apical
411 junctional regions and contribute to the maintenance/reinforcement of polarity throughout the
412 entire emergence process. In addition, this turnover may be adapted to the mechanical
413 tensions EHT pol+ cells are exposed to, in comparison to EHT pol- cells, owing to their specific
414 morphodynamic features (ex: cellular bending); these tensions may be sensed by tri-cellular
415 junctions which would be preferential sites for the renewal of junctional components whose
416 half-life is reduced owing to submission to mechanical forces.
417

418 **ArhGEF11/PDZ-Rho GEF plays essential functions during EHT progression**

419 Junctional maintenance and recycling are dependent on intracellular membrane trafficking,
420 supported by sub-cortical actin remodelling and actomyosin contractility, which are controlled
421 mainly by GTPases of the Rho family (Ridley 2006; Olayioye, Noll, and Hausser 2019). Owing
422 to the significance of apicobasal polarity control on EHT features, as suggested by our work,
423 we investigated which proteins may be essential for actin/actomyosin regulation and focused
424 on regulators of Rho GTPases, in particular Rho GEFs that catalyse exchange of GDP for GTP
425 to positively regulate their activity (Rossman, Der, and Sondek 2005). As for Pard3 proteins,
426 several of these Rho GEFs contain one or several PDZ domain(s) that target most proteins to
427 complexes acting at the apical side therefore interlinking actin/actomyosin regulation with cell
428 polarity (Mack and Georgiou 2014; Ebnet and Gerke 2022). We focused on 9 PDZ-domain
429 containing Rho GEFs, all encoded by different genes in the zebrafish (***Figure 7- figure***
430 ***supplement 1***): ArhGEF11/PDZ-RhoGEF (thereafter shortened as ArhGEF11), ArhGEF12a,
431 ArhGEF12b, PRex1, PRex2, Tiam1a, Tiam1b, Tima2a, Tiam2b. We first investigated their
432 expression by Whole mount In Situ Hybridization (WISH) and found that all 9 mRNAs are
433 detected in the aorta, and for the vast majority at 30-32 and 48-50 hpf (***Figure 7- figure***
434 ***supplement 2*)*.*** Then, using qRT-PCR (***Figure 7- figure supplement 1B***), we measured and

435 compared their expression levels in the trunk region (at 35 and 48 hpf), for dt-runx1 expressing
436 embryos and controls. We found that, in comparison to controls, ArhGEF11, ArhGEF12b,
437 Tiam1b and Tiam2a are significantly reduced upon dt-runx1 expression at 48 hpf (hence being
438 positively controlled in the wild type condition) and that their expression appears to be
439 oppositely controlled at 35 hpf; this mirrors the variations measured for polarity proteins
440 (***Figure 4***). This is consistent with a functional link between these Rho-GEFs and apicobasal
441 polarity control during EHT progression. We finally decided to focus on ArhGEF11 for the
442 following reasons: (i) in comparison to Tiams that act on Rac1, ArhGEF11 and ArhGEF12
443 (which are close relatives and can form heterodimers (Chikumi et al. 2004)), are mostly acting
444 on RhoA which is controlling apical constriction via the RhoA-Myosin II signalling axis; as we
445 have shown previously (Lancino et al. 2018), EHT progression requires the constriction of
446 circumferential actomyosin; (ii) ArhGEF11 was shown to regulate the integrity of epithelial
447 junctions by interacting directly with the scaffolding protein ZO-1, hence connecting inter-
448 cellular adhesion with RhoA-Myosin II (Itoh et al. 2012); (iii) ArhGEF11 mediated apical
449 constriction is essential during tissue morphogenesis such as, for example, the neural tube
450 formation in which epithelial cells, submitted to mediolateral contractile forces, constrict at their
451 apical side thus triggering inward bending of the neural plate which leads to the formation of
452 the neural tube (Nishimura, Honda, and Takeichi 2012). The EHT may share features with this
453 process, i.e the anisotropic distribution of contractile forces controlling the plane of emergence;
454 (iv) mammalian ArhGEF11 exhibits alternative splicing in its C-terminal region that controls
455 tight junction stability via the regulation of RhoA activity (Lee et al. 2018) as well as cell
456 migration and invasion (Itoh et al. 2017).
457 To confirm the potential function of ArhGEF11 at the junctional interface between HE/EHT and
458 endothelial cells, we first investigated its intracellular localization. We attempted to detect the
459 full-length form upon expression of a GFP fusion protein, in the vascular system, and failed to
460 do so. We then generated a truncated form that retains the N-terminal fragment encompassing
461 the PDZ and RGS domains (see ***Figure 7 – figure supplement 3A***) fused with eGFP in its C-

462 terminus. Upon transient expression in the vascular system, we visualized its localization at
463 the interface between endothelial and hemogenic cells progressing throughout the EHT, with
464 an apparent increase in density at antero-posterior regions between adjoining EHT cells
465 (***Figure 7 - figure supplement 3B***).

466 In line with the formerly described function of a splicing variant of ArhGEF11 in controlling tight
467 junction integrity, particularly during egression of cells from the skin epithelium in the mouse
468 (Lee et al. 2018), we questioned the potential role of such variant in EHT. This variant, referred
469 to as the mesenchymal form, results from the inclusion of a peptide encoded by exon 37 or
470 exon 38 in mouse and human, respectively (Shapiro et al. 2011; Itoh et al. 2017; Lee et al.
471 2018). This insertion locates in the degenerated C-terminal region of the protein, which is
472 predicted to be relatively poorly organized in its 3D structure. Upon amplifying the full-length
473 sequence of zebrafish ArhGEF11 for investigating its localization, we cloned fragments
474 encoding – or not – for the insertion of a peptide of 25 amino-acid residues (75 base pairs
475 corresponding to exon 38). Although variable when compared with other species (see ***Figure***
476 ***7 – figure supplement 4C,*** *bottom panel*), this peptide is inserted in the same region as it is
477 for mammals and may correspond to an ArhGEF11 variant functionally equivalent and involved
478 in the regulating of junctional stability (see ***Discussion***).

479 To investigate the function of ArhGEF11 on the junctional interface between HE/EHT and
480 endothelial cells, and more specifically of the isoform containing the exon 38 encoded peptide,
481 we used both morpholino (MO) and CRISPR-based strategies. We designed a splicing MO at
482 the 3-prime exon/intron boundary of exon 38 that interferes with its inclusion in the encoding
483 mRNA (***Figure 7 - figure supplement 4A***). This MO did not trigger any deleterious effect on
484 the gross morphology of zebrafish embryos (***Figure 7 – figure supplement 4B***) and blood
485 circulation was normal in comparison to control embryos. We attempted to generate CRISPR-
486 based genomic deletion mutants of exon 38, both using Cpf1 and Cas9 enzymes and failed
487 (see ***Materials and Methods***). However, using CRISPR/Cas9, we obtained a deletion mutant

488 triggering a frame shift downstream of exon 38 and introducing a premature stop codon few
489 amino-acid residues downstream thus leading to a sequence encoding for an ArhGEF11 C-
490 terminal deleted form (see ***Materials and Methods*** and ***Figure 7- figure supplement 4C***)).
491 Unlike the variant skipping exon 38 induced by the splicing MO, expression of the
492 CRISPR/Cas9 C-ter deletion mutant triggered, around 24 hpf, a severe retardation of blood
493 circulation initiation in approximately 80% of the embryos obtained from incrossing
494 ArhGEF11$^{CRISPR\text{-}Cterdel\text{-}/+}$ heterozygous mutant fishes. From 24 to 48 hpf, approximately 50% of
495 these embryos recovered a normal blood circulation (suggesting that these embryos are
496 probably heterozygous for the mutation), approximately 35% remained with a severe
497 phenotype (characterized by a large pericardiac oedema) and approximately 15% died, see
498 ***Figure 7 – figure supplement 4D*** and ***Materials and Methods***). This indicates essential
499 functions of the C-ter region of ArhGEF11, in agreement with previously published data on the
500 mammalian protein (Chikumi et al. 2004).

501 We then characterized more in depth the MO and CRISPR phenotypes and performed a
502 quantitative analysis of the number and morphology of HE, EHT and adjoining endothelial
503 cells, based on confocal images and subsequent segmentation of cell contours (using 2D
504 deployment of the aortic cylinder).

505 For the morphants, we found approximately a double amount of hemogenic cells in the aortic
506 floor (altogether localized on the floor and on the lateral sides of the aorta, see ***Figure 7A*** and
507 ***Figure 7 - figure supplement 5***); increase in the number of hemogenic cells also concerned
508 cells oriented more perpendicularly to the blood flow axis (toward the Y-axis, ***Figure 7Aa''***),
509 consistently with variation in emergence angle, as we have shown previously (Lancino et al.
510 2018). This is accompanied by a significant reduction in the number of morphologically
511 characterized EHT cells (***Figure 7A*** and ***Figure 7 – figure supplement 5***). Similar results
512 were obtained for the CRISPR homozygous deletion mutants, particularly regarding the
513 accumulation of hemogenic cells, although with a smaller amplitude (***Figure 7B*** and ***Figure 7***

514 ***- figure supplement 6***). Consistently, a significant increase in the aortic perimeter was found,
515 at least for the morphants (***Figure 7C***). Of notice also, hemogenic cells in morphants are on
516 average less elongated in comparison to control and to the CRISPR homozygous mutants (as
517 well as less dispersed according to this parameter), with the accumulation of a cell population
518 standing below the median value (***Figure 7Aa'''***; to some extent, this is reproduced as well
519 when measuring hemogenic cell area). Finally, the population of small cells in the morphants
520 are of uncharacterized morphology, which means that they appear neither as EHT pol+ nor as
521 EHT pol- cells and may represent abortive emergences (***Figure 7A*** and ***Figure 7 – figure***
522 ***supplement 5*** in which cellular morphology can be assessed from z-stacks).
523 Altogether, the morphants and CRISPR mutant phenotypes show that the progression
524 throughout EHT is significantly impaired supporting the idea that ArhGEF11 exerts important
525 functions in the process. Increase in the frequency of elongated cells for the CRISPR mutants
526 in comparison to morphants suggests that interference triggered by the C-ter deletion of
527 ArhGEF11 is more effective at early time points. Interference with inclusion of exon 38 in
528 morphants triggers an increase in the number of hemogenic cells of smaller area and reduced
529 elongation indicating a more efficient progression throughout emergence in comparison to the
530 CRISPR mutants, albeit with impairment at later stages. This may be due to alteration in the
531 dynamics of endothelial cell intercalation which is required for emergence completion (which
532 is also compatible with the accumulation of pairs of cells that may be post-mitotic and that do
533 not spread apart because this also requires aortic cell intercalation).
534

535 **ArhGEF11/PDZ-RhoGEF and its variant containing the exon 38 encoded sequence**
536 **control junctional dynamics to support reduction of the hemogenic/endothelial**
537 **interface and cell-cell intercalation**

538 To investigate how ArhGEF11 controls the dynamic interplay between HE/EHT and endothelial
539 cells, we characterized further the MO and CRISPR phenotypes, at the junctional level. To do

540 so, we performed FRAP experiments using the *Tg(Kdrl:eGFP-Jam3b)* fish line that was
541 injected at the one cell stage with the exon 38 splicing MO, or incrossing *(Kdrl:eGFP-Jam3b x*
542 ArhGEF11$^{CRISPR\text{-}Cterdel\text{-}/+}$) heterozygous fishes to obtaining homozygous mutants and wild type
543 alleles for control siblings.

544 FRAP experiments were focused on the hemogenic (HE)/endothelial (EC) membrane
545 interface, with the support of images obtained after 2D deployments of aortic segments (***Figure***
546 ***8A***). Pools of *eGFP-Jam3b* molecules localized at bi-junctional (HE-EC) and at tri-junctional
547 (HE-EC-EC and HE-HE-EC) interfaces were bleached and subsequently imaged for FRAP
548 analysis. In the case of the MO treatment (in which case HE cells accumulate on the aortic
549 floor (see ***Figure 7A*** and the 2D cartography of the aortic floor ***Figure 8A***)) we measured, in
550 comparison to control, an increase in FRAP recovery parameters for *eGFP-Jam3b* pools at
551 the tri-junctional HE-HE-EC interface (***Figure 8B***), which is the most significant for the recovery
552 speed at early time points (***Figure 8B, b'''***). Results are different for the ArhGEF11$^{CRISPR\text{-}}$
553 $^{Cterdel+/+}$ homozygous mutants for which we did not observe any obvious effect at HE-HE-EC tri-
554 junctions (***Figure 8C***) but, rather, a small tendency for an increase in the mobile pool at HE-
555 EC-EC tri-junctions (that has the particularity to concern 2 endothelial cells that contact the
556 longitudinal membrane of one HE cell, see ***Figure 8A, D***).

557 Altogether and including our results presented ***Figure 7***, these results reinforce the idea that
558 ArhGEF11 and its variant encoded by exon 38 are involved in critical steps of EHT progression,
559 partly by controlling the dynamics of junctional pools at the level of tri-junctions established
560 between adjoining hemogenic and endothelial cells (see the model ***Figure 8D*** and its legend
561 for a detailed analysis of mechanistic issues). The results also suggest that the +exon 38
562 peptide encoding variant is prominently involved in controlling the HE-HE-EC interface and
563 more specifically during intercalation, consistently with the accumulation, upon MO
564 interference, of EHT cells having progressed throughout the emergence but appearing to be
565 slowed down when reaching completion (cells of smaller area and less elongated, see ***Figure***

566 ***7***). Finally, ArhGEF11 is controlling RhoA and, most probably, its function in EHT progression
567 also involves actin and acto-myosin activities that are involved in the contraction of HE and
568 EHT cells (see Lancino et al. 2018; this is coupled with the consumption of longitudinal and
569 transversal membrane interfaces, see also the model ***Figure 8D*** and its legend).
570

571 # Discussion

572 **Characteristics of the HE and complexity of pre-hematopoietic stem cell emergence**
573 Heterogeneity in the identity and hematopoietic potential of cells emerging from the HE in the
574 AGM has been recently shown in co-culture systems and *in vivo* in the mouse (Ganuza et al.
575 2017; Dignum et al. 2021) and in the zebrafish model (Tian et al. 2017; Xia et al. 2023);
576 however, knowledge on the fundamental cell biological and molecular events leading to this
577 complexity is still lacking. Here, we highlight functional aspects that may significantly contribute
578 to this complexity and that take root in the cellular plasticity of the HE. We bring evidence
579 suggesting that HE cells that become competent to initiate the EHT time-window (around 28-
580 30 hpf) tune their apicobasal polarity status which endows them with the ability to support two
581 emergence processes with radically different morphodynamic characteristics; eventually, this
582 would lead to differentially fated cells, which remains to be determined.
583 While the ability of the HE to regulate its polarity features may be inherited from molecular
584 cues involved in its upstream intra-aortic specification (such as for example NOTCH (Robert-
585 Moreno et al. 2008; Gama-Norton et al. 2015; Bonkhofer et al. 2019), TGFβ (Monteiro et al.
586 2016), Gata2 (Butko et al. 2015; Daniel et al. 2019)), or any other of the more upstream factors
587 involved in hemogenic specification (Zhao et al. 2022)), our results suggest that Runx1 is
588 taking part in this regulation, consistently with its hematopoietic and EHT-inducing activity
589 (North et al. 1999; Kalev-Zylinska et al. 2002; Kissa and Herbomel 2010; Lancrin et al. 2012).
590 Our experiments using an interfering form of Runx1 (dt-Runx1) that produces a relatively weak
591 an subtle phenotype in comparison to morpholino treatment that prevents aortic cells to convert

592 into HE cells (Bonkhofer et al. 2019) or genetic mutation and gene knockout abrogating
593 hematopoiesis (T. E. North et al. 2009; Sood et al. 2010; Gao et al. 2018), provided the
594 opportunity to observe that, at 30 hpf, elongated HE cells on the aortic floor appear to be
595 maintained and to exhibit apicobasal polarity, with the absence of apparent cytosolic vacuolar
596 structures (as has been described in the mouse in Runx1 interfering condition (T. North et al.
597 1999)), which correlated with the subsequent accumulation of EHT pol+ cells that appeared to
598 be at the expense of EHT pol- cells. This is in favour of the idea that the two cell types arise
599 from a common precursor capable of evolving toward the one or the other, and that has lost
600 apicobasal polarity (see the model ***Figure 2B***). Recent work that has identified Runx1 targets
601 in the zebrafish embryo at 29 hpf does not point at any of the conventional apicobasal polarity
602 organizers as being direct targets although Pard3 and Pard6 mRNAs are clearly
603 downregulated in the HE in comparison to aortic roof cells (Bonkhofer et al. 2019) which is
604 consistent with our results at early time points of the EHT time-window.

605 A key question arising from our observations is what would control the balance orienting toward
606 an EHT pol+ or an EHT pol- type of emergence. Cell division may be orienting toward EHT
607 pol- emergence type (which would also be the reason why these cells have a round-shape
608 morphology in comparison to EHT pol + cells). The frequency of EHT pol+ versus EHT pol-
609 cells that we have estimated and that is of approximately 2/1 is not incompatible with this
610 possibility since divisions take place in the HE at a relatively high frequency. Indeed, it has
611 been estimated that 50% of HE cells that constitute the aortic floor at 28 hpf will divide and will
612 undergo emergence thereafter during the 28-72 hpf time window (Zhao et al. 2022). However,
613 we observe that both EHT pol+ and EHT pol- cells can divide during the emergence process
614 (see also our former work Lancino et al. 2018 for EHT pol+ cells), which is followed by the full-
615 recovery of their respective morphodynamic characteristics (not shown). Hence, this excludes
616 the possibility of a short term and purely mechanical effect of cell division on emergence
617 morphodynamics. In link with cell division however, there exist the possibility that the pool of

618 large vesicular structures potentially awaiting for exocytosis in HE cells having lost their
619 apicobasal polarity may become asymmetrically inherited after division. This would endow the
620 cell remaining with the largest pool to undergo EHT pol+ emergence after exocytosis and
621 expansion of the apical/luminal membrane. Our results ***Figure 2*** would support this possibility
622 but what controls this asymmetry would remain to be established.

623 Still, regarding the control of the balance orienting toward an EHT pol+ or an EHT pol- type of
624 emergence, the intrinsic nature of the HE, i.e. its acquaintance with the aortic differentiation
625 programme (Bonkhofer et al. 2019), raises the possibility of a partial recovery of an aortic cell
626 phenotype in the case of EHT pol+ emergence, thus supporting its very unique
627 mechanobiology. Therefore, the regulation of local signalling between aortic and HE cells may
628 tune the balance toward the one or the other fate; this could be the case, for example, for
629 adjoining HE cells in comparison to isolated ones that would then receive unequal signalling
630 cues owing to the difference in homotypic versus heterotypic contacting surfaces. In this
631 scenario, NOTCH signalling which is determinant for aortic and HE specification (Gama-Norton
632 et al. 2015) may play a significant role, particularly via the ratio of the Jag1/Dll4 ligands that is
633 fundamentally involved in HE versus aortic specification (Robert-Moreno et al. 2008;
634 Bonkhofer et al. 2019).

635 Finally, we cannot totally exclude that EHT pol+ and EHT pol- cells would originate from
636 different precursors. On this line, it has been shown that the aortic wall can home a transient
637 veinous-fated progenitor cell population that will lead to the underlying vein via selective
638 sprouting from 21 to 23 hpf (Herbert et al. 2009). This option would require a massive
639 expansion of a minor fraction of the cell population remaining in the aortic floor since it is
640 expected that most of it has been moving out toward the sub-aortic region, which is not in
641 favour of this possibility. In addition, recent scRNAseq analysis of floor and roof aortic cells at
642 21 and 28 hpf has led, for both timing points, to two well defined clusters defined only by aortic
643 and hematopoietic signatures (Zhao et al. 2022).

644

645 **The complexity of pre-HSC emergence and heterogeneity of hematopoietic stem cell**
646 **and progenitor populations**

647 Currently, we do not know what would be the features that would endow the two cell types to
648 behave differently after their release. Since post-EHT cells have to migrate in transient
649 developmental niches (i.e the CHT, the thymus, the pronephric region), these features may
650 provide them with more or less ability to migrate in the sub-aortic space and pass throughout
651 the wall of the underlying vein to conquest more distant niches (Murayama et al. 2006), or to
652 remain in a local AGM niche and be exposed to specific signalling there, in the proximity to the
653 aorta as it is the case for hematopoietic clusters in mammals and avians (Ciau-Uitz et al. 2014;
654 Jaffredo and Yvernogeau 2014). Beside their potential differences in colonizing different niches
655 which would impact on their subsequent fate, these cells may also contribute to more or less
656 transient waves of hematopoietic stem cells and progenitors that would be specific to the
657 developmental period such as, for example, a restricted sub-set of T-lymphocytes that was
658 described before (Tian et al. 2017). In the specific case of the Tian et al. work, the AGM was
659 shown to produces transient T-lymphocytes proposed to be independent of long-lived HSCs
660 according to a gradient that increases from the anterior to the posterior part of the trunk region,
661 as well as from the aorta in the tail (the posterior blood island in the tail region that was
662 proposed to give rise to hematopoietic precursors related to mammalian erythro-myeloid
663 progenitors, (Bertrand et al. 2007)). Since the EHT pol+ and EHT pol- cells that we describe in
664 our work are equally produced from the aorta in the trunk and in the tail regions (thus
665 irrespective of the antero-posterior axis of the aorta), the one or the other of the two EHT types
666 most probably does not directly relate to the first wave of T-lymphopoiesis arising from the
667 aortic endothelium described in Tian et al 2017.

668

669 **The cell biology behind emergence control and mechanics**

670 The intrinsic capacity of the HE, that we show here to be able to support two highly distinct
671 emergence processes, in the zebrafish embryo, is very unique. Indeed, not only are they taking
672 place contemporarily, but also can the two cell types proceed throughout emergence at a
673 distance shorter than 50 μm, which accommodates the intercalation of a single adjoining
674 endothelial cell. This may reflect the remarkable properties of the vascular system that needs
675 to allow cellular extrusion and transmigration. The latter is particularly relevant in the context
676 of developmental hematopoiesis since hematopoietic precursors that travel via blood
677 circulation need to pass throughout the aortic wall to conquest their distant niches.

678 In the present work, we provide some of the mechanistic insights into the specificities of the
679 two emergence types and that rely on two fundamental aspects of cellular biology, i.e
680 apicobasal polarity establishment and junctional mobility. The establishment and maintenance
681 of apicobasal polarity in a cell extruding from its environment, as is the case for EHT pol+ cells,
682 is at odds with the fundamental mechanisms of cell extrusion irrespective of the context into
683 which the process is taking place (Nieto et al. 2016; Gudipaty and Rosenblatt 2017; Pei et al.
684 2019; Staneva and Levayer 2023); this places the emergence of EHT pol+ cells as an extreme
685 case of extrusion and it is somehow unexpected to observe this type of emergence when the
686 aortic wall can extrude EHT pol- cells that appear to emerge contemporarily, apparently
687 according to a more conventional mode. During the EHT time-window, Runx1 is directly
688 controlling the emergence programme by regulating Rho-dependent cytoskeletal functions in
689 HE cells derived from mouse ES lines (Lie-A-Ling et al. 2014) and inducing the expression of
690 Gfi1ab in the zebrafish (Bonkhofer et al. 2019) that belongs to the family of transcriptional
691 repressors of the arterial programme expressed in the HE (Gfi1 and Gfi1b in the mouse,
692 (Lancrin et al. 2012)). This programme downregulates key molecules involved in the
693 maintenance of the aortic endothelium among which Cdh5 (VE-Cadh) and the downregulation
694 of cadherins is a hallmark of extrusion. Thus, for EHT cells, and particularly EHT pol+ cells,
695 downregulation of VE-Cadh should be compensated by other mechanisms that allow for the

696 maintenance of aortic integrity. In this context of adhesion downregulation, the JAMs (that are
697 expressed endogenously in the vascular system and that were used in this study) appear to
698 be a well-suited substitute. As part of tight junction complexes, they can strengthen adhesion
699 and, in addition, since they are also involved in cell migration (in particular leukocyte trans-
700 endothelial migration, see (Ebnet 2017)), they could in theory support the extrusion of EHT
701 pol- cells that do so according to a seemingly migration-type emergence mode (inferred from
702 our time-lapse sequences) more or less related to trans-endothelial migration. In the case of
703 EHT pol+ cells, we propose that JAMs may significantly contribute to the re-establishment of
704 apicobasal polarity and to the strengthening of adhesion while EHT pol+ cells should undergo
705 strong mechanical tension (owing to cellular bending). Interestingly, Jam3b appears to be a
706 direct and positively regulated target of Runx1 (Bonkhofer et al. 2019), which is supporting its
707 aforementioned potential functions during EHT.
708 Finally, regarding inter-cellular junctions and the control of their dynamics all along the EHT
709 process, we also addressed the dynamic interface between aortic and HE cells. As for EHT
710 cells, we focused more specifically on tri-junctional interfaces that have been proposed to
711 sense tension and transmit the information to other types of junctional complexes (Bosveld,
712 Wang, and Bellaïche 2018); in the EHT context, the contracting hemogenic endothelium is
713 additionally exposed to high mechanical tension owing to wall sheer stress imposed by the
714 blood flow and that was proposed to regulate emergence efficiency (Lundin et al. 2020;
715 Campinho et al. 2020; Chalin et al. 2021). In our work, we highlight one essential aspect of
716 controlling junctional recycling which is during cell-cell intercalation which concerns either
717 contacting HE cells lying on the aortic floor or HE/EHT cells after cytokinesis (as mentioned
718 before, cell division is rather frequent during the EHT time window (Zhao et al. 2022)). In this
719 context, we addressed the function of ArhGEF11/PDZ-RhoGEF which provides a functional
720 link between cell polarity (with its PDZ-binding motif and its RGS domain that couples to G-
721 protein coupled receptor signalling to regulate planar cell polarity (Nishimura, Honda, and
722 Takeichi 2012)), cell adhesion (it binds to the tight junction associated regulatory protein ZO-

723 1, (Itoh et al. 2012)), and cytoskeletal regulation/contraction (Itoh et al. 2012; Itoh 2013), all
724 three essential mechanistic components of morphogenetic movements and tissue remodelling.
725 Since morphodynamic events leading to cell extrusion and to the control of cell migration do
726 not only rely on the regulation of mRNAs levels but also on alternative splicing (Pradella et al.
727 2017) our interest for investigating the function of ArhGEF11 in EHT was raised by the fact that
728 the protein undergoes changes in its biological properties via the alternative splicing of a small
729 exon which leads to a modification of its C-terminus. We identified a splicing event in this region
730 (concerning exon 38) for a potential zebrafish isoform ortholog. However, the precise function
731 of this variant for the zebrafish protein, that was shown in the case of the mammalian isoform
732 to induce cell migration and motility (Itoh et al. 2017) and to bind to the Pak4 kinase thus
733 leading to the subsequent destabilization of tight junction complexes via loss of RhoA activation
734 (Lee et al. 2018), remains to be established. On this line, our results consistently indicate that
735 preventing exon 38 insertion interferes with EHT progression (as well as deleting the C-
736 terminus of the protein as shown with our CRISPR mutant) and appears to impair intercalation
737 of aortic cells between adjoining HE cells. Hence, the +exon 38 isoform, by regulating the
738 dynamic interplay between HE and endothelial cells, would favour one of the essential steps
739 of the EHT process leading to its completion and requiring the complete isolation of EHT cells
740 to ensure the ultimate sealing of the aortic floor (see our former work (Lancino et al. 2018)). It
741 remains to be established, as our measurements indicate, why the ArhGEF11 +exon 38
742 isoform appears to slow down junctional recycling which is counterintuitive with increasing the
743 HE/endothelial dynamic interface. However, upon interference, we have been following Jam3b
744 recycling which is only a sub-population of tight junction components that should be at play in
745 the system. Finally, the EHT process on its whole may be submitted to a complex regime of
746 alternating contraction and stabilization phases as we have shown previously in the context of
747 EHT pol+ emergence and that may reflect the necessity to adapt to mechanical constraints
748 imposed by the environment as well as the rearrangements of the HE/EHT/aortic cellular
749 interface (Lancino et al. 2018). In this context, back and forth regulatory mechanisms,

750 particularly involved in the control of the RhoA-Myosin II signalling axis partially regulated by
751 ArhGEF11, may locally and at specific timing points change the turnover of junctional
752 molecules, thus blurring the correlation between gross phenotype (here the organization of the
753 HE/aortic interface) and very local and dynamic molecular events (for a complement to the
754 discussion, see also the legend of the model presented ***Figure 8C***).

755 Overall, our work highlights the complexity of pre-hematopoietic stem cell emergence as well
756 as some of the essential molecular and mechanistic aspects involved. We show that the aorta,
757 in the zebrafish embryo, produces two fundamentally different types of EHT cells and propose
758 that this results from specific functional features of the HE regulated by the transcription factor
759 Runx1. This would support the production of cell types potentially endowed with different cell
760 fate potential, subsequently reinforced by the type of niche into which these cells will establish
761 homing. It now remains to be established if the different cell types that we describe are indeed
762 leading to cells that will eventually hold specific hematopoietic fate and properties.

763 # Materials and Methods

764 ## Key Resources Table

765 For the exhaustive list of all primers, see Materials and Methods - Supplementary Table.

Reagent type (species) or resource	Designation	Source or reference	Identifiers	Additional information
strain, strain background (zebrafish *Danio rerio*)	AB	Zebrafish International Resource Center (ZIRC)	ZFIN: ZDB-GENO-960809–7	
strain, strain background (zebrafish *Danio rerio*)	Tg(kdrl:HsHRAS -mCherry): s916Tg	(Chi et al. 2008)	ZFIN ID: ZDB-ALT-090506–2	referred to as Tg(kdrl:Ras-mCherry)
strain, strain background (zebrafish *Danio rerio*)	Tg(kdrl:nls-mKate2)	N/A	N/A	
strain, strain background (zebrafish *Danio rerio*)	Tg(kdrl:Gal4;UAS:RFP)	N/A	N/A	
strain, strain background (zebrafish *Danio rerio*)	Tg(kdrl:Gal4;UAS:RFP;4xNR:eGFP-Podxl2)	This paper	N/A	
strain, strain background (zebrafish *Danio rerio*)	Tg(kdrl:mKate2-Podxl2)	This paper	N/A	
strain, strain background (zebrafish *Danio rerio*)	Tg(kdrl:eGFP-Jam2a)	This paper	N/A	
strain, strain background (zebrafish *Danio rerio*)	Tg(kdrl:eGFP-Jam3b)	This paper	N/A	
strain, strain background (zebrafish *Danio rerio*)	Tg(kdrl:Gal4;UAS:RFP;4xNR:dt-runx1-eGFP)	This paper	N/A	
strain, strain background (zebrafish *Danio rerio*)	Tg(ArhGEF11$^{CRISPR\text{-}Cterdel\text{-}/+}$)	This paper	N/A	
recombinant DNA reagent	pG1-flk1-MCS-tol2	(Jin et al. 2005)	N/A	
recombinant DNA reagent	pEGFP-C1	Clontech	N/A	
recombinant DNA reagent	Transposase pCS-zT2TP	(Suster et al. 2011)	N/A	

Reagent type (species) or resource	Designation	Source or reference	Identifiers	Additional information
recombinant DNA reagent	pmKate2-f-mem	Evrogen	Cat# FP186	
antibody	goat anti-rabbit Alexa Fluor 488	Invitrogen	Cat# A11070	1/400
antibody	rabbit anti-GFP	MBL	Cat# 598	1/300
antibody	mouse anti-HA	Sigma	Cat# 12ca5	1/50
antibody	goat anti-mouse HRP-conjugated	Thermo Fisher Scientific	Cat# G-21040	1/300
sequence-based reagent	Morpholino sih	Sehnert et al., 2002	ZDB-MRPHLNO-060317-4	CATGTTTGCTCTGATCTGACACGCA
sequence-based reagent	Morpholino ArhGEF11 exon 38	This paper	N/A	GAAATAAATGAAGCCCCACCTCCGT
sequence-based reagent	Oligo for CRISPR: Alt-R® CRISPR-Cas12a (Cpf1) crRNAs -1	This paper	N/A	TATCACACACACATCACCTTCTA
sequence-based reagent	Oligo for CRISPR: Alt-R® CRISPR-Cas12a (Cpf1) crRNAs -2	This paper	N/A	TTTCTCAGCGCTCCTGACAGATG
sequence-based reagent	Oligo for CRISPR: Alt-R® CRISPR-Cas9 crRNAs	This paper	N/A	AGCCAATCGTCTGAGGACGG
sequence-based reagent	Oligo for CRISPR: Alt-R® tracrRNA	IDT	Cat# 1072532	
software, algorithm	CRISPRscan	(Moreno-Mateos et al. 2015)		N/A
software, algorithm	Zen Pro2 software	Zeiss	https://www.zeiss.com/microscopy/en/products/software/zeiss-zen.html	N/A
software, algorithm	QUANTSTUDIO™ DESIGN & ANALYSIS 2	Thermofisher	https://apps.thermofisher.com/apps/da2/	N/A
software, algorithm	MetaMorph software	Molecular Devices	https://www.moleculardevices.com/products/cellular-imaging-systems/acquisition-and-analysis-software/metamorph-microscopy	N/A
software, algorithm	Acquisition-Imaging analysis-LAS X	Leica	http://www.leica-microsystems.com	N/A
software, algorithm	Image Analysis-Fiji	NIH	https://imagej.net/Fiji	N/A

Reagent type (species) or resource	Designation	Source or reference	Identifiers	Additional information
software, algorithm	Image Analysis Icy	(de Chaumont et al., 2012)	http://icy.bioimageanalysis.org/	N/A
software, algorithm	Image Analysis TubeSkinner plugin for Icy	(Lancino et al. 2018)	https://icy.bioimageanalysis.org/plugin/tubeskinner/	N/A
software, algorithm	Figures-Illustrator CC 2017.1.1	Adobe	http://www.adobe.com/cn/	N/A
software, algorithm	Active contour plugin	(Dufour et al. 2010)	https://icy.bioimageanalysis.org/plugin/active-contours/	N/A
software, algorithm	NIS software	Nikon	https://www.microscope.healthcare.nikon.com/en_EU/products/software/nis-elements	N/A
software, algorithm	Rstudio	RStudio Team (2020)	http://www.rstudio.com/}	N/A
software, algorithm	ggplot2	(Wickham 2016)	https://ggplot2.tidyverse.org.	N/A
software, algorithm	readr	(Wickham, Hester, and Bryan 2022)	https://github.com/tidyverse/readr	N/A
software, algorithm	cowplot	(Wilke 2020)	https://wilkelab.org/cowplot/	N/A
software, algorithm	dplyr	(Wickham et al. 2023)	https://github.com/tidyverse/dplyr	N/A
software, algorithm	wesanderson	(Ram and Wickham 2018)	https://github.com/karthik/wesanderson	N/A
software, algorithm	matrixStats	(Ram and Wickham 2018)	https://github.com/HenrikBengtsson/matrixStats	N/A
software, algorithm	stringr	(Wickham 2022)	https://github.com/tidyverse/stringr	N/A
software, algorithm	ggsci	(Xiao N et al. 2023)	https://github.com/nanxstats/ggsci.	N/A
software, algorithm	ggpubr	(Kassambara et al. 2020)	https://rpkgs.datanovia.com/ggpubr/	N/A
software, algorithm	ggstatsplot	(Patil 2022)	https://indrajeetpatil.github.io/ggstatsplot/index.html	N/A
software, algorithm	ggbeeswarm	(Clarke and Sherrill-Mix 2017)	https://github.com/eclarke/ggbeeswarm	N/A
software, algorithm	DT	(Xie, Cheng, and Tan 2022)	https://github.com/rstudio/DT	N/A

Reagent type (species) or resource	Designation	Source or reference	Identifiers	Additional information
software, algorithm	SciViews	(Grosjean 2019)	https://www.sciviews.org/SciViews/	N/A
software, algorithm	nls.multstart	(Padfield and Matheson 2020)	https://github.com/padpadpadpad/nls.multstart	N/A

766

767

768 **Contact for reagent and resource sharing**

769 Further information and requests for resources and reagents should be directed to and will be
770 fulfilled by the corresponding Author, Anne A. Schmidt (anne.schmidt@pasteur.fr).

771 **Zebrafish husbandry**

772 Zebrafish (Danio rerio) of the AB background and transgenic fish carrying the following
773 transgenes *Tg(kdrl:ras-mCherry)* (Chi et al. 2008); *Tg(kdrl:nls-mKate2)*;
774 *Tg(kdrl:Gal4;UAS:RFP); and the fish lines generated in this study:*
775 *Tg(kdrl:Gal4;UAS:RFP;4xNR:eGFP-Podxl2); Tg(kdrl:mKate2-Podxl2); Tg(kdrl:eGFP-Jam2a);*
776 *Tg(kdrl:eGFP-Jam3b)*; *Tg(kdrl:Gal4;UAS:RFP;4xNR:dt-runx1-eGFP); Tg(ArhGEF11*$^{CRISPR\text{-}Cterdel\text{-}/+}$*)* were raised and staged as previously described (Kimmel et al. 1995). Adult fish lines
778 were maintained on a 14 hr light/10-hr dark cycle. Embryos were collected and raised at either
779 28.5 or 24°C in N-Phenylthiourea (PTU, Sigma Aldrich, Cat# P7629)/Volvic source water
780 (0.003% final) to prevent pigmentation complemented with 280 µg/L methylene blue (Sigma
781 Aldrich, Cat# M4159). Embryos used for imaging, extracting mRNA, or for WISH ranged from
782 developmental stages 28-to-60 hpf and larvae used for imaging were of 3-5 dpf, precluding
783 sex determination of the animals. The fish maintenance at the Pasteur Institute follows the
784 regulations of the 2010/63 UE European directives and is supervised by the veterinarian office
785 of Myriam Mattei.

786 **mRNA extraction and cDNA synthesis**

787 Total RNA was extracted from whole 48 hpf embryos for cDNA cloning or from pooled trunks
788 at the desired developmental stages (30-32 hpf, 48-50 hpf time windows for qRT-PCR
789 experiments) (~30 individuals per tube). Briefly, embryos were anesthetized using balneation
790 in embryo medium supplemented with tricaine methanesulfonate (MS-222, Sigma-Aldrich Cat#
791 A5040), at a final concentration of 160 μg/ml. RNA was extracted via organic extraction using
792 TRIzol reagent (Invitrogen Cat# 15596026) according to the manufacturer's guideline. gDNA
793 contaminant was removed using TURBO™ DNase (Invitrogen Cat# AM2238) treatment
794 according to the manufacturer's guideline. Total RNA was stored at -80°C. Reverse
795 transcription of mRNA was performed using SuperScriptIV (Invitrogen Cat# 18090010) with
796 OligodT primer. cDNA samples were stored at -20°C until further processing (for quantitative
797 real-time PCR, PCR, cloning and sequencing).

798 **Transient and stable transgenesis**

799 The *kdrl* promoter (*flk*) (Jin et al. 2005) was used to drive endothelial expression of mKate2-
800 Podxl2, eGFP-Jam2a and eGFP-Jam3b, with eGFP (Clontech) and mKate2 (Evrogen) cDNAs
801 amplified using overlapping primers for Gibson cloning. eGFP-Podxl2, ArhGEF11(PDZ-PRD-
802 RGS-eGFP) and dt-runx1-eGFP were amplified for cloning into a pG1-4XNR vector (built from
803 the 4XNR (non-repetitive) 4X UAS sequence less susceptible to methylation than the 14X UAS
804 described in (Akitake et al. 2011)). For the sequence of all the designed cloning primers, see
805 the Key Resources Table.

806 Podocalyxin-like 2 (Podxl2), ArhGEF11/PDZ-RhoGEF, JAM2a and JAM3b full length
807 sequences were amplified from pools of 48 hpf whole embryo cDNA (see before for mRNA
808 extraction and cDNA synthesis methodologies). All constructs generated in this study were
809 obtained using the Gibson assembly assay (NEB, Cat # E2611S).

810 For eGFP-Jam2a and eGFP-Jam3b cloning, we used the JAM2a signaling peptide sequence
811 (included in the 5-prime amplification primers and encoding for the signal peptide:
812 mlvcvsllilihsvpvspvtvssr) and, for both constructs, the eGFP sequence was inserted in frame

813 upstream of the sequence encoding for the transmembrane domain; for the eGFP-Jam2a
814 construct, the eGFP was inserted upstream of amino-acid D221 (DLNVAA) of the NCBI
815 Reference Sequence: NP_001091734.1; for the eGFP-Jam3b construct, the eGFP was
816 inserted upstream of amino-acid D243 (DINIAG) of the NCBI Reference Sequence:
817 NP_001076332.2. For transient ubiquitous and inducible expression, the eGFP-Jam2a and
818 eGFP-Jam3b fusion constructs were inserted into a KpnI pre-digested pG1 plasmid containing
819 tol2 sites and the HSP70-4 promoter. For stable transgenesis using the *kdrl* (*flk1*) promoter,
820 constructs cloned into the pG1-HSP70 plasmids were extracted using XhoI/NotI restriction
821 enzymes and inserted into the XhoI/NotI pre-digested pG1-flk1 vector using DNA T4 ligation
822 (NEB, Cat # M0202S).
823 For the Podxl2 N-ter deletion mutant that has been used for establishing stable *Tg* fish lines,
824 the cDNA encoding for the peptide sequence starting with amino-acid G341 (GGTEYL;
825 fragment 341-587) of the NCBI Reference Sequence: XP_692207.6 was fused with either
826 eGFP or mKate2 cDNAs. The sequence encoding for the signal peptide of the human CD8
827 (malpvtalllplalllhaarpsqfrvs) was introduced upstream (5-prime) of the eGFP or mKate2
828 sequences (included in the 5-prime primers designed for the Gibson cloning strategy). For the
829 construct designed to obtain the *Tg(kdrl:Gal4;UAS:RFP;4xNR:eGFP-Podxl2)* fish line, 2
830 overlapping fragments were amplified for cloning into a pG1-tol2_4xNR vector after digestion
831 with NcoI, with the following couples of primers: 4XNR_CD8-eGFP_fw and
832 delPodxl2_eGFP_rev; delPodxl2_fw and Podxl2_pG1-4XNR_rev. For the construct designed
833 to obtain the *Tg(kdrl:mKate2-Podxl2)* fish line 2 overlapping fragments were amplified for
834 cloning into a pG1-flk1 vector after digestion with EcoR1, with the following couples of primers:
835 pG1-flk1_CD8_mKate2_fw and delPodxL2-mKate2_rev; mKate2-delPodxL2_fw and
836 Podxl2_PG1-flk1_rev.
837 For the ArhGEF11(PDZ-PRD-RGS-eGFP) construct, the cDNA encoding for the peptide
838 ending upstream of the DH domain at Valine 709 of the amino-acid sequence (GenBank:
839 AY295347.1; PALDEDV; fragment 1-709) was fused upstream of the sequence encoding for

840 eGFP, for expression using the pG1-4xNR vector. The cDNA was amplified using the
841 GB_4xUAS-gef11_fw; GB_eGFP-RGS_rev couple of primers.
842 For the construct designed to obtain the *Tg(kdrl:Gal4;UAS:RFP;4xNR:dt-runx1-eGFP)* fish
843 line, the Runx1 sequence amplified omits the ATG (replaced by an nls) and ends downstream
844 of the Runt domain (ending at amino-acid sequence PAHSQIP). The construct allows for the
845 expression of the dt-runx1 protein under the control of the 4xNR driver using the same strategy
846 as for the above PodxL2 constructs. The dt-runx1 cDNA construct was amplified from the
847 zebrafish Runx1 cDNA sequence (Kalev-Zylinska et al. 2002) using the couple of primers GB-
848 4xnr-nlsRunx1_fw; GB-eGFP-T2A-2xHA-delRunx1_rev. The sequence of these primers each
849 allowed for the introduction, in the protein sequence, of a nls (encoded by the fw primer) and
850 of a 2xHA-T2A peptide (encoded by the rev primer that overlaps with the 5-prime sequence of
851 eGFP).
852 For all constructs, cloning reactions were used to transform NEB 5-alpha Competent E. coli
853 (NEB, Cat # C2987) and resistant clones then used for miniprep plasmid preparations
854 (Nucleospin plasmid, Macherey-Nagel, Cat # 740588.50), followed by sequencing. Plasmid
855 DNA from clones containing correct insertions where then used to transform E. coli TOP10
856 competent cells (Invitrogen, Cat # C404010) and purified using the endotoxin free NucleoBond
857 Xtra Midi kit (Macherey Nagel, Cat# 740420.10). Transgenesis was then performed by co-
858 injecting 1 nl of plasmid (at 25 ng/*µ*l) mixed with tol2 transposase mRNA (at 25 ng/*µ*l)
859 transcribed from linearized pCS-zT2TP plasmid using the mMESSAGE mMACHINE SP6 kit
860 (Ambion, Cat# AM1340). For stable transgenesis, embryos were screened for fluorescence
861 between 24 hpf and 48 hpf and raised to adulthood. Founders with germline integration were
862 then isolated by screening for fluorescence after outcrossing with AB adults and for
863 establishment of the F1 generation.
864
865 **CRISPR methodology and GEF11 mutant transgenic line screening**
866 *CRISPR/Cas9 mutagenesis and isolation of founders*

867 A sgRNA was designed against the splice donor site at the end of exon 38 with the aim to
868 interfere with the production of the splicing variant including its encoding sequence, using the
869 CRISPRscan web tool (Moreno-Mateos et al. 2015). The sgRNA was obtained by annealing
870 for 5 min at 95°C equal volumes of 100μM specific Alt-R® crRNAs (IDT, Cat# sequence:
871 AGCCAATCGTCTGAGGACGG) with 100μM Alt-R® generic tracrRNA (IDT, Cat# 1072532).
872 Cas9 Nuclease Reaction Buffer (NEB Cat# B0386A) was added to obtain a final 45μM sgRNA
873 stock solution. For the generation of the sgRNAs–Cas9 complex, a mix containing 18μM
874 sgRNA and 12μM Cas9 protein (EnGen™ Spy Cas9-NLS S. pyogenes, NEB Cat# M0646T)
875 was incubated for 10 min at room temperature. For mutagenesis, 1 nl of the sgRNA-Cas9
876 complex was injected into one-cell stage embryos, that were subsequently raised until 48 hpf.
877 Bulk genomic DNA (gDNA) was extracted from 60 injected and 60 non-injected control
878 embryos. gDNA extraction proceeded as follows: pooled samples were incubated for 3 hrs at
879 55°C in lysis buffer (100mM NaCl, 20mM Tris-HCl pH 8, 25mM EDTA, 0.5% SDS and 2 µg/µl
880 proteinase K), purified using phenol:chloroform. Precipitation was done in 0.1 volume of 3M
881 NaAc and 2.5 volume of 100% ethanol for 20 min at -20°C. Samples were centrifuged for 30
882 min at 4°C before washing with 70% ethanol and resuspension in water. gDNA was used for
883 PCR, using DNA polymerase Platinum™ SuperFi™ (Invitrogen Cat# 12351010) and the
884 SM31-SM32bis couple of primers (TTTCACTTTCTCTCTGCCTCTTACA;
885 AACTCTGTCCAGATGATTGAGGAGC) flanking the targeted region. PCR products were run
886 on gel electrophoresis before gel extraction of bands of interest (with sizes corresponding to
887 either a wild-type allele or a deleted allele) (Nucleospin gel and PCR clean-up, Macherey-
888 Nagel Cat# 740609.50). Fragments were cloned into blunt-end TOPO vector (Invitrogen Cat#
889 45024), transformed into E. coli TOP10 competent cells and grown on selective medium. 12
890 colonies for each PCR product were sent for sequencing. Mutant sequences contained either
891 a 7 nucleotides deletion, or a mix of 1,4 or 7 nucleotides deletions located at the same site (at
892 the end of exon 38, see ***Figure 7 - figure supplement 4A*** for the 7 nucleotides deletion),
893 attesting of the proper functioning of our guide.

894 A stable homogeneous mutant line was generated by injecting the sgRNA:Cas9 complex into
895 one-cell stage *Tg(kdrl:Gal4;UAS:RFP)* embryos similarly to what was described above. 100
896 embryos were raised until adulthood. Adult founders were identified by crossing adult F0 with
897 AB fishes, and single embryo genotyping was performed on their progeny (10 embryos per
898 adult fish). Briefly, single embryos were incubated in 40*µ*l 25mM NaOH 0.2mM EDTA and
899 heated for 10 min at 95°C, before cooling for 10 min at 4°C and addition of 40*µ*l 40mM Tris-
900 HCl pH5 to stop the reaction. PCR was performed using 5*µ*l of template and specific primers
901 (couple SM31-SM34 –TTTCACTTTCTCTCTGCCTCTTACA;
902 ATAAATGAAGCCCCACCTCCGTCC – for wild-type (WT) allele and couple SM31-SM40 –
903 TTTCACTTTCTCTCTGCCTCTTACA; ATGAAGCCCCACCTCAGACGATTGGC– for mutant
904 allele). Presence of WT or mutant allele for each single embryo was assessed by the
905 presence/absence of amplification band on gel electrophoresis. Four F0 founders were
906 isolated, that had a transmission rate in the germline ranging from 20% to 80%. Progeny of the
907 F0 founders and subsequent generations were raised separately until adulthood, and
908 genotyped. After complete anesthesia (in fish water supplemented with 160*µ*g/ml tricaine
909 methanesulfonate), a small tissue sample was collected from the caudal fin, placed into DNA
910 extraction buffer (10mM Tris pH8.2, 10mM EDTA, 200mMNaCl, 0.5% SDS, 200*µ*g/ml
911 proteinase K) and incubated 3 hrs at 50°C. DNA precipitation and resuspension was performed
912 as described above. 7*µ*L gDNA was used as template for PCR amplification using the primer
913 couple SM31-SM32bis. Sequenced PCR products showed that all founders harbored the same
914 7 nucleotides deletion (see ***Figure 7 - figure supplement 4A***). All experiments relative to
915 ***Figure 7*** *and* ***Figure 8*** were performed using the progenies of one heterozygous mutant F3
916 couple. For these experiments, genotyping on single embryos was performed on gDNA as
917 mentioned above. Only WT homozygous and mutant homozygous embryos were kept for
918 analysis.

919 *Alternative Cpf1 approach*

920 As an alternative approach to the CRISPR/Cas9 deletion, we attempted to generate a second
921 mutant line, using to CRISPR/Cpf1(Cas12a) system to delete a 315 nucleotides region
922 encompassing exon 38 (with specific guides located in the introns before and after exon 38).
923 The sequence of guides that have been tested are: TATCACACACACATCACCTTCTA and
924 TTTCTCAGCGCTCCTGACAGATG. However, due to the structure of the intronic regions
925 (repeat rich) and the necessary presence of specific PAM sequence, we only generated off-
926 target deletions of intronic regions, without deletions of exon 38, leading us to focus on the
927 CRISPR/Cas9 approach.
928
929 **Morpholinos and injections**
930 Morpholinos were obtained from GeneTools (see Key Resources Table for sequences). The
931 *sih* Tnnt2 translation start codon and flanking 5-prime sequence MO (Sehnert et al. 2002) as
932 well as the ArhGEF11 exon 38 splice blocking MO (overlapping the exon 38/intron 38-39
933 boundary) were resuspended in ddH2O to obtain stock solutions at 2mM and 1mM,
934 respectively. The *sih* MO (1.5ng) and ArhGEF11 exon 38 MO (3ng) were injected into 1-cell
935 stage zebrafish embryos, after dilution in ddH2O. For *sih* morphants, embryos that were used
936 in the experiments were checked for absence of heart beating 24 hrs after injection as well as
937 before being used for dissection and RNA extractions at the 30-32 and 48-50 hpf time-
938 windows. For measuring the efficiency of the ArhGEF11 exon 38 MO, total RNA was extracted
939 from pools of injected and control embryos followed by mRNA reverse transcription. PCR on
940 cDNA flanking the exon 38 was performed using DNA polymerase Platinum™ SuperFi™
941 (Invitrogen Cat# 12351010) and analyzed on gel electrophoresis before extraction, cloning and
942 sequencing to verify the absence of the DNA sequence encoded by exon 38 (see ***Figure 7 -***
943 ***figure supplement 4A***).
944
945 **Whole mount in situ hybridization**

946 For the sequence of all the primers used to amplify probes, see the Key Resources Table. The
947 probes for WISH concern Pard3ab, Pard3bb (***Figure 3***) and PDZ-RhoGEFs (***Figure 7 – figure***
948 ***supplement 2***).
949 Whole-mount chromogenic in situ hybridization was performed as described in Lancino et al
950 2018. Probes were synthetized using the manufacturer recommendation (T7 RNA polymerase,
951 Promega, Cat# P2075, DIG-nucleotides, Jena Bioscence, Cat# NU-803-DIGX).
952 For Pard3ab (GenBank: AY524776.2), a probe of 717bp (nucleotides 1258-1974)
953 encompassing the nucleotide sequence starting in the 3-prime of the sequence encoding for
954 PDZ1 and ending between PDZ2 and PDZ3 was amplified with the couple of primers
955 pard3ab_WISH_Nter_fw and pard3ab_WISH_Nter_T7_rev. For Pard3bb (NCBI Reference
956 sequence: XM_021478865.1), a probe of 747bp (nucleotides 468-1214) encompassing the
957 nucleotide sequence starting in the 5-prime of the sequence encoding for the N-ter of the
958 protein and ending at the 3-prime of PDZ1 was amplified with the couple of primers
959 pard3bb_WISH_Nter_fw and pard3bb_WISH_Nter_T7_rev (for the position of the primers
960 respectively to the 2 pard3 proteins sequences and domains, see Figure 3B).
961 Images were captured with the Zeiss Axio ZOOM V16 microscope with the Zen Pro2 software,
962 with a brightfield transmitted light optics. Post-processing steps were performed using the
963 Extended-Depth Focus method to combine in focus regions from multiple z-planes and convert
964 into in a transmitted light z-stack to generate a unique in-focus image.
965
966 **Immunofluorescence detection of the HA-tagged dt-runx1 deletion mutant**
967 Whole mount immunostaining was performed on hand-dechorionated 48 hpf *Tg(dt-runx1)*
968 embryos to assess the localization of the 2XHA-tagged dt-runx1 protein in aortic cells. Briefly,
969 embryos were fixed in 4% methanol free PFA (Polysciences Cat# 040181) for 3 hrs at room
970 temperature (RT) and washed in PBS/0.1% tween20 (PBT). Embryos were treated in
971 successive baths of milliQ water supplemented with 0.1% tween20, then in cold acetone for
972 10 min at -20°C and again in milliQ water plus 0.1% tween20. They were then washed in 1X

973 HBSS (Invitrogen Cat# 14025), and permeabilized for 45 min at RT in 1X HBSS, 0.1%
974 tween20, 5mM CaCl2 and 0.1mg/ml collagenase (Sigma-Aldrich Cat# C9891). Embryos were
975 then rinsed in PBSDT and incubated in blocking solution 1× sheep serum (SS, Sigma Cat#
976 S2263) for at least 4 hrs at RT. They were then incubated overnight at 4°C with primary
977 antibodies in blocking solution: rabbit anti-GFP (MBL Cat# 598; 1/300) and mouse anti-HA
978 (Sigma, Cat# 12ca5; 1/50). On the next day, embryos were washed several times in PBSDT
979 and endogenous peroxidase activity was inactivated by treatment with 6%H2O2 (Sigma-
980 Aldrich, Cat# H1009) for 1 hr at 4°C. Embryos were then incubated in the NGS for at least 4
981 hrs and incubated overnight at 4°C with secondary antibodies: goat anti-rabbit Alexa Fluor 488
982 (Invitrogen Cat# A11070; 1/400) and goat anti-mouse HRP-conjugated (Thermo Fisher
983 Scientific Cat# G-21040; 1/300). Finally, embryos were rinsed several times first in PBSDT and
984 after in PBT before HRP fluorescent revelation. Embryos were incubated for 45 min at RT in
985 the dark in imidazole buffer (0.1 M imidazole (Sigma-Aldrich, Cat# I5513) in PBT supplemented
986 with 1% H2O2) with Cy3 Tyramide Reagent (Cy3 NHS sigma Cat# PA13101, tyramide sigma
987 Cat# T-2879, dimethyl formamide sigma Cat# T-8654 and triethylamine sigma Cat# T-0886).
988 Final washes in PBT and in 6% H2O2 for POD inactivation were performed before embryos
989 were mounted in low-melting agarose in 1X PBT for fluorescence confocal imaging.
990
991 **Quantitative real-time PCR**
992 *Preparation of samples*
993 To determine the impact of runx1 interference and blood flow on pard3 family genes and splice
994 variants expression, total RNA from dissected trunk regions was extracted (as described
995 previously) from 30-32 hpf and 48-50 hpf embryos from either incross of the Tg(kdrl:dt-
996 runx1(eGFP)) fish line, outcross of the Tg(kdrl:dt-runx1(eGFP)) and Tg(kdrl:gal4;UAS:RFP)
997 fish lines - with eGFP positive embryos as the interfering condition and eGFP negative
998 embryos as sibling controls -, or Tg(kdrl:gal4;UAS:RFP) embryos injected at the single cell
999 stage with sih morpholino. Analysis was carried on 3 biological replicates.

1000 *Technical procedure*

1001 For the sequence of all the designed qRT-PCR primers, see the Key Resources Table.

1002 qRT-PCR was performed using Takyon Rox SYBR 2x Master mix blue dTTP kit (Eurogentec

1003 Cat# UF-RSMT-B0701), with starting concentrations of template of around 10ng/*µ*l and primer

1004 concentrations of 0.5*µ*M, on a QuantStudio3 system (Applied Biosystems). Each reaction was

1005 performed in technical triplicates and in at least 3 biological replicates. Ct was determined

1006 automatically by the QUANTSTUDIO™ DESIGN & ANALYSIS 2 software on the Thermofisher

1007 cloud and exported to be analyzed manually. Standard deviation was calculated within the

1008 technical triplicates, and when superior to 0.3, obvious outliers were removed (Dixon's Q test).

1009 The delta-delta-Ct method (double normalization to endogenous control — zebrafish

1010 elongation factor ef1α — and to control sample) was used to compare gene expression in

1011 control and altered conditions.

1012

1013 **In vivo confocal imaging**

1014 Embryos, dechorionated manually, were anesthetized using tricaine (Sigma Aldrich, Cat#

1015 A5040). They were then embedded on the side position in 1% low melting agarose (Promega,

1016 Cat# V2111) in a glass bottom 60µ-Dish (35mm high; Ibidi, Cat# 81156). To avoid movements

1017 and pigmentation during image acquisitions, 1x tricaine /1x PTU Volvic water was incorporated

1018 to the low melting agarose and, after solidification, 1ml of 1x tricaine /1x PTU Volvic water was

1019 added before sealing the dish.

1020 Embryos were imaged with 2 confocal microscope systems. For the results presented Figure

1021 1, z-stacks and time-lapse sequences were obtained using a Leica TCS SP8 inverted confocal

1022 microscope as described in Lancino et al 2018.

1023 For all the other confocal microscopy results, embryos were imaged using an Andor (Oxford

1024 Instruments) spinning disk confocal system (CSU-W1 Dual camera with 50µm Disk pattern

1025 and single laser input (445/488/561/642nm), LD Quad 405/488/561/640 and Tripl 445/561/640

1026 dichroic mirrors), equipped with a Leica DMi8 fluorescence inverted microscope and CMOS

1027 cameras (Orca Flash 4.0 V2+ (Hamamatsu)). Imaging was performed using a 40x water
1028 immersion objective (HC PL APO 40x/1.10 Water CORR CS2), a LEDs light source (CoolLED
1029 pE-4000 16 wavelength LED fluorescence system), and the acquisitions were piloted with the
1030 support of the MetaMorph software.
1031
1032 **Morphological and morphometric analysis of aortic and hemogenic cells**
1033 For the morphometric analysis of the aorta and aortic cells, large z-stack of 48-55 hpf
1034 Tg(kdrl:eGFP-JAM3b; kdrl:nls-mKate2) or Tg(kdrl:eGFP-JAM2a; kdrl:nls-mKate2)
1035 encompassing the whole aortic depth were acquired with optimal z-resolution (0.3μm z-step).
1036 For each embryo, 3 contiguous z-stacks of 330μm width were acquired, allowing us to image
1037 the entirety of the AGM region, from the anterior to the posterior end of the elongated yolk.
1038 *Samples*
1039 For ArhGEF11 splicing morpholino experiment, 3 splicing morpholino injected embryos and 2
1040 control non injected siblings were kept for the analysis.
1041 For ArhGEF11 CRISPR Cter deletion and when performing the experiments, imaging was
1042 done, for putative mutants, on embryos that had shown a delay in initiation of circulation at 24
1043 hpf, regained circulation at 48 hpf albeit with a clearly visible oedema in the cardiac region
1044 (non-altered embryos were kept as sibling controls). All imaged embryos whose signal allowed
1045 us to generate segmentable 2D-cartography from the whole length of the aorta were kept and
1046 processed further for genotyping. Genotyping confirmed that the circulation problems at 24 hpf
1047 and the remaining oedema at 48 hpf corresponded to embryos bearing the mutation.
1048 For CRISPR mutant phenotype analyses, 2 mutant embryos and 2 wild type siblings were kept,
1049 after genotyping.
1050 *Image analysis*
1051 The following image analysis was performed on Icy software.
1052 For each segment, we generated a 2D-cartography of the eGFP-Jam signals at intercellular
1053 contacts of aortic cells, using the Tubeskinner plugin, according to the protocol described in

1054 Lancino et al 2018. Briefly, the aorta was rotated to face the lumen, a circular ROI fitting the
1055 interior of the aorta was initialized by the experimenter on the first plane, and for each plane
1056 sequentially, the algorithm will more accurately fit the ROI to the aortic perimeter and collect
1057 the fluorescence intensity all along its longitudinal axis. The collected intensity was then
1058 projected on a 2D-plane, where the Y-axis of the 2D-cartography corresponds to the perimeter
1059 of the aorta, and the X-axis corresponds to the X-axis of the original z-stack.
1060 Before further processing, a metadata table recapitulating the dates and conditions of
1061 experiments for each embryo was generated, and a random label was assigned to rename
1062 each acquisition. This allowed for the later part of the analysis, that involves semi-automated
1063 segmentation and classification by the user, to be blind and avoid potential bias.
1064 Each 2D-cartography was then manually pre-segmented using the ROI Polygon tool to draw
1065 the contour of each aortic cell, using the original 3D z-stack as reference. Due to technical
1066 limitation (decreased fluorescence signal collection on the farthest lateral side of the aorta),
1067 only about 2/3 of the 2D-cartographies could be segmented (comprising the floor, the right
1068 lateral side of the aorta and the roof). The manual segmentation was then improved using the
1069 "Active Contour" plugin, that improved the fit of the cellular contour to the fluorescence signal
1070 and slightly dilated the cell contours until the ROIs formed a joint paving. All morphometric
1071 descriptors were extracted for each cell. The number of neighbours was automatically
1072 generated for each cell by counting the number of touching adjacent ROIs.
1073 Additionally, cells were manually classified into cell types according to morphometric
1074 parameters using as reference the original 3D z-stack and in particular the nls-mKate2 nuclear
1075 signal. EHT-undergoing cells were positioned on the floor of the aorta, have reduce antero-
1076 posterior axis length, luminal membrane inward bending for EHT pol+ cells and luminal
1077 membrane outward bending for EHT pol- cells, and a thickened nucleus. Hemogenic cells
1078 whose criteria were established in Lancino et al 2018 (elongated in the antero-posterior axis,
1079 with lateral membranes not trespassing the equatorial plane of the aortic wall), are positioned
1080 on the floor of the aorta, systematically have a reduced width perpendicular to the blood flow

1081 and, importantly, a thickened nucleus that protrudes out of the aortic plane. Finally, endothelial
1082 cells have a flattened nucleus positioned high on the lateral side or on the roof of the aorta.
1083
1084 **Measurement of the aortic perimeter**
1085 An accurate measurement of the aortic perimeter was obtained using the z-stack generated
1086 for the aortic cells' morphometric analysis. Briefly, the z-stack was rotated to face the lumen of
1087 the aorta and a ROI fitting the aortic perimeter was drawn by the user and optimized by the
1088 "Cell Contour" plugin. The length of the perimeter was then extracted from the ROI statistics.
1089
1090 **Fluorescence Recovery After Photobleaching (FRAP) measurements and analysis**
1091 Measurement of junctional turn-over was performed on 48-55 hpf *Tg(kdrl:eGFP-JAM3b;*
1092 *kdrl:nls-mKate2)* embryos using a Nikon Ti2e spinning disk microscope equipped with a
1093 sCMOS camera (Photometrics, Prime 95B, pixel size 11μm, 1200×1200 pixels, QE 95%) and
1094 a 40x water objective (Numerical Aperture 1.15, Working Distance 0.6mm, xy pixel size of
1095 0.27μm). Embryos were mounted as previously described.
1096 *Samples*
1097 For ArhGEF11 splicing morpholino phenotypic analysis, 10 different embryos (injected with the
1098 splicing morpholino) obtained from 3 separate experiments and 30 control embryos (non-
1099 injected siblings or control morpholino injected siblings) obtained from 6 separate experiments
1100 were analyzed.
1101 For EHT analysis, 16 embryos over 4 separate experiments were analyzed.
1102 For ArhGEF11 CRISPR/Cas9 Cter deletion phenotypic analysis, 8 mutant embryos and 12
1103 wild type siblings over 3 separate experiments were analyzed.
1104 Overall, the exact number of interfaces analyzed is written on each figure panel.
1105 *Acquisitions*
1106 For each acquisition, a wide two channels z-stack of the aorta was generated to capture the
1107 whole aortic volume and generate a 2D-cartography of the aortic environment (Icy, plugin

1108 Tubeskinner). This 2D-cartography of the cellular contours and the z-stack with the cellular
1109 contours and nuclei were used jointly to identify un-ambiguously cellular and junctional types
1110 and define one or multiple single point regions of interest (ROIs) for subsequent bleaching and
1111 fluorescence recovery measurement.
1112 The sequence of acquisitions before/after bleach focused only on the eGFP-Jam3b signal to
1113 speed up the acquisition and improve the temporal resolution. The 5 steps of the acquisition
1114 can be recapitulated as follows and we obtained/performed: (1) a single z-stack of 20μm
1115 centered on the plane of focus, (2) a 30 sec time-lapse acquisition on the plane of focus to
1116 measure average pre-bleach intensity with an image every second, (3) a high intensity
1117 stimulation of the ROIs (25% 300ms 488 FRAP laser exposure, leading to the bleaching of the
1118 Jam3b-eGFP signal), (4) a 3 min time-lapse acquisition on the plane of focus to measure fast
1119 post-bleach recovery with an image every second, and (5) a 7 min time lapse acquisition of
1120 8μm z-stack centered around focus plane with a 20 sec time interval to measure slow post-
1121 bleach recovery. Each step was save separately as .nd2 files.
1122 *Signal quantification and recovery analysis*
1123 File were converted from .nd2 to .tiff using FIJI batch converter, scale factor 1.00, bilinear
1124 interpolation, no average when downsizing, images read using bioformat.
1125 To collect fluorescence intensity, ROIs for each stimulation point was manually drawn using
1126 Fiji and named with an individual label using Fiji ROI manager. A metadata table was manually
1127 curated with all information for each ROI (junction type, condition, date of experiment, embryo
1128 number). An additional ROI was created to collect background intensity for subsequent
1129 corrections. Acquisitions with clear embryo movement or drifting were either completely
1130 removed from the dataset (~5% of the acquisitions) or only kept for early recovery analysis
1131 (see below) if the drift only occurred in the last step (fifth) of the acquisition.
1132 Fluorescence intensity for each ROI was collected and saved automatically as a .csv file for
1133 each acquisition using a homemade Fiji macro.
1134 All further analysis were performed using R for automatization.

1135 Briefly, for each ROI: the fluorescent signal was normalized to the background signal ($I_{background}$
1136 $_{normalized} = I_{roi} - I_{background}$), then normalized to mean intensity pre-bleach
1137 ($I_{normalized} = I_{background\ normalized\ ROI\ post\text{-}bleach} / I_{background\ normalized\ ROI\ pre\text{-}bleach}$), and finally scaled
1138 ($I_{full\ scaled\ normalized} = (I_{normalized} - \min(I_{normalized}))/(1 - \min(I_{normalized}))$).
1139 A single exponential equation was used to fit the data using the nls:multistart package for
1140 parameter optimization:
1141 $F(t) = A*(1-e^{-t*\tau})$
1142 With A the maximum amplitude of the curve, t the time, and τ a constant defining the growth
1143 rate of the curve.
1144 The fitted curve allowed to extract quantitative information describing the recovery of each type
1145 of junction in different conditions: the mobile fraction of the bleached pool (corresponding to A,
1146 the amplitude of recovery) and the time of half recovery, related to the speed of recovery, that
1147 can be extracted from τ:
1148 $T_{half\text{-}recovery} = \ln(0.5)/(-\tau)$
1149 A more precise description of the recovery speed was extracted from the observation of the
1150 early time period (until 30s post bleach), were the fluorescence intensity increases uniformly.
1151 A first-degree polynomial equation was fitted to the data (using lm() function from the stats
1152 package), and the coefficient corresponding to the slope of the fitted curve was used as a
1153 metric for speed of fluorescence recovery.
1154
1155 **Statistical analysis**
1156 Statistical tests used are described for each figure panel in the legend. Since our samples are
1157 usually small, the test used is an unpaired two samples non-parametrical Wilcoxon mean
1158 comparison test, without a priori knowledge on sample normal distribution or homoscedasticity.
1159
1160 **Data and software availability**

All graphics and plots were generated using RStudio and packages including: ggplot2 (Wickham 2016), readr (Wickham, Hester, and Bryan 2022), dplyr (Wickham et al. 2023), stringr (Wickham 2022), ggstatsplot (Patil 2022), ggpubr (Kassambara 2020), wesanderson (Ram and Wickham 2018), cowplot(Wilke 2020), ggsci (Xiao 2018), ggbeeswarm (Clarke and Sherrill-Mix 2017), viridis (Garnier 2021), DT (Xie, Cheng, and Tan 2022), SciViews (Grosjean 2019), nls.multstart (Padfield and Matheson 2020), matrixStats (Bengtsson 2022).

Acknowledgments

We wish to warmly thank Philippe Herbomel for his encouragements and for ensuring the funding of this study.

We thank our fish facility members Y. Rolin and K. Sebastien for their daily help, R. Patient (University of Oxford) for the Hsp70 promoter. This work was supported by Institut Pasteur, CNRS, grants to P. Herbomel from the Fondation pour la Recherche Médicale (#DEQ20160334881), the Fondation ARC pour la Recherche sur le Cancer, and the Agence Nationale de la Recherche Laboratoire d'Excellence Revive (Investissement d'Avenir, ANR-10-LABX-73), and a grant to AS from the Institut Pasteur (PTR 439-2021). LT was recipient of a PhD fellowship from the Collège Doctoral, Sorbonne Université, and from the Labex Revive (ANR-10-LABX-73).

Authors contributions

LT designed, performed and analyzed experiments, and wrote the Method section and the Figure legends. SM designed and conducted experiments. CV conducted experiments. AS conceived the project, designed, performed and analyzed experiments, wrote the manuscript with input from LT, and obtained funding.

Declaration of interests

The authors declare no competing interests.

1188 ## Figure legends

1189

1190 **Figure 1: Tracing the evolution of the luminal membrane using the polarity marker**
1191 **Podocalyxin points at the biological significance of apicobasal polarity establishment**
1192 **in EHT cell emergence complexity. A**, cartoons depicting the early and late steps of EHT
1193 cells emerging from the aortic floor (steps 1 and 2, as previously described in the zebrafish
1194 embryo, see (Kissa and Herbomel 2010; Lancino et al. 2018)) and with hypothetical evolution
1195 of the luminal membrane (in green) before (3 and 4) and after the release (2', the cell detaches
1196 from the endothelial layer via junction downregulation leading to exposure of the luminal
1197 membrane with le extracellular milieu; 3', the luminal membrane is consumed via endocytic
1198 recycling (E) and/or lysosomal degradation (Lys) prior to detachment; 4', the luminal
1199 membrane in 4 is released inside the cell (twisted arrow) before detachment. Grey area=
1200 nucleus. **B**, PodocalyxinL2 (Podxl2) construct designed to establish transgenic fish lines.
1201 Cartoons representing full length (top drawing) and deleted Podxl2 (amino-acid sequence 341-
1202 587) in which the mucin domain (serine/threonine-rich O-glycosylation domain) is replaced by
1203 either eGFP or mKate2. The tetracystein-containing globular domain (subjected to N-
1204 glycosylation) was kept as favoring apical membrane retention. TMD, transmembrane domain;
1205 DTHL, C-terminal peptidic motif involved in partnership with PDZ domain containing proteins.
1206 **C-D**, EHT performing cells visualized using *Tg(Kdrl:Gal4;UAS:RFP;4xNR:eGFP-Podxl2)*
1207 embryos and time-lapse sequences initiated at 55 hpf obtained with spinning disk confocal
1208 microscopy (imaging was performed at the boundary between the most downstream region of
1209 the AGM and the beginning of the caudal hematopoietic tissue). Top grey panels show the
1210 green, eGFP channels for eGFP-Podxl2 only. Bottom panels show the merge between green
1211 and red (soluble RFP, in magenta) channels. Bars: 8μm. **C**, single plane images of 2 EHT pol+
1212 cells extracted from a time-lapse sequence at t = 0 and t = 45 min, with the right cell (eht cell
1213 2) more advanced in the emergence process than the left one (eht cell1). Note the enrichment

1214 of eGFP-Podxl2 at the luminal membrane (surrounding the cavity labelled with an asterisk) in
1215 comparison to the basal membrane (white arrow). Note also the evolution of the luminal
1216 membranes with time, with the aortic and eht cell 1 lumens still connecting at t = 0 (green
1217 arrow), the apparent fragmentation of the cytosolic vacuole (2 asterisks for eht cell 1 at t = 45
1218 min) and the compaction of Podxl2-containing membranes for eht cell 2 at t = 45 min. More
1219 details on the evolution of the connection between the aortic/eht cell lumens are shown in
1220 ***Figure 1 – figure supplement 1A***. **D**, single plane images of 2 EHT pol- cells extracted from
1221 a time-lapse sequence at t = 30 min and t = 210 min (see ***Figure 1 – video 3*** for the full-time
1222 lapse sequence), with the right cell (eht cell 2) slightly more advanced in the emergence than
1223 the left one (eht cell 1, with the latest attachment point between the emerging cell and the
1224 aortic floor (pink arrow)). Note, in comparison with the cells in panel C, the ovoid shapes of
1225 cells, the absence of enrichment of eGFP-Podxl2 at luminal membranes (green arrows) and
1226 the accumulation of eGFP-Podxl2 at basal membrane rounded protrusions (white arrows).
1227

1228 **Figure 2: Immature HE is not polarized and controls membrane delivery of intra-**
1229 **cytosolic vesicular pools**. **A**, *Tg(Kdrl:Gal4;UAS:RFP;4xNR:eGFP-Podxl2)* embryo imaged
1230 using spinning disk confocal microscopy. Black and white images show eGFP-Podxl2 only.
1231 Images were obtained from a time-lapse sequence (initiated at 35 hpf) lasting for 435 min (7.25
1232 hrs), with intervals of 15 min between each z-stack. Example of an HE cell with equal
1233 partitioning of eGFP-podxl2 between luminal and abluminal membranes (at t = 0 min), with
1234 eGFP-podxl2 containing intra-cytosolic vesicles (one labelled with a green asterisk) and
1235 undergoing mitosis at t = 30 min (HE cell 1' and HE cell 1'' are daughter cells). Note the
1236 inheritance of the largest micropinocytic-like vacuole by HE cell 1' and its maintenance through
1237 time until EHT emergence initiation at t = 180 min (green asterisk in 1.5x magnified areas at t
1238 = 60 and 90 min). At t = 360 min (green box) both fluorescence channels are shown; bottom
1239 panel: green (eGFP-Podxl2), magenta (soluble RFP). The magenta arrow points at the basal

1240 side of the EHT pol + cell that does not contain any detectable eGFP-Podxl2; on the contrary,
1241 eGFP-Podxl2 is enriched at the luminal/apical membrane (note that exocytosis of the large
1242 vacuolar structure may have contributed to increase the surface of the apical/luminal
1243 membrane (the green asterisk labels the lumen of the EHT pol + cell). The green arrow points
1244 at the abluminal membrane of the EHT cell derived from HE cell 1'' and that contains eGFP-
1245 Podxl2 (with no evidence of a significant expansion of a luminal/apical membrane); this
1246 indicates that this cell is more likely to be an EHT pol- cell that does not sort the vesicular cargo
1247 to the luminal/apical membrane. Bar = 10μm. **B**, model summarizing the evolution of HE cells
1248 that involves the tuning of apicobasal polarity thus leading to cells competent for giving birth to
1249 either EHT pol+ or EHT pol- cells (including the oriented release of large vesicular
1250 macropinocytic-like vacuoles preferentially toward the luminal membrane of future EHT pol +
1251 cells). The polarity status of the HE is proposed to evolve throughout the entire time window
1252 of the EHT, leading to asynchrony in its ability to give birth to EHT cells (emergence of EHT
1253 pol+ and EHT pol- cells are both observed until 72 hpf, see main text).
1254
1255 **Figure 3: Molecular variants and deletion mutants to investigate the control of**
1256 **apicobasal polarity during the 30-32 and 48-50 hpf time-windows. A,** Expression of
1257 Pard3ab and bb isoforms in the zebrafish embryo at 35 hpf using whole mount in situ
1258 hybridization (WISH). Expression in the dorsal aorta, in the trunk region (delimited areas), is
1259 marked by arrowheads as well as in the veinous plexus of the caudal hematopoietic tissue, in
1260 the tail. ey = elongated yolk. **B,** Pard3ab and bb zebrafish isoforms and natural variants to
1261 investigate the regulation of apicobasal polarity during the 30-32 hpf and 48-50 hpf time
1262 windows. The cartoons show the 3 sequential PDZ domains (PDZ1-3), the CR1 and CR3
1263 conserved regions involved in oligomerization and atypical protein kinase C (aPKC) binding,
1264 respectively. For each isoform, the variants that we have cloned either contain or exclude (+/-
1265 exon) the peptides encoded by specific exons (see ***Materials and Methods***); of relevance for
1266 our purpose (investigating the expression of potential interfering isoforms), we focused on

1267 isoforms deleted from exons encoding for part of the PDZ domains (covering the amino-
1268 terminus of Pard3ab PDZ2 and the carboxy-terminus of Pard3bb PDZ3). Note that deletion of
1269 exon 10 of Pard3ab triggers a frame shift in the ORF leading to a complete deletion of PDZ2
1270 and to a premature stop codon upstream of PDZ3. In this case, this should lead to the synthesis
1271 of a deleted proteins with major loss of function or, alternatively, the degradation of the mRNA
1272 via alternative splicing activated non-sense mediated decay (NMD, as exemplified in the EMT
1273 process, see (Pradella et al. 2017)). The position of the primers used to amplify cDNA
1274 fragments is depicted (fw (forward), rev (reverse), magenta: primers for WISH probes; see
1275 ***Materials and Methods***). Note that, in this study and for the PDZ1 domain of Pard3ab, we did
1276 not address the expression levels of the isoforms containing or not the insert encoding for the
1277 YVFR peptide. **C**, **left:** cartoons representing the zebrafish full-length runx1a amino-acid
1278 sequence and the dt-runx1 mutant deleted from the trans-activation domain and of the C-
1279 terminus (note that the construct encodes for a C-terminal fusion with eGFP that is released
1280 upon expression via a cleavable T2A peptide (introduced between the 2xHA tag and the N-
1281 terminus of eGFP, to prevent from potential steric hindrance). nls, nuclear localization signal.
1282 **Right:** anti-HA tag immunofluorescence obtained after z-projection of the dorsal aorta of a 50
1283 hpf *Tg(dt-runx1)* embryo. Note the localization of the 2xHA-tagged dt-runx1 protein in nuclei
1284 (some of them are pointed by red arrowheads) and of eGFP in nuclei and the cytosol of aortic
1285 cells. Bar: 25μm.
1286
1287 **Figure 4: Pard3 isoforms and variants are differentially regulated during the 30-32 and**
1288 **48-50 hpf time-windows.** qRT-PCR analysis of gene products of interest in trunks isolated
1289 from 30-32 hpf and 48-50 hpf embryos. Trunks were collected from eGFP positive or eGFP
1290 negative incrosses of heterozygous *Tg(dt-runx1) fishes* (dt-runx1 incross and sibling controls,
1291 respectively) and from *Tg(kdrl:Gal4;UAS:RFP)* embryos injected or not at the single cell stage
1292 with the *sih* morpholino (morpholino sih). Graphs show the measured mean fold changes
1293 relative to the expression of ef1α and to the expression in control embryos. Statistical tests:

1294 two sided unpaired two samples Wilcoxon test, with p-values of significant differences. **A,** gene
1295 expression levels of (**left)** the 3 isoforms of Pard3 proteins (Pard3ab, bb, b and ba, see
1296 ***Materials and Methods*** for accession numbers and primers) and (**right**) the hematopoietic
1297 marker cmyb and the polarity protein Scrib (for the cellular basolateral domain
1298 establishment/maintenance). **B,** Pard3ab and Pard3bb gene expression levels for dt-runx1
1299 mutants (red boxes) and for the *sih* morpholino (yellow boxes), all relative to control conditions.
1300 **C,** Pard3ab +/- PDZ2 (top 2 panels) and Pard3bb +/- PDZ3 (bottom 2 panels) gene splicing
1301 variants expression levels for dt-runx1 mutants (left panels, red boxes) or the *sih* morpholino
1302 (right panels, yellow boxes), all relative to control conditions.
1303
1304 **Figure 5: eGFP-Jam3b localization is reinforced at antero-posterior sites of the**
1305 **endothelial/EHT interface and at tri-cellular junctions. A**, cartoons representing
1306 homodimers of full-length JAMs with the C-terminal cytosolic part interacting with Pard3 (JAMs
1307 interact with the first PDZ domain of Pard3) as well as the constructs generated in this study
1308 and containing eGFP inserted between the Immunoglobulin-like (Ig) domains and the trans-
1309 membrane region (TMD). The constructs were obtained for zebrafish JAM2a and JAM3b. **B,**
1310 **C**, 52 hpf *Tg(kdrl:eGFP-Jam3b; kdrl:nls-mKate2)* embryos were imaged in the trunk region
1311 (AGM) using spinning disc confocal microscopy. The panels are either maximum z-projections
1312 (top two) or single plane z-sections (bottom two, focusing on the aortic floor) of aortic
1313 segments, with either the merged nls-mkate2 and eGFP-Jam3b fluorescence signals
1314 (magenta and green) or the eGFP-Jam3b signal only (black and white images). Bottom of the
1315 Figure: 2D-cartographies obtained after deploying aortic cylinders and showing the eGFP-
1316 Jam3b signals only. **B**, example of an EHT pol+ cell (cell 1, white arrows point at reinforcement
1317 of signal at antero-posterior junctions). On the 2D cartography, cell 1 (red) is contacting
1318 endothelial cells 2 and 3; note the reinforcement of eGFP-Jam3b signals along antero-
1319 posterior membrane interfaces perpendicular to blood flow (red arrows) as well as at the two
1320 tri-cellular junctions visible between cells 1, 2 and 3 (black arrows). **C**, example of two EHT

1321 pol- cells (cells 1 and 2, white arrows point at reinforcement of signal at antero-posterior
1322 junctions). On the 2D cartography, cells 1 and 2 (red) are contacting endothelial cells 3, 4, 6
1323 and 3, 6 respectively; note the reinforcement of eGFP-Jam3b signals along antero-posterior
1324 membrane interfaces perpendicular to blood flow (red arrows) and endothelial cell 6 that has
1325 intercalated between endothelial cell 7 and EHT pol- cell 2 (blue arrow). In right margins,
1326 magenta and green arrowheads designate the aortic floor and roof, respectively. Bars = 10μm.
1327

1328 **Figure 6: Junctional recycling at tri-cellular contacts is differentially controlled between**
1329 **the two EHT types.** 48-55 hpf *Tg(kdrl:eGFP-Jam3b; kdrl:nls-mKate2)* embryos were imaged
1330 using spinning disc confocal microscopy and illuminated for Fluorescence Recovery After
1331 Photobleaching (FRAP) in the trunk region (AGM, Aorta Gonad Mesonephros). **A, B**, panels
1332 are either maximum z-projections (top left) or single plane z-sections (bottom left and top right,
1333 focusing on the aortic floor) of aortic segments, with either the merged nls-mkate2 and eGFP-
1334 Jam3b fluorescence signals (magenta and green) or the eGFP-Jam3b signal only (black and
1335 white images). White arrows point at reinforcement of signal at antero-posterior junctional
1336 pools of an EHT pol+ cell (**A**) or of an EHT pol- cell (**B**), both marked by asterisks. Bottom right:
1337 2D-cartographies obtained after deploying aortic cylinders and showing the eGFP-Jam3b
1338 signals only. Black arrows point at antero-posterior junctional pools, in particular at tri-
1339 junctional regions that exhibit increase in signal density (well visible in **A,** black arrows). 2 and
1340 3 endothelial cells are contacting the EHT pol+ cell (**A**) and the EHT pol- cell (**B**), respectively.
1341 In right margins, magenta and green arrowheads designate the aortic floor and roof,
1342 respectively. Bars = 20μm. **C - G,** FRAP analyses. EGFP-Jam3b junctional pools
1343 corresponding to the brightest spots inside junctional regions of interest were bleached for
1344 FRAP measurements (these high intensity pools were localized at the level of bi- and tri-
1345 junctions for endothelial cells (EC) and in tri-junctional regions for EHT pol+ and EHT pol- cells;
1346 all these junctional pools were systematically visualized by deploying each aortic segment
1347 before bleaching as shown in the 2D-cartographies in A and B as well as in ***Figure 6 – figure***

1348 ***supplement 1***, see also ***Materials and Methods***). FRAP analysis concerned 3 types of
1349 junctional interfaces: between endothelial cells (EC – EC, black and grey), EHT pol- and
1350 endothelial cells (pol- – EC, brown), EHT pol+ and endothelial cells (pol+ – EC, blue). **C, D**,
1351 evolution of mean fluorescence intensity for each type of junctional interface over time (10
1352 min), after photobleaching (t = 0s). **E**, median maximum amplitude of recovery of all
1353 determinations and for each type of junctional interface (maximum of simple exponential fitted
1354 curves). **F, G**, early fluorescence recovery. Early evolution (over the first 30s) of the mean
1355 fluorescence intensity for each type of junctional interface over time after photobleaching (t =
1356 0s). **F**, the fitted lines correspond to linear regressions of mean fluorescence intensities. **G**,
1357 median values of fluorescence recovery slopes (linear regressions) of all determinations and
1358 for each type of junctional interface. Statistical tests: two sided unpaired two samples Wilcoxon
1359 test.
1360
1361 **Figure 7: Interfering with ArhGEF11/PDZ-RhoGEF function leads to the accumulation of**
1362 **hemogenic cells and impairs EHT progression. A-C,** numeration and morphometric
1363 analyses of aorta and cell types for *Tg(kdrl:eGFP-Jam3b; kdrl:nls-mKate2)* ArhGEF11 exon
1364 38 splicing morpholino-injected and control embryos (**A**), or for *(Kdrl:eGFP-Jam3b;*
1365 *kdrl:*ArhGEF11$^{\text{CRISPR-Cterdel+/+}}$) homozygous ArhGEF11 C-ter deletion mutants and control
1366 siblings (**B**). 48-55 hpf embryos were imaged using spinning disk confocal microscopy. **Aa,**
1367 **Bb**, 2D-cartographies obtained after deploying aortic cylinders and showing the eGFP-Jam3b
1368 signals only with cell contours delineated either in blue (endothelial cells), yellow (hemogenic
1369 cells, see ***Materials and Methods*** for their morphological definition), red (morphologically
1370 characterized EHT cells, for controls), and small cells delineated by cyan boxes
1371 (morphologically uncharacterized EHT cells and putative post-mitotic cells remaining as pairs,
1372 included in the numeration as hemogenic cells). Cellular contours have been semi-
1373 automatically segmented along the cellular interfaces labelled with eGFP-Jam3b (see

1374 ***Materials and Methods***). Scale bars: 10μm. **Aa', Bb'**, **left:** numeration of endothelial,
1375 hemogenic and EHT-undergoing cells according to the position of their geometrical center
1376 (either on the aortic floor, or on the roof, or on the lateral side), for each condition; **right**: number
1377 of endothelial, hemogenic and EHT-undergoing cells in each condition calculated from the
1378 segmentation of 3 x 2D-projections per embryo and covering the entire aortic regions in the
1379 trunk. **Aa'', Bb''**, **left**: length of hemogenic cells (in the longest axis) in function of their
1380 orientation (°) relative to the blood flow axis (0 – 180°); **right**: distribution of the orientation of
1381 hemogenic cells relative to the blood flow axis, displayed as a mean distribution of cells per
1382 embryo. **Aa''', Bb'''**, hemogenic cell elongation factors in arbitrary Units (scale factor given by
1383 the ratio between the first- and the second-best fitting ellipse diameters, the minimum value
1384 being 1 for a non-elongated object) represented as boxplot distribution of all segmented cells
1385 (**left**) or as the distribution of cell elongation factor per embryo (**right**), for controls and for
1386 interfering conditions as indicated. **Aa'''', Bb''''**, hemogenic cell area represented as boxplot
1387 distribution of all segmented cells (**left**) or as the distribution of cell area per embryo (**right**),
1388 for controls and for interfering conditions as indicated. **C**, aortic perimeter (in μm) for controls
1389 and mutant conditions as indicated. Statistical tests: two sided unpaired two samples Wilcoxon
1390 test. For the ArhGEF11 exon 38 splicing morpholino condition, analysis was performed on 2
1391 x control (non-injected embryos) and 3 x embryos injected at the one-cell stage; for the
1392 CRISPR mutant condition, analysis was performed on 2 x wild-type siblings for control and 2
1393 x homozygous mutant embryos whose DNA mutation was confirmed by sequencing. 3
1394 consecutive aortic segments per embryo were analyzed to cover the whole length of the dorsal
1395 aorta, in the trunk region (covering a distance of 990μm per embryo).
1396
1397 **Figure 8: Interfering with the function of ArhGEF11/PDZ-RhoGEF suggests an activity**
1398 **at the interface between endothelial and hemogenic cells that relies on restricting the**
1399 **mobility of junctional pools at tri-cellular junctions, with a prominent role of the +exon**

1400 **38 variant during endothelial cell intercalation. A**, 2D-cartography of an aortic segment of
1401 a *Tg(kdrl:eGFP-Jam3b; kdrl:nls-mkate2)* embryo injected at the one cell stage with the
1402 ArhGEF11 exon 38 splicing morpholino. All the arrows pointing at reinforced junctional
1403 contacts between cells were bleached and imaged for FRAP analysis (the bleached areas
1404 correspond to the spots of highest intensities in the regions of interest, as visualized at the
1405 fluorescent confocal microscope, see ***Materials and Methods***). Black and Magenta arrows
1406 point at he-he-ec and he-ec-ec tri-cellular junctions, respectively (he: hemogenic cell; ec:
1407 endothelial cell). Green arrows point at he-ec bi-cellular junctions. ec: endothelial cell, he:
1408 hemogenic cell. Bar = 20μm. **B, C**, FRAP analysis of bleached eGFP-Jam3b localized in
1409 regions of interest in controls (grey) and ArhGEF11 exon 38 splicing morpholino injected
1410 embryos (blue) or homozygous ArhGEF11$^{\text{CRISPR-Cterdel+/+}}$ mutants (green). Statistical tests: two
1411 sided unpaired two samples Wilcoxon test. Bb, Cc, evolution, after photobleaching (at t=0s),
1412 of the mean fluorescence intensity per condition at HE-EC, HE-EC-EC and HE-HE-EC bi- and
1413 tri-junctions over time (10 min). Bb', Cc', median values for maximum amplitude of recovery
1414 (maximum of simple exponential fitted curves, see ***Materials and Methods***). Bb'', Cc'', early
1415 evolution, after photobleaching (at t=0s), of the mean fluorescence intensity per condition over
1416 time (for the first 30 seconds). The fitted lines correspond to the linear regression of the mean
1417 fluorescence intensities. Bb''', Cc''', median fluorescence recovery slopes (linear regression).
1418 **D**, Model (2D deployment of the aortic wall) representing the endothelial/hemogenic dynamic
1419 interplay and the proposed function of ArhGEF11 and of its +exon 38 peptide encoding variant
1420 at junctional and membrane interfaces. This interplay involves 2 essential dynamic events
1421 requiring junctional remodeling: **1** (left cartoon, magenta arrows), the mobility of he-ec-ec tri-
1422 junctional contacts accompanying the movement of endothelial cells (ex: for ec1 and ec2)
1423 along lateral sides of hemogenic cells which is required to decrease the number of adjoining
1424 cells (see Lancino et al. 2018). This takes place contemporarily to - or in alternance with -, the
1425 contraction of HE and EHT cells as they are progressing throughout the emergence and
1426 reducing contacting membrane surfaces along the longitudinal axis (the reduction in contacting

1427 membrane surfaces also involves membrane retrieval, hypothetically via endocytosis). Our
1428 data obtained with the CRISPR deletion mutants (a slight tendency to increase, on average,
1429 the turnover and mobile pool of these he-ec-ec junctions) suggest that ArhGEF11, in the wild
1430 type condition, should be slowing down the recycling of junctional components at tri-junctions,
1431 which hypothetically should contribute to increase adhesion strength. This may be required
1432 also to stabilize the junction-cytoskeleton interface involved in controlling the
1433 contraction/shrinkage of HE cells along the longitudinal axis, a hypothesis that is compatible
1434 with the mutant phenotype observed in this study, i.e the increase in frequency of more
1435 elongated HE cells and the decrease in HE cell progression throughout EHT (see ***Figure 7***); **2**
1436 (right cartoon, cyan arrow and bottom cartoons a-c), the intercalation of an endothelial cell to
1437 isolate 2 adjacent hemogenic cells or 2 daughter cells after mitosis (not depicted). This is
1438 mandatory for EHT progression and completion which requires adjoining endothelial cells to
1439 protrude membrane extensions that will anastomose to seal the aortic floor (see Lancino et al.
1440 2018). The accumulation of adjoining cells of rather small length and apparently impaired in
1441 EHT progression that we describe in ***Figure*** 7 upon MO interference (that may also indicate
1442 impairment in abscission completion) suggests that the ArhGEF11 +exon 38 peptide encoding
1443 variant is more specifically involved in controlling the remodeling of the he/he interface that
1444 leads to endothelial cell intercalation (bottom cartoons, the remodeling of he-he-ec junctions is
1445 leading to he-ec-ec junctions and takes place between b and c). The increase in the recycling
1446 parameters that we measure in this interfering condition (mobile pool and early speed of
1447 recovery) indicates that the activity of ArhGEF11, and in particular of its +exon 38 peptide
1448 encoding variant, negatively controls junctional recycling. Hypothetically, the junctional
1449 adhesion strengthening triggered by reducing the recycling of junctional components at the
1450 he/he interface may be required during the early phase and progression of intercalation to
1451 support increase in membrane tension and environmental constraints (intercalation contributes
1452 to reducing the length/surface of the he/he membrane interface preceding junctional

remodeling (cartoons b and c); this reducing membrane interface is in addition submitted to the shear stress imposed by blood flow).

1456 **Legends to supplement figures**

1457

1458 **Figure 1 – figure supplement 1. A**, 2 EHT pol+ cells visualized using a
1459 *Tg(Kdrl:Gal4;UAS:RFP;4xNR:eGFP-Podxl2)* embryo and time-lapse sequence (initiated at 55
1460 hpf) obtained with spinning disk confocal microscopy. The images are extracted from the same
1461 time lapse sequence than the one used for ***Figure 1C***. Green channel (eGFP-Podxl2) only is
1462 shown. Green arrows point at the evolution of the connection between the aortic/eht cell
1463 lumens at t = 0, 10, 30 min. Asterisks label the lumen delimited by the luminal/apical
1464 membranes. Bar = 8μm. **B**, Model summarizing and interpreting the temporal evolution of the
1465 luminal/apical membrane (in green, the asterisks mark the lumen of the apparent vacuole-like
1466 intracellular membrane structures) after the release of an EHT pol+ cell from the aortic floor.
1467 **Step 1**, the pseudo-vacuole filled with fluid and delimited by eGFP-Podxl2 as visualized at t =
1468 65 min in **A** (and also at 45 min in ***Figure 1C***, 2 asterisks) is consumed partly via budding (after
1469 sorting of eGFP-Podxl2); these budding profiles can be seen on the left image (pink
1470 arrowheads) corresponding, for eht cell 1, to the plane 16 of the time point t = 80 min of the
1471 time lapse sequence (see the Z-stack in ***Figure 1 – video 2***). **Step 2**, after sorting and budding,
1472 the cell remains with pseudo-endocytic Podxl2 containing membranes and the remaining
1473 vacuolar structures filled up with fluid regress, putatively by chasing water as illustrated in **step**
1474 **3**. **Step 4**, the eht cell remains with pseudo-endocytic Podxl2 containing membranes that label
1475 newly born precursors of HSPCs. Note that since the cell remains in contact with the aortic
1476 floor while the pseudo-vacuole is regressing, the vacuole-like intracellular membrane proximal
1477 to aortic cells may never undergo fission (see ***Figure 1A***, steps 4-4') but gets consumed via
1478 budding and flattening upon water chase (steps 1-3 that are similar to ***Figure 1A***, steps 3-3').

1479

1480 **Figure 1 – video 1. EHT pol+ cells at early timing.** Z-stack (37 planes) corresponding to the
1481 time point t = 0 min whose plane 21 is shown ***Figure 1C***.

1482

1483 **Figure 1 – video 2. EHT pol+ cells at late timing.** Z-stack (37 planes) corresponding to the
1484 time point t = 80 min whose planes 16 (for eht cell 1) and 22 (for eht cell 2) are shown ***Figure***
1485 ***1 – figure supplement 1B.***

1486

1487 **Figure 1 – video 3. Emergence of EHT pol- cells.** Time-lapse sequence using a
1488 *Tg(Kdrl:Gal4;UAS:RFP;4xNR:eGFP-Podxl2)* embryo, obtained with spinning disk confocal
1489 microscopy (38 timing points, each acquired with 10 min intervals, starting at 55 hpf) and from
1490 which the images of the 2 emerging EHT pol- cells shown Figure 1D were extracted.

1491

1492 **Figure 2 – figure supplement 1. HE cells are not polarized at 30 hpf.**
1493 *Tg(Kdrl:Gal4;UAS:RFP;4xNR:eGFP-Podxl2)* 30 hpf embryo imaged using spinning disk
1494 confocal microscopy. **Top 2 panels**: green (eGFP-Podxl2) and red (soluble RFP, in magenta)
1495 channels. White arrows point at 2 individual EHT cells. Note that HE cell 1 protrudes long
1496 filopodia, some of which inside the aortic lumen (live imaging shows that they are moving along
1497 the blood flow, data not shown). **Bottom 2 panels**: 1.625X magnification of EHT cell 1 and 2
1498 in top panels. Green channel (eGFP-Podxl2) only. Green arrows point at very large intracellular
1499 vesicles, the largest reaching approximately 30μm. Asterisks mark the cytoplasm. Bar: 100μm.

1500

1501 **Figure 2 – figure supplement 2. Evolution of non-polarized HE cells throughout**
1502 **emergence**. *Tg(Kdrl:Gal4;UAS:RFP;4xNR:eGFP-Podxl2)* embryo imaged using spinning disk
1503 confocal microscopy. Images were obtained from discontinuous time-lapse sequences
1504 covering a period of 13 hours (from 35 – to – 48 hpf). Successive phases of the evolution of
1505 HE cells are visible, from a non-polarized status (with the accumulation of Podxl2-containing
1506 intra-cytosolic vesicles as well as cell division) to post-emergence EHT cells remaining
1507 beneath the aortic floor. The top panel is a z-projection of 69 consecutive z-sections
1508 interspaced by 0.3μm; green (eGFP-Podxl2) and red (soluble RFP, in magenta) channels are

1509 shown; 4 individual HE cells (1 – 4, green arrows)) are marked, with cells 1 and 4 more
1510 advanced in the process of emergence. All the other panels are z-sections focused on the
1511 aortic floor, allowing visualizing the progression of the EHT, in particular at 35 hpf (t = 0), a
1512 timing point at which the separation between the luminal and basal membranes are equally
1513 labelled with eGFP-Podxl2, attesting for the absence of apicobasal polarity (see cells 1 and 4,
1514 see also cell 1 at t = 2.5 hours (hrs) and cells 3' and 3'' at t = 5 hrs). Note, at t = 2.5 and 5.0
1515 hrs, the presence of intracytoplasmic eGFP-Podxl2 labelled vesicles inside HE cells,
1516 suggesting vesicular transport (white arrowheads, to be compared with images ***Figure 2 –***
1517 ***figure supplement 1***, at 30 hpf). At 48 hpf (bottom panel), HE cells have emerged and remain,
1518 for some of them, in close contact with the aortic floor (after having performed mitosis (notably
1519 for HE cell 2 (the division is visualized at 5hrs) and for HE cell 3, each one giving rise to cells
1520 2' - 2'' and 3' - 3'' respectively, all containing residual eGFP-Podxl2 containing membranes as
1521 EHT signature). Bar = 80*µ*m.
1522
1523 **Figure 3 – figure supplement 1. Phenotypic analysis of dt-runx1 expressing mutants:**
1524 **expansion of the thymus. A**, maximum z-projections of confocal spinning disk sections of the
1525 thymus region of 5 dpf *Tg(kdrl:gal4;UAS:RFP)* (left, control) and incrossed
1526 *Tg(kdrl:Gal4;UAS:RFP;4xNR:dt-runx1-eGFP)* (right, dt-runx1) larva. The area for each thymus
1527 is delimitated (white lines); note the systematic expansion of thymic cells on the right sides of
1528 each image for dt-runx1 mutants in comparison to controls. Bar: 20*µ*m. **B**, Area of projected
1529 thymus for the 2 conditions illustrated in A. Statistical tests: two sided unpaired two samples
1530 Wilcoxon test, with p-values of significant differences only.
1531
1532
1533 **Figure 3 – figure supplement 2. Phenotypic analysis of dt-runx1 expressing mutants:**
1534 **evidence for apicobasal polarity of hemogenic cells.** 30-32 hpf embryos obtained from

1535 *outcrossed Tg(Kdrl:Gal4;UAS:RFP;4xNR:mKate2-Podxl2) X Tg(kdrl:Gal4;UAS:RFP;4xNR:dt-*
1536 *runx1-eGFP)* fishes and imaged in the trunk (AGM) region using spinning disk confocal
1537 microscopy. Images are depicting typical HE cells (in boxes) from hemogenic regions, with
1538 apical and basal membranes clearly separated from each other owing to reduction of their
1539 surface area (in comparison to flat aortic cells) and elongation in the antero-posterior axis.
1540 Luminal membranes are enriched with (magenta arrows) or more or less devoid of (green
1541 arrows) mkate2-Podxl2. Green: cytosolic eGFP released from the cleavage of *dt-runx1-eGFP*.
1542 Note that because of mosaicism, he cell 2 does not express mkate2-Podxl2. Bars:100*μ*m.
1543
1544 **Figure 3 – figure supplement 3. Phenotypic analysis of dt-runx1 expressing mutants:**
1545 **slowing down of the emergence process and accumulation of EHT cells.**
1546 *Tg(kdrl:Gal4;UAS:RFP;4xNR:dt-runx1-eGFP)* embryos imaged using spinning disk confocal
1547 microscopy and analyzed in the AGM/trunk region. **A,** z-projections of the dorsal aorta obtained
1548 from 52-55 hpf embryos. Top panel: fluorescence from the red channel is shown for the
1549 *Tg(Kdrl:Gal4;UAS:RFP)* control. Bottom panels: fluorescence in the green channel only is
1550 shown for the mutants (eGFP, released form the dt-runx1-eGFP cleavage). The black asterisks
1551 point at emerged cells that are in close contact with the aortic floor. Green arrows: EHT pol+
1552 cells on aortic floor; magenta arrows: EHT pol+ cells in the lateral aortic wall; white arrows:
1553 uncharacterized emerging cells; he: hemogenic cells. **B,** evolution of an EHT cell extracted
1554 from a 7 hrs time-lapse sequence (0 to 420 min) and showing significant changes in its
1555 morphology throughout emergence. Note the sub-luminal and cytosolic localization of pools of
1556 Podxl2 (notably at t = 30 min, magenta arrows) suggesting enhanced trafficking of the protein
1557 and relative instability of apical polarity features, consistently with apparent fluctuation of the
1558 luminal membrane surface contacting the aortic lumen (green arrows, in particular at t = 240
1559 min). At t = 420 min, the cell has emerged and Podxl2 containing membranes remain in close
1560 contact with the membrane contacting the aortic floor. Bars:20*μ*m.
1561

1562 **Figure 5 – figure supplement 1. Model depicting the evolution of junctional interfaces**
1563 **and of the differential mobility of antero-posterior junctional complexes for EHT pol+**
1564 **and EHT pol- cell emergence types. Top panel:** EHT pol+ cell whose emergence depends
1565 on the constriction of circumferential actomyosin (orange, see Lancino et al. 2018) and the
1566 reduction of the membrane interface contacting endothelial neighbors shrinking along the
1567 longitudinal axis (horizontal double arrows) and in the 2D plane (endothelial neighbors are not
1568 depicted and are embedded in the blue X-Y plane). Presumably, the reduction of membrane
1569 interfaces relies on consumption via endocytosis. Green ovals: junctional complexes
1570 reinforced at antero-posterior poles. Green line: apical/luminal membrane with typical inward
1571 bending. **Bottom panel**: EHT pol- cell whose emergence depends on the dynamics of
1572 adhesion pools that move synchronously in 3D (X, Y, Z), both at antero-posterior poles (blue
1573 ovals) and at lateral sides of the emerging cell contacting endothelial neighbors (adjoining
1574 endothelial cells are not depicted and are embedded in the blue X-Y plane). Presumably, this
1575 type of emergence in which endothelial cells crawl over the EHT cell (curved arrows) involves,
1576 for the latter, a partial retrograde endocytic recycling of junctional complexes (opposite to the
1577 direction of emergence). Note that nuclei are not drawn at scale.
1578
1579 **Figure 5 – figure supplement 2. JAM2a and JAM3b expression and localization in**
1580 **diverse embryonic tissues.** Localization of transiently expressed eGFP-Jam2a (**A-D**) and
1581 eGFP-Jam3b (**E-G**) in 52 hpf embryos, using spinning disk confocal microscopy. Plasmid
1582 constructs were expressed under the control of the heat shock *Hsp70* promoter. For both
1583 constructs, expression was induced approximately 6 hrs before imaging, by 1hour balneation
1584 in 39°C embryo medium. All images are maximum z-projections. **A, E,** ependymal cells. White
1585 and red arrows point at reinforcement of eGFP-Jam2a and eGFP-Jam3b at apical intercellular
1586 junctions and at basolateral membranes, respectively. **B,** pronephric tubule cells. White arrows
1587 point at the reinforcement of the eGFP-Jam2a signal at apical sides of membranes of polarized

1588 cells constituting pronephric tubules. The red arrow points at baso-lateral localization of eGFP-
1589 Jam2a. **C, F,** skin epithelial cells. White arrows point at the localization of eGFP-Jam2a and
1590 eGFP-Jam3b at lateral junctional interfaces between two neighboring cells. Red arrows point
1591 at tri-cellular junctions at which the density of eGFP-Jam2a and eGFP-Jam3b is reinforced. **D,**
1592 skin epithelial cells. White arrows point at membrane protrusions. **G,** Striated muscle cells. Red
1593 arrows point at T-tubules (invagination of the sarcolemmal membranes); white arrows point at
1594 the plasma membranes of myofibrils. Bars: 20μm.
1595
1596 **Figure 6 – figure supplement 1. Examples of junctional contacts targeted by FRAP in**
1597 **the aortic landscape.** After performing z-stack acquisitions in trunk regions followed by 2D-
1598 deployment of aortic segments (**A-C**), 4 different *Tg(kdrl:eGFP-Jam3b; kdrl:nls-mKate2)* 48-
1599 55 hpf embryos were illuminated for FRAP. Panels (**A)** and (**B)** are the entire segments from
1600 which cropped images of EHT pol+ and EHT pol- cells (black asterisks) and surroundings were
1601 extracted to build the panels A and B of ***Figure 6***. Panels (**C**) and (**D**) are from 2 other embryos.
1602 The 2D-cartographies allow visualizing the junctions that were selected for FRAP, with the
1603 black arrows pointing at junctional interfaces between EHT and endothelial cells (all are in the
1604 area of tri-junctions) and the green arrows pointing at bi-junctions (Bj) or tri-junctions between
1605 endothelial cells (green asterisks). Bar = 20μm.
1606
1607 **Figure 7 – figure supplement 1. Searching for PDZ-domain containing RhoGEFs**
1608 **potentially involved in the EHT. A,** cartoons representing the domains composing the 9 PDZ
1609 domain-containing RhoGEFs that were investigated in this study (all these RhoGEFs are
1610 encoded by different genes in the zebrafish; protein respective length is not drawn at scale).
1611 **B,** results obtained from 3 independent qRT-PCR experiments and performed on material
1612 extracted from trunk regions of 35 and 48 hpf embryos obtained from incrossed
1613 *Tg(kdrl:Gal4;UAS:RFP;4xNR:dt-runx1-eGFP)* adult fishes. Statistical tests: two sided unpaired
1614 two samples Wilcoxon test, with p-values of significant differences. GEF: guanine nucleotide-

1615 exchange factor; PDZ: postsynaptic density protein of 95 kDa, Discs large and Zona
1616 occludens-1; PH: Plekstrin homology; RGS: regulator of G-protein signaling; DH: Dbl (diffuse
1617 B-cell lymphoma) homology; RBD: Ras-binding domain; DEP: Dishevelled Egl-10 and
1618 Plekstrin; InsPx4-PTPase: PtdIns(1,3,4,5)P4 phosphatidylinositol phosphatase; TIAM: T-cell-
1619 lymphoma invasion and metastasis; LARG: leukemia-associated Rho guanine-nucleotide
1620 exchange factor; PRex: PtdIns(3,4,5)P3-dependant Rac exchanger-1 and 2.
1621
1622 **Figure 7 – figure supplement 2.** Whole mount in situ hybridizations (WISH) performed on 30-
1623 32 hpf and 48-50 hpf embryos, with probes specific for all 9 PDZ-domain containing RhoGEFs
1624 that were investigated in this study. Note that all RhoGEFs are detected in the dorsal aorta of
1625 the trunk region (white arrowheads).
1626
1627 ***Figure 7 – figure supplement 3.*** **A N-terminal fragment of ArhGEF11/PDZ-RhoGEF**
1628 **localizes at junctional membranes with enrichment at antero-posterior sites of EHT**
1629 **cells. A,** domains of ArhGEF11, including its actin binding site (L/IIxxFE) and the position of
1630 exon 38 encoded peptide. The bottom cartoon represents a protein deleted from its DH-PH
1631 domains and C-terminus that are replaced by eGFP (PDZ-PRD-RGS-eGFP) to follow the
1632 localization of the truncated fusion protein in expressing cells. **B**, localization of the ArhGEF11
1633 PDZ-PRD-RGS-eGFP fusion protein after transient expression in the aorta (expression was
1634 obtained after injection of the plasmid, at the one cell stage, in the *Tg(Kdrl:Gal4;UAS:RFP)* fish
1635 line). Confocal images extracted from a time-lapse sequence (timing points t = 0 and t = 77
1636 min) and showing either the eGFP channel only (left), or the merge between the green and the
1637 red channels (RFP labels the cytoplasm). Note the localization of PDZ-PRD-RGS-eGFP at
1638 membrane interfaces at early time point of the emergence and at the rim of an emerging cell
1639 (white arrowheads, second cell from the right) and its enrichment at antero-posterior sites of
1640 an EHT pol+ cell proceeding throughout emergence (right cell, at t = 0 and t = 77 min and
1641 bottom cartoons, green arrows point at localization/concentration of PDZ-PRD-RGS-eGFP).

1642

1643 **Figure 7 – figure supplement 4. MO and CRISPR approaches to investigate the function**
1644 **of ArhGEF11/PDZ-RhoGEF in the EHT. A**, splicing MO interfering with integration of exon
1645 38. **Top panel**: cartoon representing exons/introns (not drawn at scale) composing the 3-
1646 prime region of the gene encoding for ArhGEF11, with the position of the splicing MO. **Middle**
1647 **panel**: agarose gel showing the 2 alternative mRNAs encoding for ArhGEF11 in control
1648 animals (left track, control) and after injection of the MO at the one cell stage (right track, +MO
1649 at 2 and 5ng). **Bottom panel**: ArhGEF11 DNA sequences obtained after RT-PCR, cloning and
1650 sequencing for 1 control and 2 +MO clones (+MO1, +MO3). **B**, morphologies of control and
1651 +MO injected 48 hpf embryos. Note the absence of malformations. **C**, **top panel**: ArhGEF11
1652 wild type and CRISPR-mediated 7bp deletion in the 3-prime region of exon 38 leading to a
1653 frame-shift in the ORF and a downstream premature stop codon; **middle panel**: CRISPR
1654 del/C-ter nucleotide/aa sequence and wild type nucleotide/aa sequence covering the extreme
1655 C-ter of the full-length protein; **bottom panel**: CLUSTAL 2.1 multiple sequence alignment of
1656 mouse and zebrafish C-termini highlighting the sequences of spliced variants of potentially
1657 similar activity in the regulation of ArhGEF11 activity on RhoA. Accession numbers:
1658 NP_001003912.1 and NP_001027010.1 for the mouse and Danio rerio sequence,
1659 respectively. **D,** morphologies of control and homozygous ArhGEF11$^{CRISPR\text{-}Cterdel+/+}$ 48 hpf
1660 embryos (*(Kdrl:eGFP-Jam3b; kdrl:*ArhGEF11$^{CRISPR\text{-}Cterdel+/+}$) embryos). Note the edema in the
1661 cardiac region (35 hpf embryos also exhibited retardation in blood circulation).

1662

1663 **Figure 7 – figure supplement 5. Supplementary data on the ArhGEF11/PDZ-RhoGEF**
1664 **exon 38 splicing morpholino phenotype.** *Tg(kdrl:eGFP-Jam2a; kdrl:nls-mKate2)* control (**A,**
1665 **C, E**) or MO-injected (**B, D, F**) embryos were imaged using spinning disk confocal microscopy
1666 (48-55 hpf time-window). Aorta segments (330 μm each) were imaged in the trunk region
1667 (AGM). The 2D-cartographies with delimited cellular contours in panels **A** and **B** are presented

1668 ***Figure 7A*** with the corresponding un-modified 2D-cartographies shown on top for unmasking
1669 of contours. Panels **A** and **C** illustrate 2 different segments from the same embryo. Panels **B,**
1670 **D, F** illustrate segments from 3 different embryos. (a-f) Maximum z-projections of merged nls-
1671 mkate2 and eGFP-Jam2a signals for control (a, c, e) and for ArhGEF11 exon 38 splicing
1672 morpholino (b, d, f) conditions. For panels (a) and (b), maximum z-projections of the eGFP-
1673 Jam2a signal only are also shown. (a'-f') Single z-plane images of merged nls-mkate2 and
1674 eGFP-Jam2a signals for control (a', c', e') and for ArhGEF11 exon 38 splicing morpholino (b',
1675 d', f') conditions. For **e'**, the image is a composition of 2 different z-planes from the same field
1676 (the boundaries are marked with white ticks). In right margins, magenta and green arrowheads
1677 designate the aortic floor and roof, respectively. (a''-f'') 2D-cartographies (bottom, with
1678 delineated cellular contours) obtained from eGFP-Jam2a signals for control (a'', c'', e'') and for
1679 the ArhGEF11 exon 38 splicing morpholino (b'', d'', f'') conditions, respectively. Cell contours
1680 are delineated either in blue (endothelial cells), yellow (hemogenic cells), red (morphologically
1681 characterized EHT cells, red arrows), and small cells delineated by cyan boxes
1682 (morphologically uncharacterized EHT cells and putative post-mitotic cells remaining as pairs).
1683 Cellular contours have been semi-automatically segmented along the cellular interfaces
1684 labelled with eGFP-Jam3b (see ***Materials and Methods***). White and black arrows designate
1685 hemogenic cells with their nucleus visible on the z-section. Analyses were performed on 2 x
1686 control non-injected embryos and 3 x embryos injected at the one-cell stage with the
1687 ArhGEF11 exon 38 splicing MO. Bars = 20μm.
1688
1689 **Figure 7 – figure supplement 6. Supplementary data on the ArhGEF11/PDZ-RhoGEF**
1690 **CRISPR C-ter deletion phenotype.** *(Kdrl:eGFP-Jam3b; kdrl:*ArhGEF11$^{\text{CRISPR-Cterdel+/+}}$)
1691 homozygous ArhGEF11 C-ter deletion mutants (CRISPR ArhGEF11: panels **B, D, F**) and
1692 control siblings (Control: panels **A, C, E**) were imaged using spinning disk confocal microscopy
1693 (48-55hpf time-window). Note that the genetic background of the CRISPR fish line is

1694 (Kdrl:GAL4; UAS:RFP) thus allowing the red cytosolic staining of aortic and hemogenic cells.
1695 Aorta segments (330 μm each) were imaged in the trunk region. The 2D-cartographies with
1696 delimited cellular contours in panels **A** and **B** are presented ***Figure 7B*** with the corresponding
1697 un-modified 2D-cartographies shown on top for unmasking of contours. Panels **A, C** and **D, F**
1698 illustrate 2 different segments from the same embryo. (a-f) Maximum z-projections of merged
1699 nls-mkate2 and eGFP-Jam3b signals for control (a, c, e) and for the CRISPR mutant (b, d, f)
1700 conditions. For panels (a) and (b), maximum z-projections of the eGFP-Jam2a signal only are
1701 also shown. (a'-f') Single z-plane images of merged nls-mkate2 and eGFP-Jam3b signals for
1702 control (a', c', e') and for ArhGEF11 exon 38 splicing morpholino (b', d', f') conditions. For b'
1703 and d', the image is a composition of 2 different z-planes from the same field (the boundaries
1704 are marked with white ticks). In right margins, magenta and green arrowheads designate the
1705 aortic floor and roof, respectively. (a''-f'') 2D-cartographies (bottom, with delineated cellular
1706 contours) obtained from eGFP-Jam3b signals for control (a'', c'', e'') and for the CRIPR mutant
1707 (b'', d'', f'') conditions, respectively.
1708 Cell contours are delineated either in blue (endothelial cells), yellow (hemogenic cells), red
1709 (morphologically characterized EHT cells, red arrows), and small cells delineated by cyan
1710 boxes (morphologically uncharacterized EHT cells). Cellular contours have been semi-
1711 automatically segmented along the cellular interfaces labelled with eGFP-Jam3b (see
1712 ***Materials and Methods***). White and black arrows designate hemogenic cells with their
1713 nucleus visible on the z-section. Analyses were performed on 2 x wild-type siblings for controls
1714 and 2 x mutant embryos whose mutation was confirmed by DNA sequencing. Bars = 20μm.
1715

References

Adamo, Luigi, Olaia Naveiras, Pamela L. Wenzel, Shannon McKinney-Freeman, Peter J. Mack, Jorge Gracia-Sancho, Astrid Suchy-Dicey, et al. 2009. "Biomechanical Forces Promote Embryonic Haematopoiesis." *Nature* 459 (7250): 1131–35. https://doi.org/10.1038/nature08073.

Akitake, Courtney M., Michelle Macurak, Marnie E. Halpern, and Mary G. Goll. 2011. "Transgenerational Analysis of Transcriptional Silencing in Zebrafish." *Developmental Biology* 352 (2): 191–201. https://doi.org/10.1016/j.ydbio.2011.01.002.

Barone, Cristiana, Roberto Orsenigo, Raffaella Meneveri, Silvia Brunelli, and Emanuele Azzoni. 2022. "One Size Does Not Fit All: Heterogeneity in Developmental Hematopoiesis." *Cells* 11 (6): 1061. https://doi.org/10.3390/cells11061061.

Bayless, Kayla J., and George E. Davis. 2002. "The Cdc42 and Rac1 GTPases Are Required for Capillary Lumen Formation in Three-Dimensional Extracellular Matrices." *Journal of Cell Science* 115 (6): 1123–36. https://doi.org/10.1242/jcs.115.6.1123.

Bengtsson, Henrik. 2022. *MatrixStats: Functions That Apply to Rows and Columns of Matrices (and to Vectors)*. https://github.com/HenrikBengtsson/matrixStats.

Bertrand, Julien Y., Neil C. Chi, Buyung Santoso, Shutian Teng, Didier Y. R. Stainier, and David Traver. 2010. "Haematopoietic Stem Cells Derive Directly from Aortic Endothelium during Development." *Nature* 464 (7285): 108–11. https://doi.org/10.1038/nature08738.

Bertrand, Julien Y., Albert D. Kim, Emily P. Violette, David L. Stachura, Jennifer L. Cisson, and David Traver. 2007. "Definitive Hematopoiesis Initiates through a Committed Erythromyeloid Progenitor in the Zebrafish Embryo." *Development* 134 (23): 4147–56. https://doi.org/10.1242/dev.012385.

Boisset, Jean-Charles, Wiggert van Cappellen, Charlotte Andrieu-Soler, Niels Galjart, Elaine Dzierzak, and Catherine Robin. 2010. "In Vivo Imaging of Haematopoietic Cells Emerging from the Mouse Aortic Endothelium." *Nature* 464 (7285): 116–20. https://doi.org/10.1038/nature08764.

Bonkhofer, Florian, Rossella Rispoli, Philip Pinheiro, Monika Krecsmarik, Janina Schneider-Swales, Ingrid Ho Ching Tsang, Marella de Bruijn, Rui Monteiro, Tessa Peterkin, and Roger Patient. 2019. "Blood Stem Cell-Forming Haemogenic Endothelium in Zebrafish Derives from Arterial Endothelium." *Nature Communications* 10 (1): 3577. https://doi.org/10.1038/s41467-019-11423-2.

Bosveld, Floris, Zhimin Wang, and Yohanns Bellaïche. 2018. "Tricellular Junctions: A Hot Corner of Epithelial Biology." *Current Opinion in Cell Biology*, Cell Dynamics, 54 (October): 80–88. https://doi.org/10.1016/j.ceb.2018.05.002.

Bruijn, Marella F. T. R de, Xiaoqian Ma, Catherine Robin, Katrin Ottersbach, Maria-Jose Sanchez, and Elaine Dzierzak. 2002. "Hematopoietic Stem Cells Localize to the Endothelial Cell Layer in the Midgestation Mouse Aorta." *Immunity* 16 (5): 673–83. https://doi.org/10.1016/S1074-7613(02)00313-8.

Bryant, David M., Julie Roignot, Anirban Datta, Arend W. Overeem, Minji Kim, Wei Yu, Xiao Peng, et al. 2014. "A Molecular Switch for the Orientation of Epithelial Cell Polarization." *Developmental Cell* 31 (2): 171–87. https://doi.org/10.1016/j.devcel.2014.08.027.

Buckley, Clare E., and Daniel St Johnston. 2022. "Apical–Basal Polarity and the Control of Epithelial Form and Function." *Nature Reviews Molecular Cell Biology* 23 (8): 559–77. https://doi.org/10.1038/s41580-022-00465-y.

Burns, Caroline Erter, Tony DeBlasio, Yi Zhou, Jin Zhang, Leonard Zon, and Stephen D Nimer. 2002. "Isolation and Characterization of Runxa and Runxb, Zebrafish Members of the Runt Family of Transcriptional Regulators." *Experimental Hematology* 30 (12): 1381–89. https://doi.org/10.1016/S0301-472X(02)00955-4.

Butko, Emerald, Martin Distel, Claire Pouget, Bart Weijts, Isao Kobayashi, Kevin Ng, Christian Mosimann, et al. 2015. "Gata2b Is a Restricted Early Regulator of Hemogenic Endothelium in the Zebrafish Embryo." *Development* 142 (6): 1050–61. https://doi.org/10.1242/dev.119180.

Campinho, Pedro, Paola Lamperti, Francesco Boselli, Andrej Vilfan, and Julien Vermot. 2020. "Blood Flow Limits Endothelial Cell Extrusion in the Zebrafish Dorsal Aorta." *Cell Reports* 31 (2): 107505. https://doi.org/10.1016/j.celrep.2020.03.069.

Chalin, Dmitrii, Charlotte Bureau, Andrea Parmeggiani, Sergei Rochal, Karima Kissa, and Ivan Golushko. 2021. "Modeling and Live Imaging of Mechanical Instabilities in the Zebrafish Aorta during Hematopoiesis." *Scientific Reports* 11 (1): 9316. https://doi.org/10.1038/s41598-021-88667-w.

Chi, Neil C., Robin M. Shaw, Sarah De Val, Guson Kang, Lily Y. Jan, Brian L. Black, and Didier Y. R. Stainier. 2008. "Foxn4 Directly Regulates Tbx2b Expression and Atrioventricular Canal Formation." *Genes & Development* 22 (6): 734–39. https://doi.org/10.1101/gad.1629408.

Chikumi, Hiroki, Ana Barac, Babak Behbahani, Yuan Gao, Hidemi Teramoto, Yi Zheng, and J. Silvio Gutkind. 2004. "Homo- and Hetero-Oligomerization of PDZ-RhoGEF, LARG and P115RhoGEF by Their C-Terminal Region Regulates Their in Vivo Rho GEF Activity and Transforming Potential." *Oncogene* 23 (1): 233–40. https://doi.org/10.1038/sj.onc.1207012.

Ciau-Uitz, Aldo, Rui Monteiro, Arif Kirmizitas, and Roger Patient. 2014. "Developmental Hematopoiesis: Ontogeny, Genetic Programming and Conservation." *Experimental Hematology*, Genomics and Model Organisms: New Horizons for Experimental Hematology, 42 (8): 669–83. https://doi.org/10.1016/j.exphem.2014.06.001.

Clarke, Erik, and Scott Sherrill-Mix. 2017. *Ggbeeswarm: Categorical Scatter (Violin Point) Plots*. https://github.com/eclarke/ggbeeswarm.

Cumano, Ana, Françoise Dieterlen-Lievre, and Isabelle Godin. 1996. "Lymphoid Potential, Probed before Circulation in Mouse, Is Restricted to Caudal Intraembryonic Splanchnopleura." *Cell* 86 (6): 907–16. https://doi.org/10.1016/S0092-8674(00)80166-X.

Daniel, Michael G., David Sachs, Jeffrey M. Bernitz, Yesai Fstkchyan, Katrina Rapp, Namita Satija, Kenneth Law, et al. 2019. "Induction of Human Hemogenesis in Adult Fibroblasts by Defined Factors and Hematopoietic Coculture." *FEBS Letters* 593 (23): 3266–87. https://doi.org/10.1002/1873-3468.13621.

Davis, George E., Kayla J. Bayless, and Anil Mavila. 2002. "Molecular Basis of Endothelial Cell Morphogenesis in Three-Dimensional Extracellular Matrices." *The Anatomical Record* 268 (3): 252–75. https://doi.org/10.1002/ar.10159.

De Chaumont, Fabrice, Stéphane Dallongeville, Nicolas Chenouard, Nicolas Hervé, Sorin Pop, Thomas Provoost, Vannary Meas-Yedid, et al. 2012. "Icy: An Open Bioimage Informatics Platform for Extended Reproducible Research." *Nature Methods* 9 (7): 690–96. https://doi.org/10.1038/nmeth.2075.

Dignum, Tessa, Barbara Varnum-Finney, Sanjay R. Srivatsan, Stacey Dozono, Olivia Waltner, Adam M. Heck, Takashi Ishida, et al. 2021. "Multipotent Progenitors and Hematopoietic Stem Cells Arise Independently from Hemogenic Endothelium in the Mouse Embryo." *Cell Reports* 36 (11): 109675. https://doi.org/10.1016/j.celrep.2021.109675.

Dufour, Alexandre, Roman Thibeaux, Elisabeth Labruyere, Nancy Guillen, and Jean-Christophe Olivo-Marin. 2011. "3-D Active Meshes: Fast Discrete Deformable Models for Cell Tracking in 3-D Time-Lapse Microscopy." *IEEE Transactions on Image Processing* 20 (7): 1925–37. https://doi.org/10.1109/TIP.2010.2099125.

Ebnet, Klaus. 2017. "Junctional Adhesion Molecules (JAMs): Cell Adhesion Receptors With Pleiotropic Functions in Cell Physiology and Development." *Physiological Reviews* 97 (4): 1529–54. https://doi.org/10.1152/physrev.00004.2017.

Ebnet, Klaus, Michel Aurrand-Lions, Annegret Kuhn, Friedemann Kiefer, Stefan Butz, Kerstin Zander, Maria-Katharina Meyer Zu Brickwedde, Atsushi Suzuki, Beat A. Imhof, and Dietmar Vestweber. 2003. "The Junctional Adhesion Molecule (JAM) Family Members JAM-2 and JAM-3 Associate with the Cell Polarity Protein PAR-3: A Possible Role for JAMs in Endothelial Cell Polarity." *Journal of Cell Science* 116 (19): 3879–91. https://doi.org/10.1242/jcs.00704.

Ebnet, Klaus, and Volker Gerke. 2022. "Rho and Rab Family Small GTPases in the Regulation of Membrane Polarity in Epithelial Cells." *Frontiers in Cell and Developmental Biology* 10. https://www.frontiersin.org/articles/10.3389/fcell.2022.948013.

Ebnet, Klaus, Daniel Kummer, Tim Steinbacher, Amrita Singh, Masanori Nakayama, and Maja Matis. 2018. "Regulation of Cell Polarity by Cell Adhesion Receptors." *Seminars in Cell & Developmental Biology*, Cell Polarity and Planar Cell Polarity Proteins, 81 (September): 2–12. https://doi.org/10.1016/j.semcdb.2017.07.032.

Ebnet, Klaus, Atsushi Suzuki, Yosuke Horikoshi, Tomonori Hirose, Maria-Katharina Meyer zu Brickwedde, Shigeo Ohno, and Dietmar Vestweber. 2001. "The Cell Polarity Protein ASIP/PAR-3 Directly Associates with Junctional Adhesion Molecule (JAM)." *The EMBO Journal* 20 (14): 3738–48. https://doi.org/10.1093/emboj/20.14.3738.

Eilken, Hanna M., Shin-Ichi Nishikawa, and Timm Schroeder. 2009. "Continuous Single-Cell Imaging of Blood Generation from Haemogenic Endothelium." *Nature* 457 (7231): 896–900. https://doi.org/10.1038/nature07760.

Frame, Jenna M., Katherine H. Fegan, Simon J. Conway, Kathleen E. McGrath, and James Palis. 2016. "Definitive Hematopoiesis in the Yolk Sac Emerges from Wnt-Responsive Hemogenic Endothelium Independently of Circulation and Arterial Identity." *Stem Cells* 34 (2): 431–44. https://doi.org/10.1002/stem.2213.

Gama-Norton, Leonor, Eva Ferrando, Cristina Ruiz-Herguido, Zhenyi Liu, Jordi Guiu, Abul B. M. M. K. Islam, Sung-Uk Lee, et al. 2015. "Notch Signal Strength Controls Cell Fate in the Haemogenic Endothelium." *Nature Communications* 6 (1): 8510. https://doi.org/10.1038/ncomms9510.

Ganuza, Miguel, Brandon Hadland, Ashley Chabot, Chen Li, Guolian Kang, Irwin Bernstein, and Shannon McKinney-Freeman. 2017. "Murine Hemogenic Endothelial Precursors Display Heterogeneous Hematopoietic Potential Ex Vivo." *Experimental Hematology* 51 (July): 25-35.e6. https://doi.org/10.1016/j.exphem.2017.04.006.

Gao, Long, Joanna Tober, Peng Gao, Changya Chen, Kai Tan, and Nancy A. Speck. 2018. "RUNX1 and the Endothelial Origin of Blood." *Experimental Hematology* 68 (December): 2–9. https://doi.org/10.1016/j.exphem.2018.10.009.

Garcia-Porrero, Juan A., Isabelle E. Godin, and Françoise Dieterlen-Lièvre. 1995. "Potential Intraembryonic Hemogenic Sites at Pre-Liver Stages in the Mouse." *Anatomy and Embryology* 192 (5): 425–35. https://doi.org/10.1007/BF00240375.

Garnier, Simon. 2021. *Viridis: Colorblind-Friendly Color Maps for R*. https://CRAN.R-project.org/package=viridis.

Garrido-Urbani, S., P. F. Bradfield, and B. A. Imhof. 2014. "Tight Junction Dynamics: The Role of Junctional Adhesion Molecules (JAMs)." *Cell and Tissue Research* 355 (3): 701–15. https://doi.org/10.1007/s00441-014-1820-1.

Ghosn, Eliver, Momoko Yoshimoto, Hiromitsu Nakauchi, Irving L. Weissman, and Leonore A. Herzenberg. 2019. "Hematopoietic Stem Cell-Independent Hematopoiesis and the Origins of Innate-like B Lymphocytes." *Development* 146 (15): dev170571. https://doi.org/10.1242/dev.170571.

Grosjean, Philippe. 2019. *SciViews: SciViews - Main Package*. https://CRAN.R-project.org/package=SciViews.

Gudipaty, Swapna Aravind, and Jody Rosenblatt. 2017. "Epithelial Cell Extrusion: Pathways and Pathologies." *Seminars in Cell & Developmental Biology*, Extracellular Vesicles, 67 (July): 132–40. https://doi.org/10.1016/j.semcdb.2016.05.010.

Hadland, Brandon, and Momoko Yoshimoto. 2018. “Many Layers of Embryonic Hematopoiesis: New Insights into B-Cell Ontogeny and the Origin of Hematopoietic Stem Cells.” *Experimental Hematology* 60 (April): 1–9. https://doi.org/10.1016/j.exphem.2017.12.008.

Herbert, Shane P., Jan Huisken, Tyson N. Kim, Morri E. Feldman, Benjamin T. Houseman, Rong A. Wang, Kevan M. Shokat, and Didier Y. R. Stainier. 2009. “Arterial-Venous Segregation by Selective Cell Sprouting: An Alternative Mode of Blood Vessel Formation.” *Science* 326 (5950): 294–98. https://doi.org/10.1126/science.1178577.

Herwig, Lukas, Yannick Blum, Alice Krudewig, Elin Ellertsdottir, Anna Lenard, Heinz-Georg Belting, and Markus Affolter. 2011. “Distinct Cellular Mechanisms of Blood Vessel Fusion in the Zebrafish Embryo.” *Current Biology* 21 (22): 1942–48. https://doi.org/10.1016/j.cub.2011.10.016.

Itoh, Masahiko. 2013. “ARHGEF11, a Regulator of Junction-Associated Actomyosin in Epithelial Cells.” *Tissue Barriers* 1 (2): e24221. https://doi.org/10.4161/tisb.24221.

Itoh, Masahiko, Derek C. Radisky, Masaaki Hashiguchi, and Hiroyuki Sugimoto. 2017. “The Exon 38-Containing ARHGEF11 Splice Isoform Is Differentially Expressed and Is Required for Migration and Growth in Invasive Breast Cancer Cells.” *Oncotarget* 8 (54): 92157–70. https://doi.org/10.18632/oncotarget.20985.

Itoh, Masahiko, Hiroyuki Sasaki, Mikio Furuse, Harunobu Ozaki, Toru Kita, and Shoichiro Tsukita. 2001. “Junctional Adhesion Molecule (JAM) Binds to PAR-3.” *Journal of Cell Biology* 154 (3): 491–98. https://doi.org/10.1083/jcb.200103047.

Itoh, Masahiko, Sachiko Tsukita, Yuji Yamazaki, and Hiroyuki Sugimoto. 2012. “Rho GTP Exchange Factor ARHGEF11 Regulates the Integrity of Epithelial Junctions by Connecting ZO-1 and RhoA-Myosin II Signaling.” *Proceedings of the National Academy of Sciences* 109 (25): 9905–10. https://doi.org/10.1073/pnas.1115063109.

Ivanovs, Andrejs, Stanislav Rybtsov, Elizabeth S. Ng, Edouard G. Stanley, Andrew G. Elefanty, and Alexander Medvinsky. 2017. “Human Haematopoietic Stem Cell Development: From the Embryo to the Dish.” *Development* 144 (13): 2323–37. https://doi.org/10.1242/dev.134866.

Ivanovs, Andrejs, Stanislav Rybtsov, Lindsey Welch, Richard A. Anderson, Marc L. Turner, and Alexander Medvinsky. 2011. “Highly Potent Human Hematopoietic Stem Cells First Emerge in the Intraembryonic Aorta-Gonad-Mesonephros Region.” *Journal of Experimental Medicine* 208 (12): 2417–27. https://doi.org/10.1084/jem.20111688.

Jaffredo, Thierry, Rodolphe Gautier, Anne Eichmann, and Françoise Dieterlen-Lièvre. 1998. “Intraaortic Hemopoietic Cells Are Derived from Endothelial Cells during Ontogeny.” *Development* 125 (22): 4575–83. https://doi.org/10.1242/dev.125.22.4575.

Jaffredo, Thierry, and Laurent Yvernogeau. 2014. “How the Avian Model Has Pioneered the Field of Hematopoietic Development.” *Experimental Hematology*, Genomics and Model Organisms: New Horizons for Experimental Hematology, 42 (8): 661–68. https://doi.org/10.1016/j.exphem.2014.05.009.

Jin, Suk-Won, Dimitris Beis, Tracy Mitchell, Jau-Nian Chen, and Didier Y. R. Stainier. 2005. “Cellular and Molecular Analyses of Vascular Tube and Lumen Formation in Zebrafish.” *Development* 132 (23): 5199–5209. https://doi.org/10.1242/dev.02087.

Kalev-Zylinska, Maggie L., Julia A. Horsfield, Maria Vega C. Flores, John H. Postlethwait, Maria R. Vitas, Andrea M. Baas, Philip S. Crosier, and Kathryn E. Crosier. 2002. “Runx1 Is Required for Zebrafish Blood and Vessel Development and Expression of a Human RUNX1-CBF2T1 Transgene Advances a Model for Studies of Leukemogenesis.” *Development* 129 (8): 2015–30. https://doi.org/10.1242/dev.129.8.2015.

Kamei, Makoto, W. Brian Saunders, Kayla J. Bayless, Louis Dye, George E. Davis, and Brant M. Weinstein. 2006. “Endothelial Tubes Assemble from Intracellular Vacuoles in Vivo.” *Nature* 442 (7101): 453–56. https://doi.org/10.1038/nature04923.

Kassambara, Alboukadel. 2020. *Ggpubr: Ggplot2 Based Publication Ready Plots*. https://rpkgs.datanovia.com/ggpubr/.

Kataoka, Hiroko, Mitsuo Ochi, Koh-ichi Enomoto, and Akira Yamaguchi. 2000. "Cloning and Embryonic Expression Patterns of the Zebrafish Runt Domain Genes, Runxa and Runxb." *Mechanisms of Development* 98 (1): 139–43. https://doi.org/10.1016/S0925-4773(00)00445-7.

Kimmel, Charles B., William W. Ballard, Seth R. Kimmel, Bonnie Ullmann, and Thomas F. Schilling. 1995. "Stages of Embryonic Development of the Zebrafish." *Developmental Dynamics* 203 (3): 253–310. https://doi.org/10.1002/aja.1002030302.

Kissa, Karima, and Philippe Herbomel. 2010. "Blood Stem Cells Emerge from Aortic Endothelium by a Novel Type of Cell Transition." *Nature* 464 (7285): 112–15. https://doi.org/10.1038/nature08761.

Kobayashi, Isao, Jingjing Kobayashi-Sun, Yuto Hirakawa, Madoka Ouchi, Koyuki Yasuda, Hiroyasu Kamei, Shigetomo Fukuhara, and Masaaki Yamaguchi. 2020. "Dual Role of Jam3b in Early Hematopoietic and Vascular Development." *Development* 147 (1): dev181040. https://doi.org/10.1242/dev.181040.

Lagendijk, Anne Karine, Alpha S Yap, and Benjamin M Hogan. 2014. "Endothelial Cell–Cell Adhesion during Zebrafish Vascular Development." *Cell Adhesion & Migration* 8 (2): 136–45. https://doi.org/10.4161/cam.28229.

Lancino, Mylene, Sara Majello, Sebastien Herbert, Fabrice De Chaumont, Jean-Yves Tinevez, Jean-Christophe Olivo-Marin, Philippe Herbomel, and Anne Schmidt. 2018. "Anisotropic Organization of Circumferential Actomyosin Characterizes Hematopoietic Stem Cells Emergence in the Zebrafish." *ELife* 7 (August): e37355. https://doi.org/10.7554/eLife.37355.

Lancrin, Christophe, Milena Mazan, Monika Stefanska, Rahima Patel, Monika Lichtinger, Guilherme Costa, Özge Vargel, et al. 2012. "GFI1 and GFI1B Control the Loss of Endothelial Identity of Hemogenic Endothelium during Hematopoietic Commitment." *Blood* 120 (2): 314–22. https://doi.org/10.1182/blood-2011-10-386094.

Lee, SungKyoung, Benjamin Cieply, Yueqin Yang, Natoya Peart, Carl Glaser, Patricia Chan, and Russ P. Carstens. 2018. "Esrp1-Regulated Splicing of Arhgef11 Isoforms Is Required for Epithelial Tight Junction Integrity." *Cell Reports* 25 (9): 2417-2430.e5. https://doi.org/10.1016/j.celrep.2018.10.097.

Lie-A-Ling, Michael, Elli Marinopoulou, Yaoyong Li, Rahima Patel, Monika Stefanska, Constanze Bonifer, Crispin Miller, Valerie Kouskoff, and Georges Lacaud. 2014. "RUNX1 Positively Regulates a Cell Adhesion and Migration Program in Murine Hemogenic Endothelium Prior to Blood Emergence." *Blood* 124 (11): e11–20. https://doi.org/10.1182/blood-2014-04-572958.

Lundin, Vanessa, Wade W. Sugden, Lindsay N. Theodore, Patricia M. Sousa, Areum Han, Stephanie Chou, Paul J. Wrighton, et al. 2020. "YAP Regulates Hematopoietic Stem Cell Formation in Response to the Biomechanical Forces of Blood Flow." *Developmental Cell* 52 (4): 446-460.e5. https://doi.org/10.1016/j.devcel.2020.01.006.

Mack, Natalie Ann, and Marios Georgiou. 2014. "The Interdependence of the Rho GTPases and Apicobasal Cell Polarity." *Small GTPases* 5 (2): e973768. https://doi.org/10.4161/21541248.2014.973768.

Marshall, Caroline J., and Adrian J. Thrasher. 2001. "The Embryonic Origins of Human Haematopoiesis." *British Journal of Haematology* 112 (4): 838–50. https://doi.org/10.1046/j.1365-2141.2001.02537.x.

Meder, Doris, Anna Shevchenko, Kai Simons, and Joachim Füllekrug. 2005. "Gp135/Podocalyxin and NHERF-2 Participate in the Formation of a Preapical Domain during Polarization of MDCK Cells." *Journal of Cell Biology* 168 (2): 303–13. https://doi.org/10.1083/jcb.200407072.

Medvinsky, Alexander, and Elaine Dzierzak. 1996. “Definitive Hematopoiesis Is Autonomously Initiated by the AGM Region.” *Cell* 86 (6): 897–906. https://doi.org/10.1016/S0092-8674(00)80165-8.

Medvinsky, Alexander L., Nina L. Samoylina, Albrecht M. Müller, and Elaine A. Dzierzak. 1993. “An Early Pre-Liver Intraembryonic Source of CFU-S in the Developing Mouse.” *Nature* 364 (6432): 64–67. https://doi.org/10.1038/364064a0.

Monteiro, Rui, Philip Pinheiro, Nicola Joseph, Tessa Peterkin, Jana Koth, Emmanouela Repapi, Florian Bonkhofer, Arif Kirmizitas, and Roger Patient. 2016. “Transforming Growth Factor β Drives Hemogenic Endothelium Programming and the Transition to Hematopoietic Stem Cells.” *Developmental Cell* 38 (4): 358–70. https://doi.org/10.1016/j.devcel.2016.06.024.

Moreno-Mateos, Miguel A., Charles E. Vejnar, Jean-Denis Beaudoin, Juan P. Fernandez, Emily K. Mis, Mustafa K. Khokha, and Antonio J. Giraldez. 2015. “CRISPRscan: Designing Highly Efficient SgRNAs for CRISPR-Cas9 Targeting in Vivo.” *Nature Methods* 12 (10): 982–88. https://doi.org/10.1038/nmeth.3543.

Müller, A. M., A. Medvinsky, J. Strouboulis, F. Grosveld, and E. Dzierzak. 1994. “Development of Hematopoietic Stem Cell Activity in the Mouse Embryo.” *Immunity* 1 (4): 291–301. https://doi.org/10.1016/1074-7613(94)90081-7.

Murayama, Emi, Karima Kissa, Agustin Zapata, Elodie Mordelet, Valérie Briolat, Hui-Feng Lin, Robert I. Handin, and Philippe Herbomel. 2006. “Tracing Hematopoietic Precursor Migration to Successive Hematopoietic Organs during Zebrafish Development.” *Immunity* 25 (6): 963–75. https://doi.org/10.1016/j.immuni.2006.10.015.

Nielsen, Julie S., and Kelly M. McNagny. 2008. “Novel Functions of the CD34 Family.” *Journal of Cell Science* 121 (22): 3683–92. https://doi.org/10.1242/jcs.037507.

Nieto, M. Angela, Ruby Yun-Ju Huang, Rebecca A. Jackson, and Jean Paul Thiery. 2016. “EMT: 2016.” *Cell* 166 (1): 21–45. https://doi.org/10.1016/j.cell.2016.06.028.

Nishimura, Tamako, Hisao Honda, and Masatoshi Takeichi. 2012. “Planar Cell Polarity Links Axes of Spatial Dynamics in Neural-Tube Closure.” *Cell* 149 (5): 1084–97. https://doi.org/10.1016/j.cell.2012.04.021.

North, Trista E., Marella F. T. R. de Bruijn, Terryl Stacy, Laleh Talebian, Evan Lind, Catherine Robin, Michael Binder, Elaine Dzierzak, and Nancy A. Speck. 2002. “Runx1 Expression Marks Long-Term Repopulating Hematopoietic Stem Cells in the Midgestation Mouse Embryo.” *Immunity* 16 (5): 661–72. https://doi.org/10.1016/S1074-7613(02)00296-0.

North, Trista E., Wolfram Goessling, Marian Peeters, Pulin Li, Craig Ceol, Allegra M. Lord, Gerhard J. Weber, et al. 2009. “Hematopoietic Stem Cell Development Is Dependent on Blood Flow.” *Cell* 137 (4): 736–48. https://doi.org/10.1016/j.cell.2009.04.023.

North, Trista, Ting-Lei Gu, Terryl Stacy, Qing Wang, Louisa Howard, Michael Binder, Miguel Marín-Padilla, and Nancy A. Speck. 1999. “*Cbfa2* Is Required for the Formation of Intra-Aortic Hematopoietic Clusters.” *Development* 126 (11): 2563–75. https://doi.org/10.1242/dev.126.11.2563.

Olayioye, Monilola A., Bettina Noll, and Angelika Hausser. 2019. “Spatiotemporal Control of Intracellular Membrane Trafficking by Rho GTPases.” *Cells* 8 (12): 1478. https://doi.org/10.3390/cells8121478.

Orkin, Stuart H., and Leonard I. Zon. 2008. “Hematopoiesis: An Evolving Paradigm for Stem Cell Biology.” *Cell* 132 (4): 631–44. https://doi.org/10.1016/j.cell.2008.01.025.

Padfield, Daniel, and Granville Matheson. 2020. *Nls.Multstart: Robust Non-Linear Regression Using AIC Scores*. https://CRAN.R-project.org/package=nls.multstart.

Patil, Indrajeet. 2022. *Ggstatsplot: Ggplot2 Based Plots with Statistical Details*. https://CRAN.R-project.org/package=ggstatsplot.

Pei, Duanqing, Xiaodong Shu, Ama Gassama-Diagne, and Jean Paul Thiery. 2019. “Mesenchymal–Epithelial Transition in Development and Reprogramming.” *Nature Cell Biology* 21 (1): 44–53. https://doi.org/10.1038/s41556-018-0195-z.

Pradella, Davide, Chiara Naro, Claudio Sette, and Claudia Ghigna. 2017. “EMT and Stemness: Flexible Processes Tuned by Alternative Splicing in Development and Cancer Progression.” *Molecular Cancer* 16 (1): 8. https://doi.org/10.1186/s12943-016-0579-2.

Ram, Karthik, and Hadley Wickham. 2018. *Wesanderson: A Wes Anderson Palette Generator*. https://github.com/karthik/wesanderson.

Ridley, Anne J. 2006. “Rho GTPases and Actin Dynamics in Membrane Protrusions and Vesicle Trafficking.” *Trends in Cell Biology*, Membrane Dynamics, 16 (10): 522–29. https://doi.org/10.1016/j.tcb.2006.08.006.

Robert-Moreno, Àlex, Jordi Guiu, Cristina Ruiz-Herguido, M. Eugenia López, Julia Inglés-Esteve, Lluis Riera, Alex Tipping, et al. 2008. “Impaired Embryonic Haematopoiesis yet Normal Arterial Development in the Absence of the Notch Ligand Jagged1.” *The EMBO Journal* 27 (13): 1886–95.

Rodriguez-Boulan, Enrique, Anne Müsch, and Andre Le Bivic. 2004. “Epithelial Trafficking: New Routes to Familiar Places.” *Current Opinion in Cell Biology* 16 (4): 436–42. https://doi.org/10.1016/j.ceb.2004.06.013.

Román-Fernández, Alvaro, and David M. Bryant. 2016. “Complex Polarity: Building Multicellular Tissues Through Apical Membrane Traffic.” *Traffic* 17 (12): 1244–61. https://doi.org/10.1111/tra.12417.

Rossman, Kent L., Channing J. Der, and John Sondek. 2005. “GEF Means Go: Turning on RHO GTPases with Guanine Nucleotide-Exchange Factors.” *Nature Reviews Molecular Cell Biology* 6 (2): 167–80. https://doi.org/10.1038/nrm1587.

Sato, Yuki, Mugiho Shigematsu, Maria Shibata-Kanno, Sho Maejima, Chie Tamura, and Hirotaka Sakamoto. 2023. “Aquaporin Regulates Cell Rounding through Vacuole Formation during Endothelial-to-Hematopoietic Transition.” *Development* 150 (11): dev201275. https://doi.org/10.1242/dev.201275.

Sehnert, Amy J., Anja Huq, Brant M. Weinstein, Charline Walker, Mark Fishman, and Didier Y. R. Stainier. 2002. “Cardiac Troponin T Is Essential in Sarcomere Assembly and Cardiac Contractility.” *Nature Genetics* 31 (1): 106–10. https://doi.org/10.1038/ng875.

Shapiro, Irina M., Albert W. Cheng, Nicholas C. Flytzanis, Michele Balsamo, John S. Condeelis, Maja H. Oktay, Christopher B. Burge, and Frank B. Gertler. 2011. “An EMT–Driven Alternative Splicing Program Occurs in Human Breast Cancer and Modulates Cellular Phenotype.” *PLOS Genetics* 7 (8): e1002218. https://doi.org/10.1371/journal.pgen.1002218.

Sood, Raman, Milton A. English, Christiane L. Belele, Hao Jin, Kevin Bishop, Rebecca Haskins, Mary Cathleen McKinney, et al. 2010. “Development of Multilineage Adult Hematopoiesis in the Zebrafish with a Runx1 Truncation Mutation.” *Blood* 115 (14): 2806–9. https://doi.org/10.1182/blood-2009-08-236729.

Staneva, Ralitza, and Romain Levayer. 2023. “Chapter Five - Cell Polarity and Extrusion: How to Polarize Extrusion and Extrude Misspolarized Cells?” In *Current Topics in Developmental Biology*, edited by ULRICH Tepass, 154:131–67. Cell Polarity in Development and Disease. Academic Press. https://doi.org/10.1016/bs.ctdb.2023.02.010.

Strilić, Boris, Jan Eglinger, Michael Krieg, Martin Zeeb, Jennifer Axnick, Pavel Babál, Daniel J. Müller, and Eckhard Lammert. 2010. “Electrostatic Cell-Surface Repulsion Initiates Lumen Formation in Developing Blood Vessels.” *Current Biology* 20 (22): 2003–9. https://doi.org/10.1016/j.cub.2010.09.061.

Strilić, Boris, Tomáš Kučera, Jan Eglinger, Michael R. Hughes, Kelly M. McNagny, Sachiko Tsukita, Elisabetta Dejana, Napoleone Ferrara, and Eckhard Lammert. 2009. “The Molecular Basis of Vascular Lumen Formation in the Developing Mouse Aorta.” *Developmental Cell* 17 (4): 505–15. https://doi.org/10.1016/j.devcel.2009.08.011.

Swiers, Gemma, Claudia Baumann, John O’Rourke, Eleni Giannoulatou, Stephen Taylor, Anagha Joshi, Victoria Moignard, et al. 2013. “Early Dynamic Fate Changes in

Haemogenic Endothelium Characterized at the Single-Cell Level." *Nature Communications* 4 (1): 2924. https://doi.org/10.1038/ncomms3924.

Tian, Ye, Jin Xu, Shachuan Feng, Sicong He, Shizheng Zhao, Lu Zhu, Wan Jin, et al. 2017. "The First Wave of T Lymphopoiesis in Zebrafish Arises from Aorta Endothelium Independent of Hematopoietic Stem Cells." *Journal of Experimental Medicine* 214 (11): 3347–60. https://doi.org/10.1084/jem.20170488.

Weijts, Bart, Laurent Yvernogeau, and Catherine Robin. 2021. "Recent Advances in Developmental Hematopoiesis: Diving Deeper With New Technologies." *Frontiers in Immunology* 12. https://www.frontiersin.org/articles/10.3389/fimmu.2021.790379.

Wickham, Hadley. 2016. *Ggplot2: Elegant Graphics for Data Analysis*. Springer-Verlag New York. https://ggplot2.tidyverse.org.

Wickham. 2022. *Stringr: Simple, Consistent Wrappers for Common String Operations*. https://CRAN.R-project.org/package=stringr.

Wickham, Hadley, Romain François, Lionel Henry, Kirill Müller, and Davis Vaughan. 2023. *Dplyr: A Grammar of Data Manipulation*. https://CRAN.R-project.org/package=dplyr.

Wickham, Hadley, Jim Hester, and Jennifer Bryan. 2022. *Readr: Read Rectangular Text Data*. https://CRAN.R-project.org/package=readr.

Wilke, Claus O. 2020. *Cowplot: Streamlined Plot Theme and Plot Annotations for Ggplot2*. https://wilkelab.org/cowplot/.

Wu, Yinyu, and Karen K. Hirschi. 2021. "Regulation of Hemogenic Endothelial Cell Development and Function." *Annual Review of Physiology* 83 (February): 17–37. https://doi.org/10.1146/annurev-physiol-021119-034352.

Xia, Jun, Mengyao Liu, Caiying Zhu, Shicheng Liu, Lanlan Ai, Dongyuan Ma, Ping Zhu, Lu Wang, and Feng Liu. 2023. "Activation of Lineage Competence in Hemogenic Endothelium Precedes the Formation of Hematopoietic Stem Cell Heterogeneity." *Cell Research*, April, 1–16. https://doi.org/10.1038/s41422-023-00797-0.

Xiao, Nan. 2018. *Ggsci: Scientific Journal and Sci-Fi Themed Color Palettes for Ggplot2*. https://CRAN.R-project.org/package=ggsci.

Xie, Yihui, Joe Cheng, and Xianying Tan. 2022. *DT: A Wrapper of the JavaScript Library DataTables*. https://github.com/rstudio/DT.

Yoshimoto, Momoko, Encarnacion Montecino-Rodriguez, Michael J. Ferkowicz, Prashanth Porayette, W. Christopher Shelley, Simon J. Conway, Kenneth Dorshkind, and Mervin C. Yoder. 2011. "Embryonic Day 9 Yolk Sac and Intra-Embryonic Hemogenic Endothelium Independently Generate a B-1 and Marginal Zone Progenitor Lacking B-2 Potential." *Proceedings of the National Academy of Sciences* 108 (4): 1468–73. https://doi.org/10.1073/pnas.1015841108.

Yoshimoto, Momoko, Prashanth Porayette, Nicole L. Glosson, Simon J. Conway, Nadia Carlesso, Angelo A. Cardoso, Mark H. Kaplan, and Mervin C. Yoder. 2012. "Autonomous Murine T-Cell Progenitor Production in the Extra-Embryonic Yolk Sac before HSC Emergence." *Blood* 119 (24): 5706–14. https://doi.org/10.1182/blood-2011-12-397489.

Zhao, Shizheng, Shachuan Feng, Ye Tian, and Zilong Wen. 2022. "Hemogenic and Aortic Endothelium Arise from a Common Hemogenic Angioblast Precursor and Are Specified by the Etv2 Dosage." *Proceedings of the National Academy of Sciences* 119 (13): e2119051119. https://doi.org/10.1073/pnas.2119051119.

Zhu, Qin, Peng Gao, Joanna Tober, Laura Bennett, Changya Chen, Yasin Uzun, Yan Li, et al. 2020. "Developmental Trajectory of Prehematopoietic Stem Cell Formation from Endothelium." *Blood* 136 (7): 845–56. https://doi.org/10.1182/blood.2020004801.

2128 ## Supplementary files

2129

2130 **Supplementary file 1**: Materials and Methods - Supplementary Table

2131

2132

2133 **Figure 1 – video 1. EHT pol+ cells at early timing.** Z-stack (37 planes) corresponding to the
2134 time point t = 0 min whose plane 21 is shown ***Figure 1C***.

2135

2136 **Figure 1 – video 2. EHT pol+ cells at late timing.** Z-stack (37 planes) corresponding to the
2137 time point t = 80 min whose planes 16 (for eht cell 1) and 22 (for eht cell 2) are shown ***Figure***
2138 ***1 – figure supplement 1B.***

2139

2140 **Figure 1 – video 3. Emergence of EHT pol- cells.** Time-lapse sequence using a
2141 *Tg(Kdrl:Gal4;UAS:RFP;4xNR:eGFP-Podxl2)* embryo, obtained with spinning disk confocal
2142 microscopy (38 timing points, each acquired with 10 min intervals, starting at 55 hpf) and from
2143 which the images of the 2 emerging EHT pol- cells shown Figure 1D were extracted.

2144

Figure 1

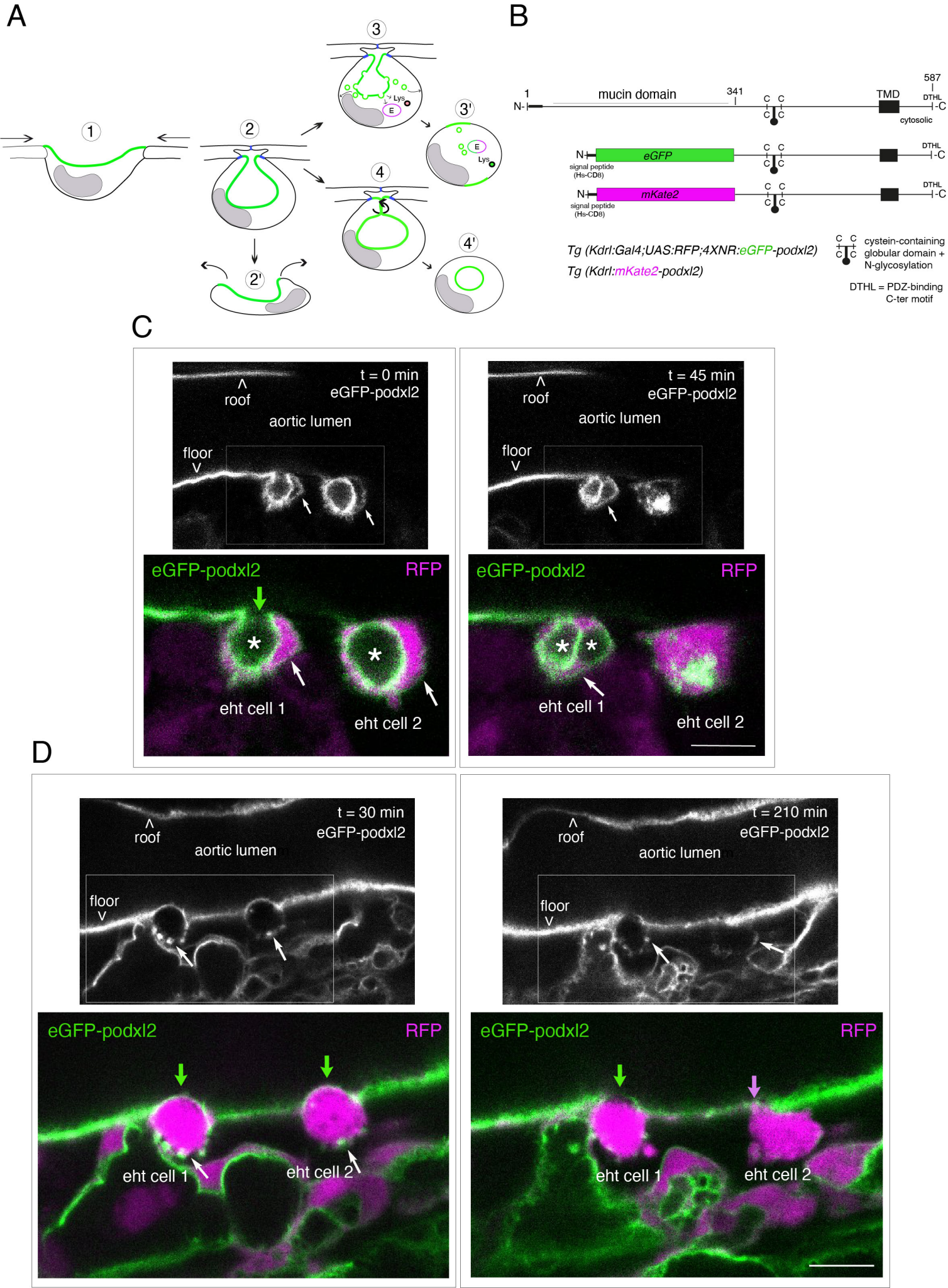
A
1
2
2'
3
3'
4
4'
Lys
E
B
1
mucin domain
341
TMD
587
DTHL
N-
-C
cytosolic
eGFP
mKate2
signal peptide
(Hs-CD8)
Tg (Kdrl:Gal4;UAS:RFP;4XNR:eGFP-podxl2)
Tg (Kdrl:mKate2-podxl2)
cystein-containing
globular domain +
N-glycosylation
DTHL = PDZ-binding
C-ter motif
C
t = 0 min
eGFP-podxl2
roof
aortic lumen
floor
t = 45 min
eGFP-podxl2
RFP
eht cell 1
eht cell 2
D
t = 30 min
t = 210 min

FIGURE 1 - figure supplement 1

A

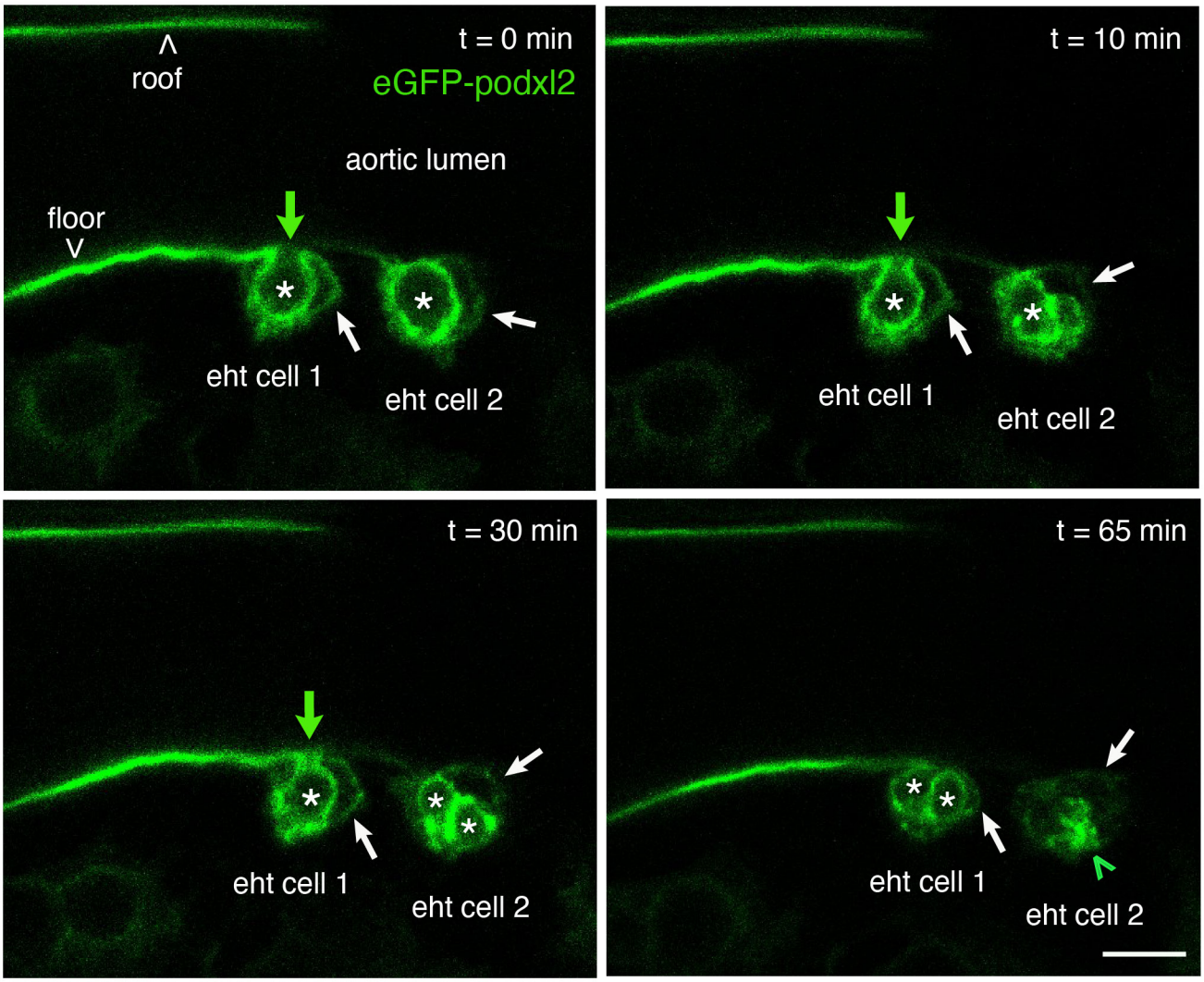

B

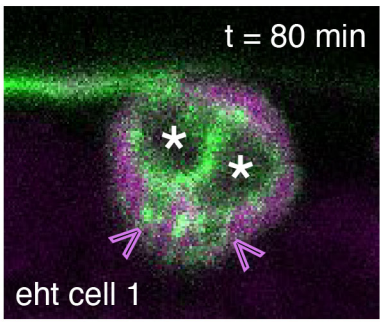

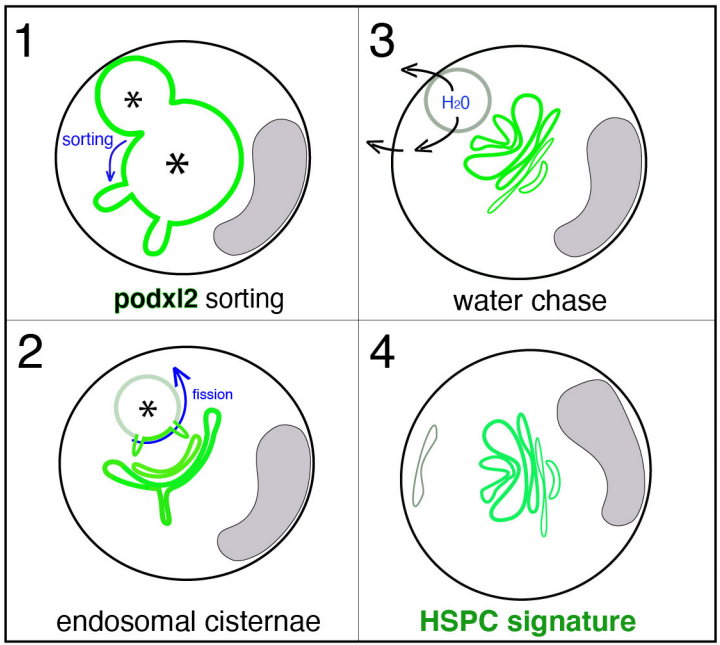

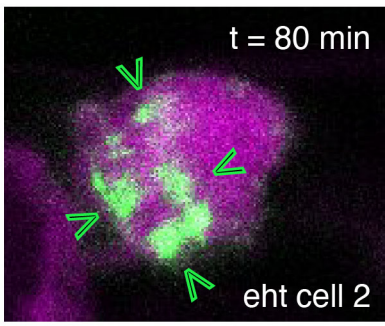

Figure 2

A

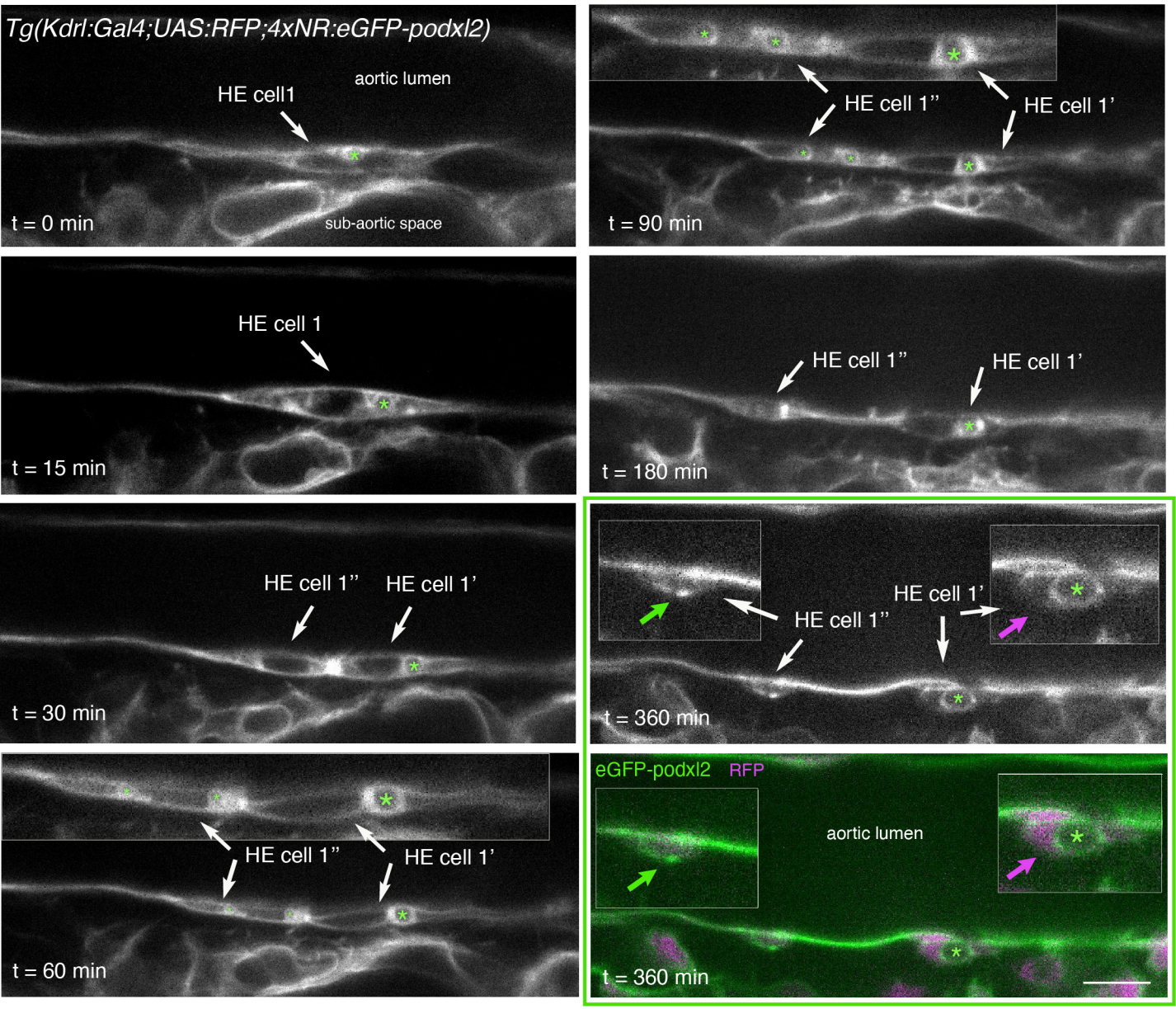
Tg(Kdrl:Gal4;UAS:RFP;4xNR:eGFP-podxl2)
aortic lumen
HE cell1
sub-aortic space
t = 0 min
HE cell 1''
HE cell 1'
t = 90 min
HE cell 1
t = 15 min
HE cell 1''
HE cell 1'
t = 180 min
HE cell 1''
HE cell 1'
t = 30 min
HE cell 1'
HE cell 1''
t = 360 min
HE cell 1''
HE cell 1'
t = 60 min
eGFP-podxl2
RFP
aortic lumen
t = 360 min

B

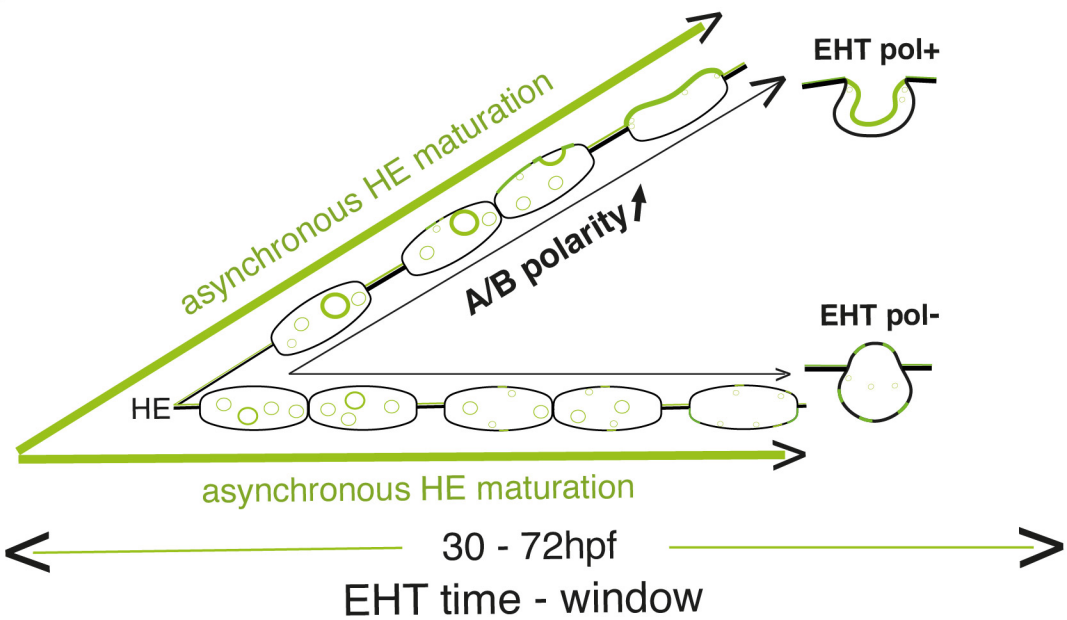
asynchronous HE maturation
EHT pol+
A/B polarity
EHT pol-
HE
asynchronous HE maturation
30 - 72hpf
EHT time - window

Figure 2
- figure supplement 1

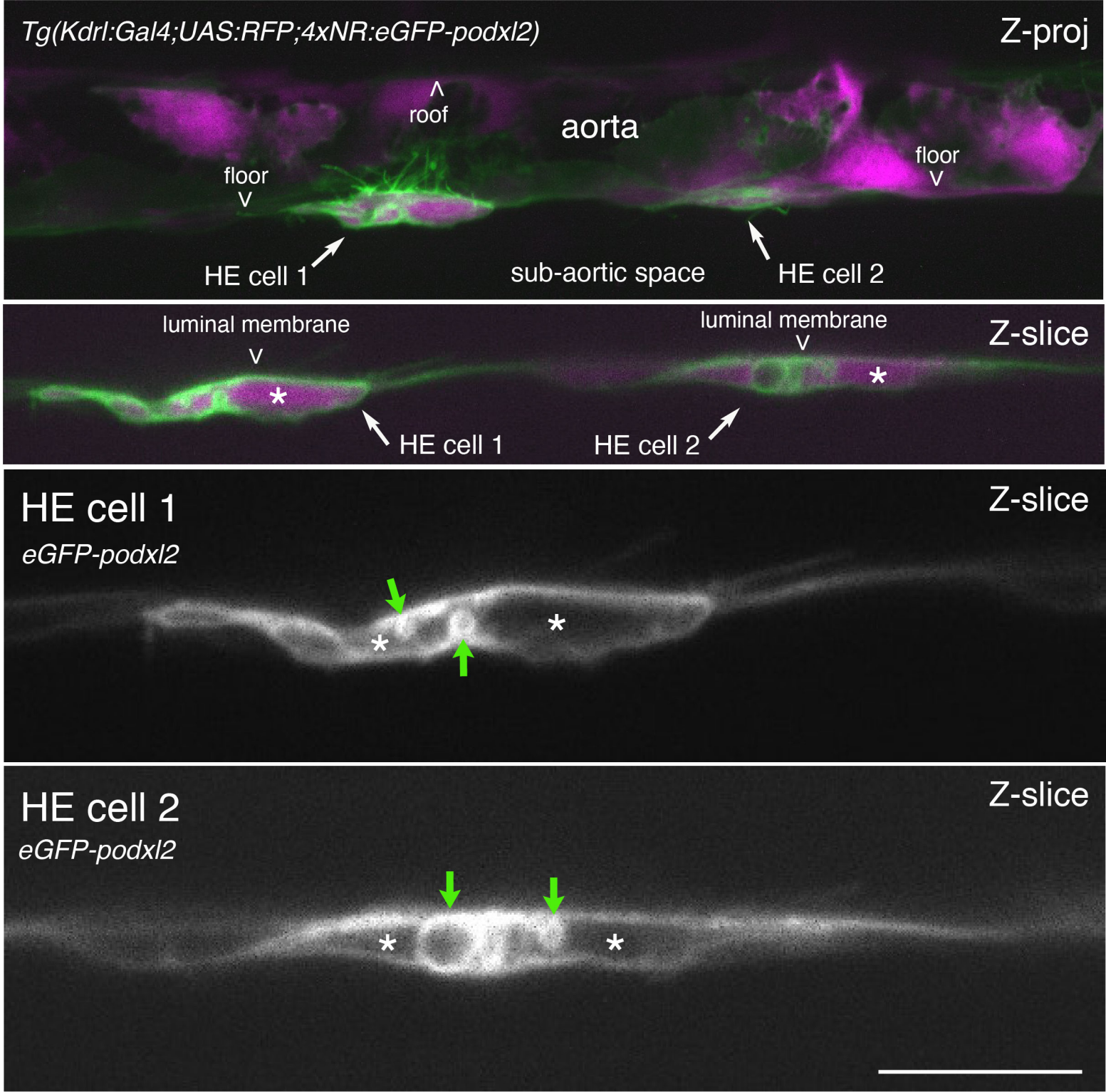

Figure 2 - figure supplement 2

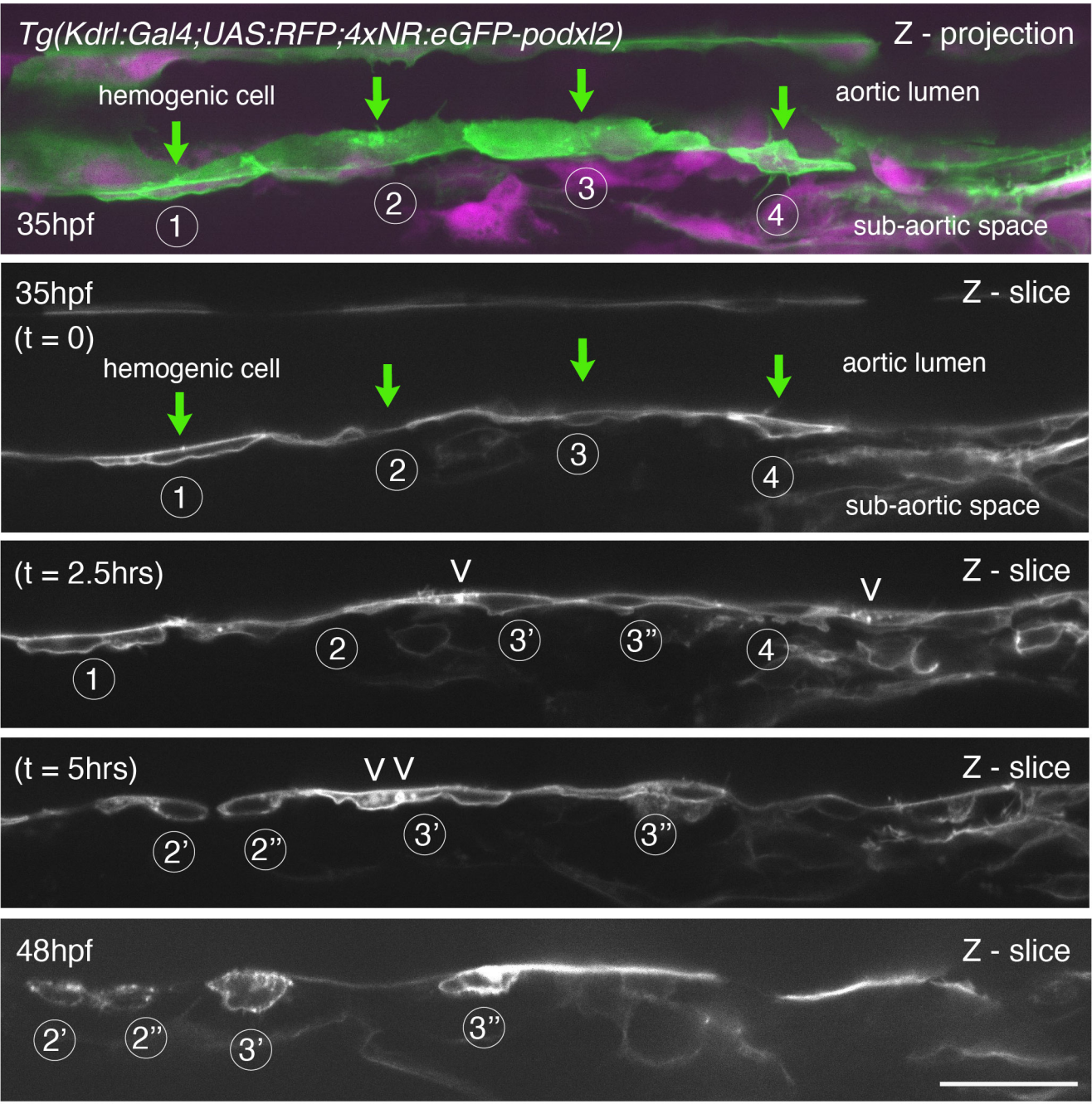

Figure 3

A

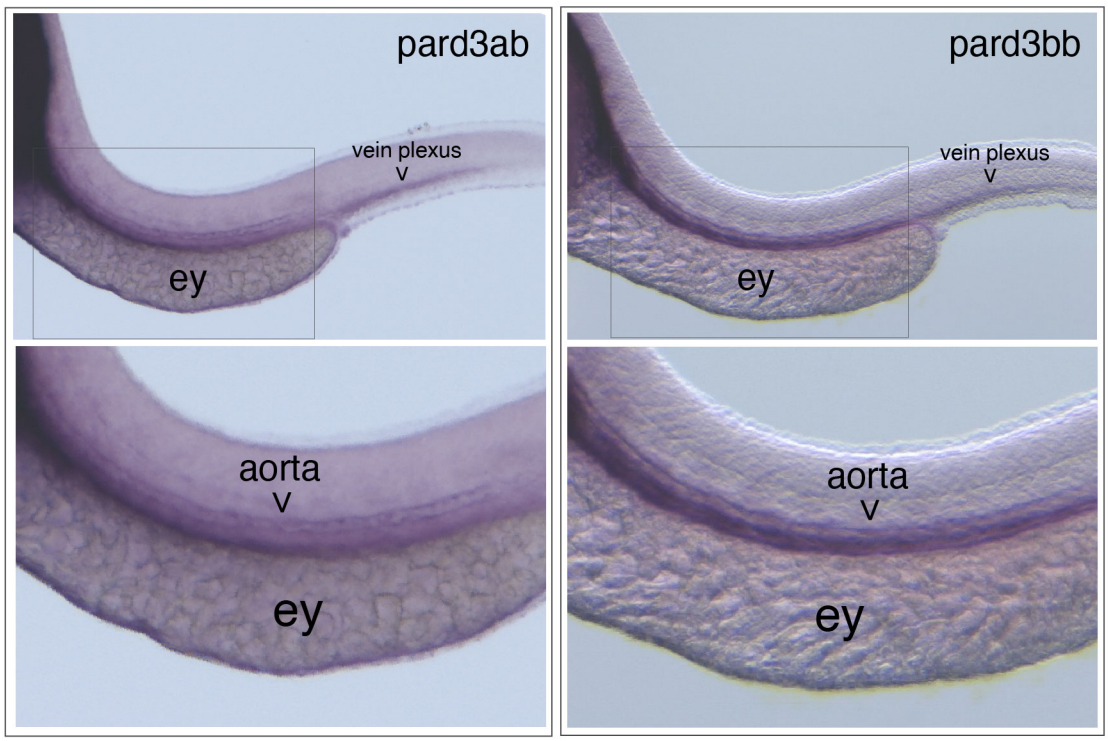

B

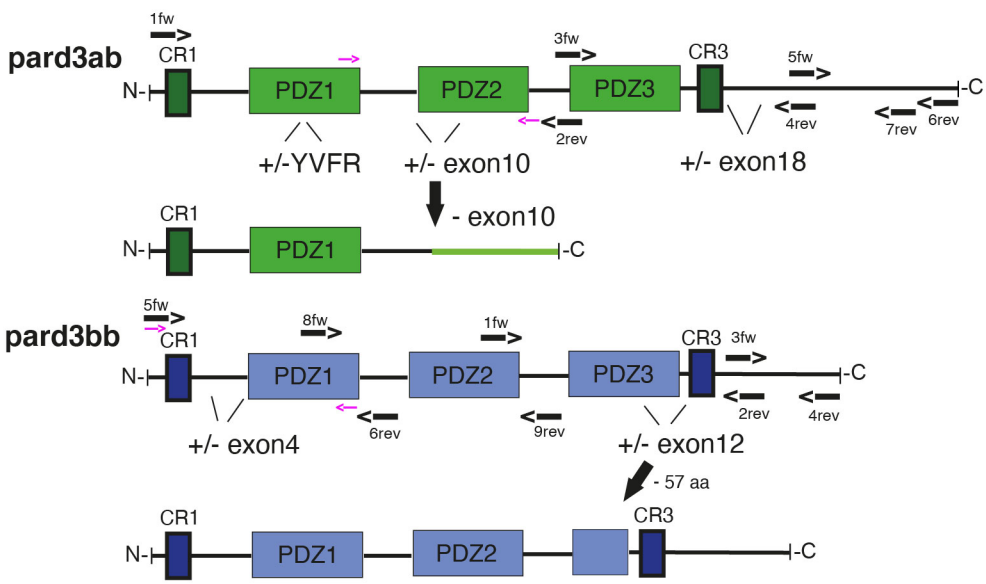

C

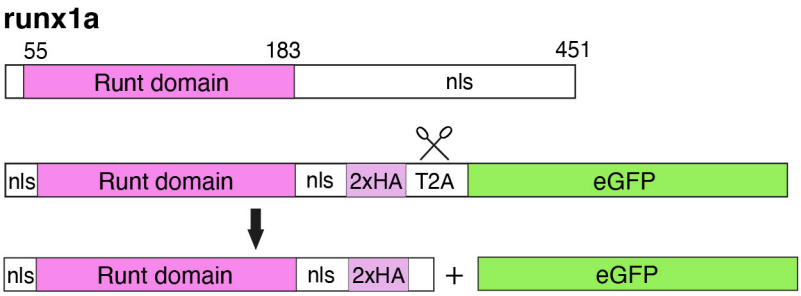

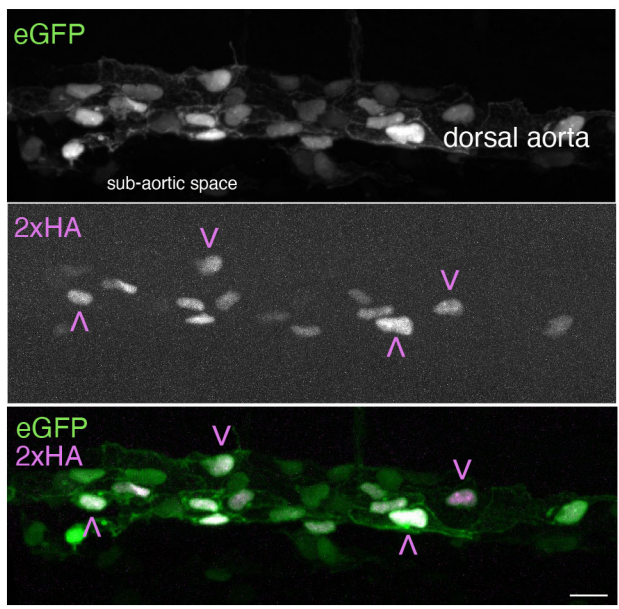

Bar = 25 μm

Figure 3 - figure supplement 1

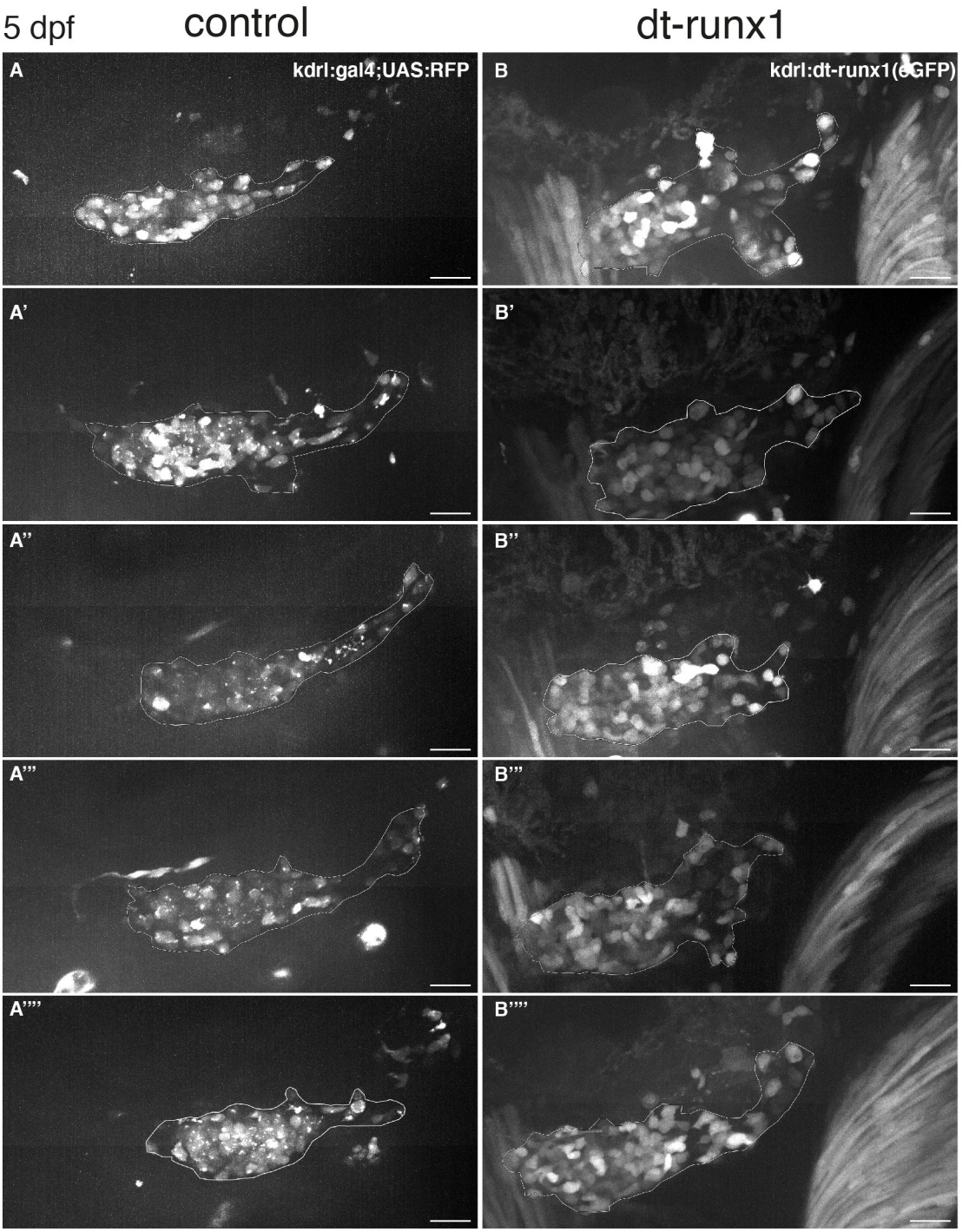

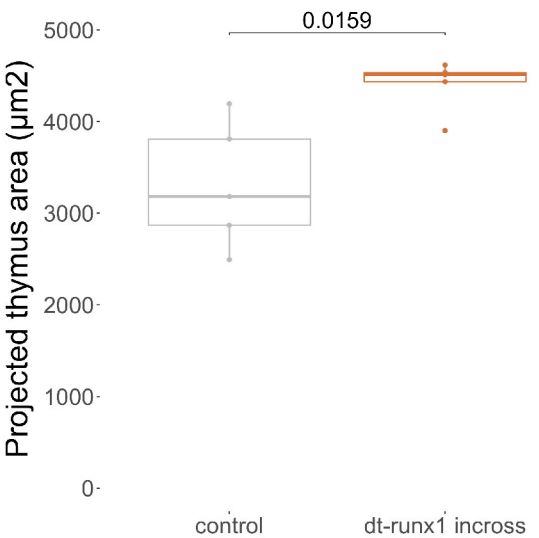

Figure 3 - figure supplement 2

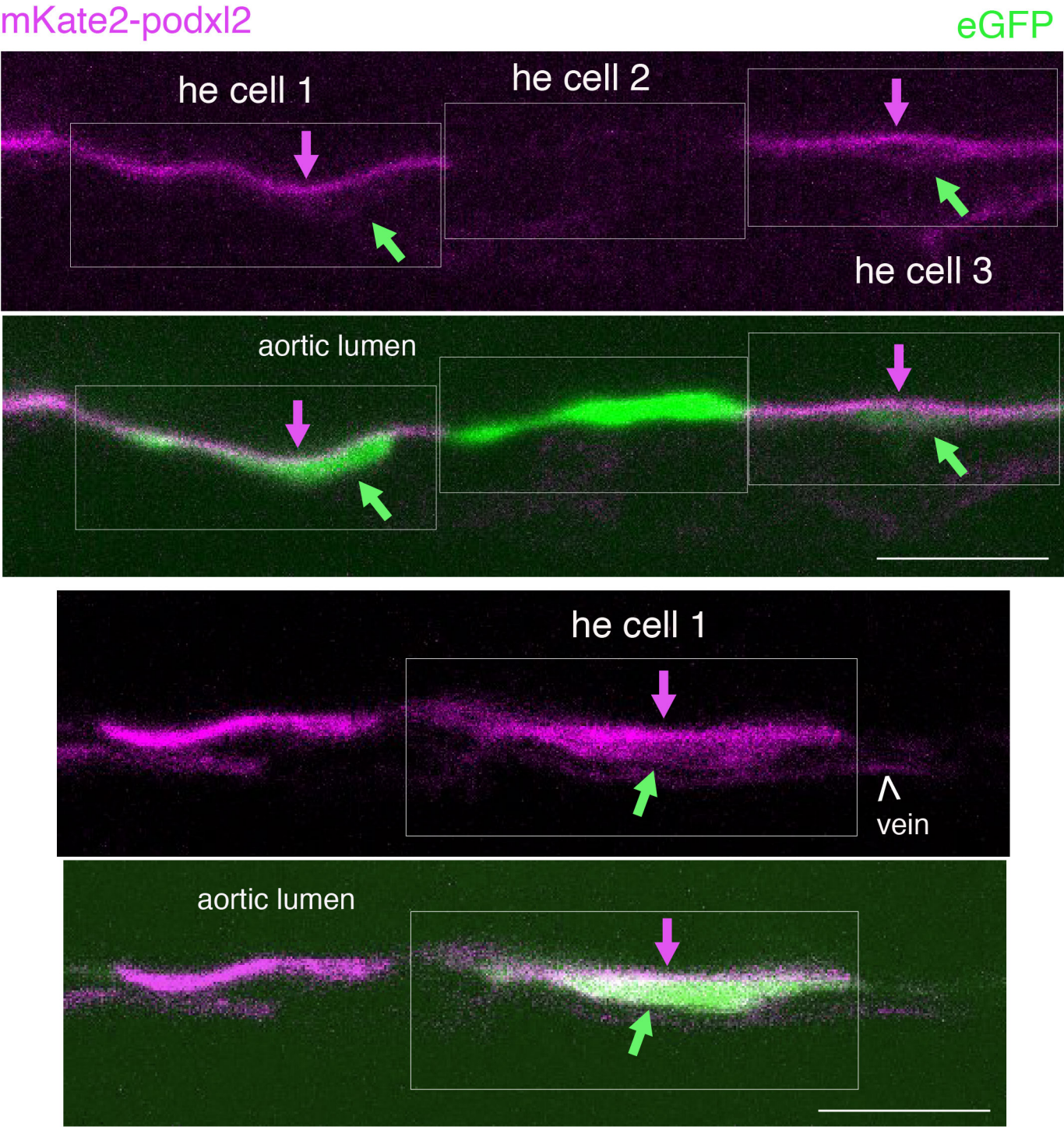

Figure 3 - figure supplement 3

A

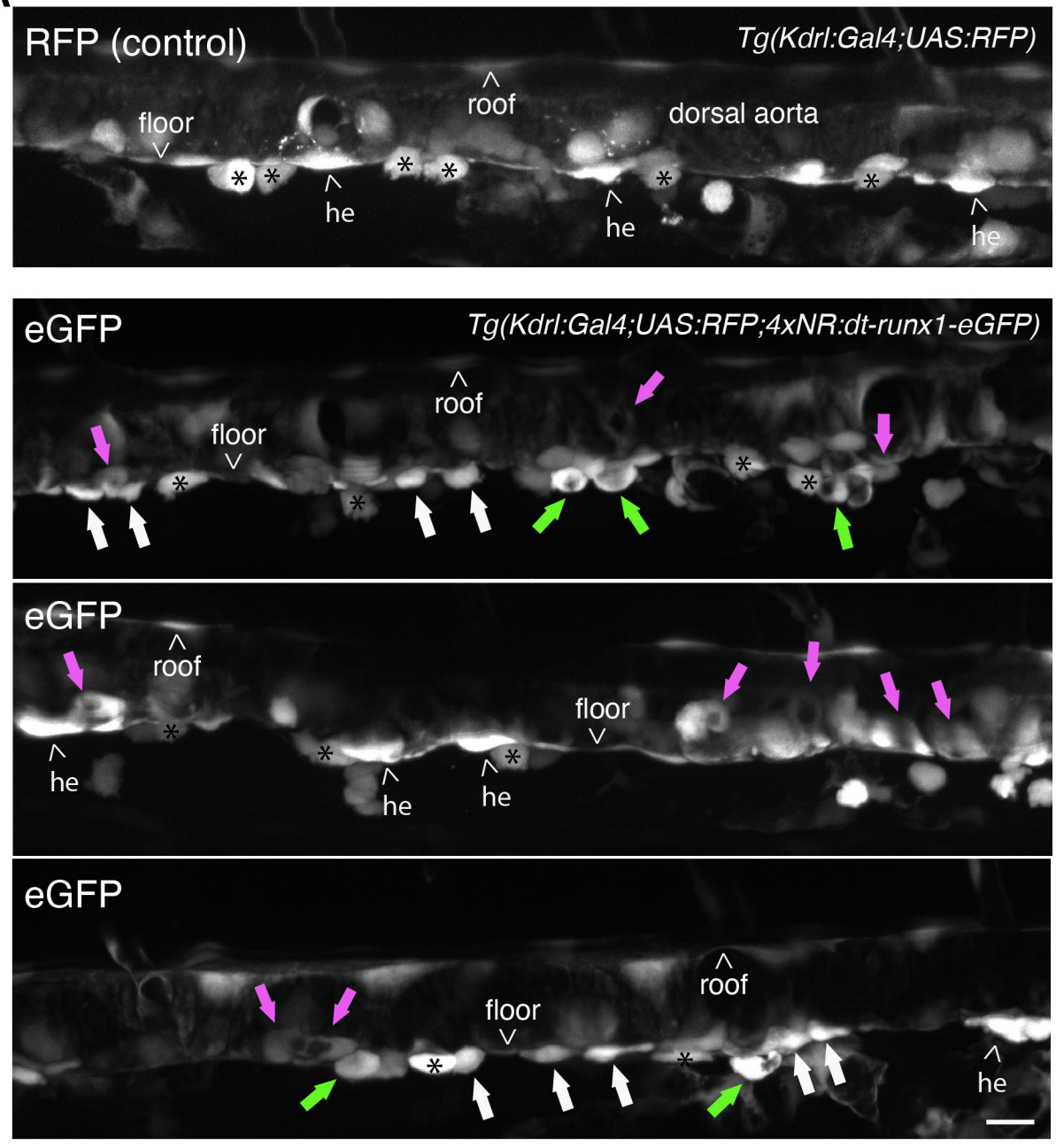

B

Tg(kdrl:mKate2-podxl2)x(kdrl:Gal4;4xNR:dt-runx1-eGFP)

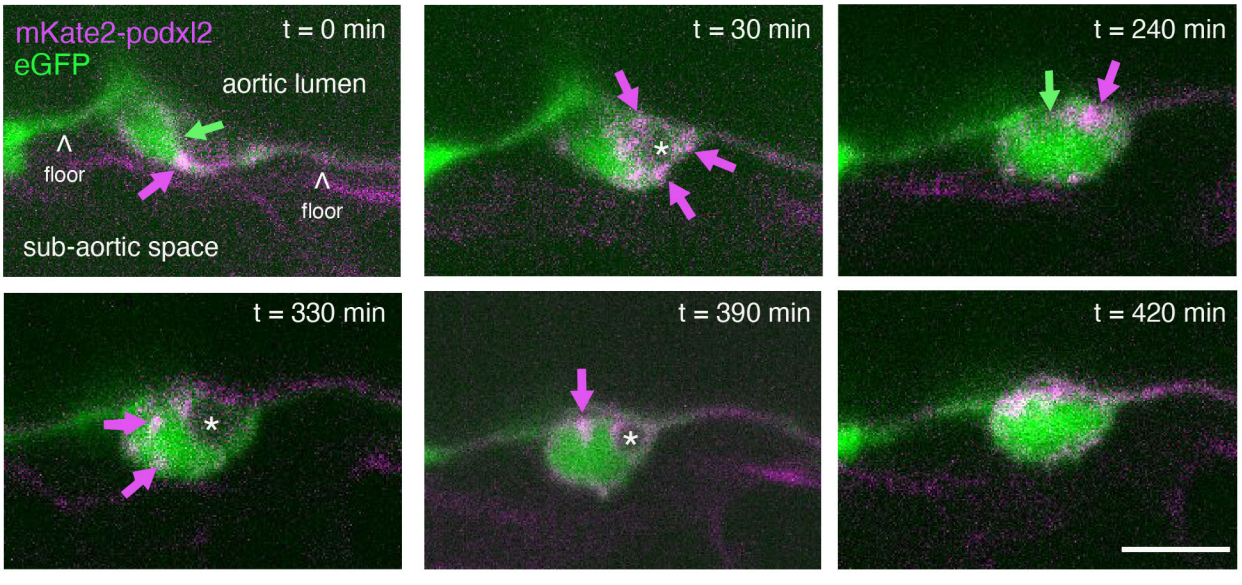

Figure 4

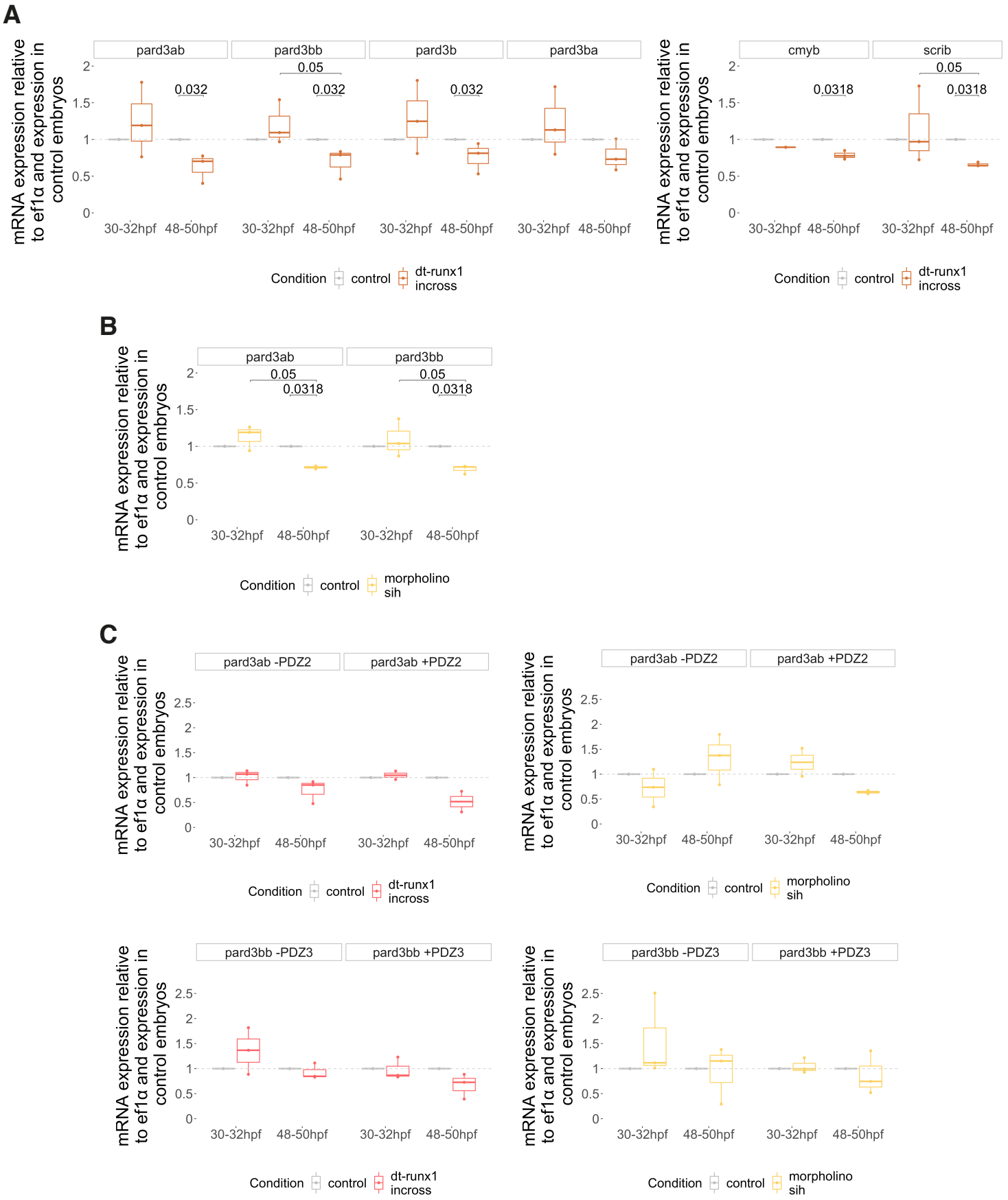
A
pard3ab
pard3bb
pard3b
pard3ba
0.05
0.032
0.032
0.032
mRNA expression relative to ef1α and expression in control embryos
30-32hpf
48-50hpf
Condition
control
dt-runx1 incross
cmyb
scrib
0.05
0.0318
0.0318
B
pard3ab
pard3bb
0.05
0.0318
0.05
0.0318
morpholino sih
C
pard3ab -PDZ2
pard3ab +PDZ2
pard3bb -PDZ3
pard3bb +PDZ3

Figure 5

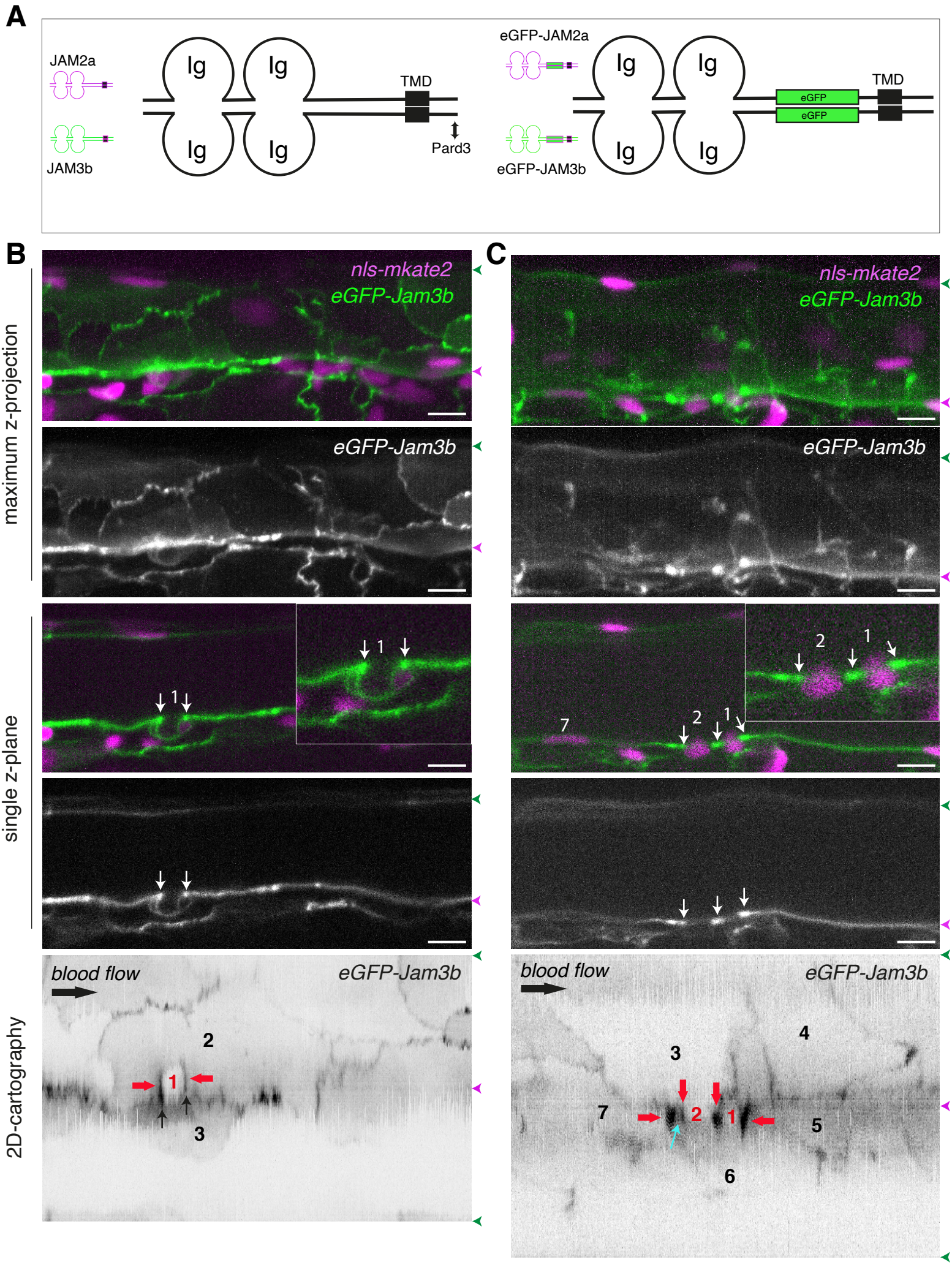
A
JAM2a
JAM3b
Ig
Ig
Ig
Ig
TMD
Pard3
eGFP-JAM2a
eGFP-JAM3b
eGFP
eGFP
TMD
B
C
maximum z-projection
single z-plane
2D-cartography
nls-mkate2
eGFP-Jam3b
eGFP-Jam3b
blood flow
eGFP-Jam3b
1
2
3
4
5
6
7

Figure 5 - figure supplement 1

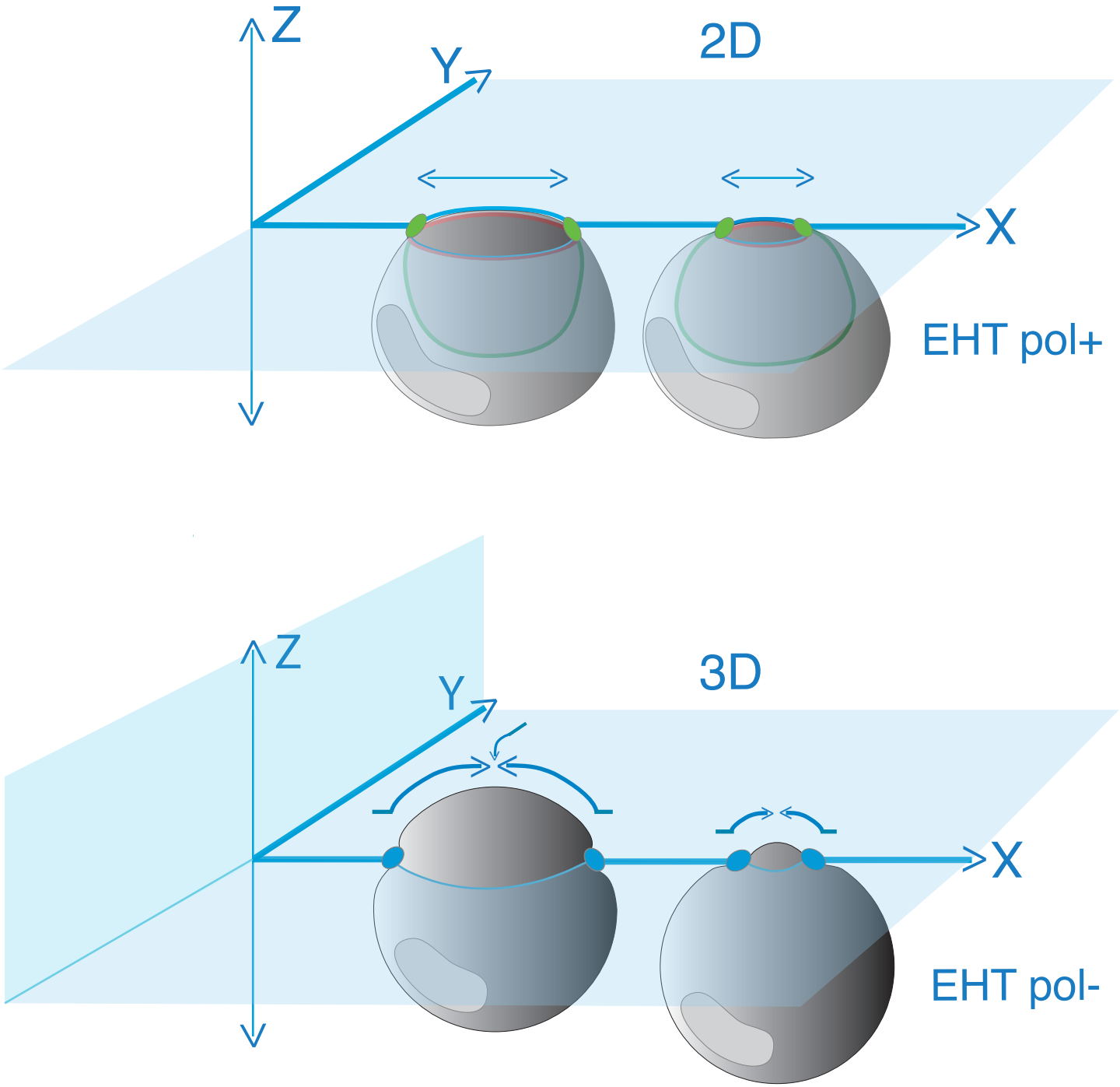

Figure 5 - figure supplement 2

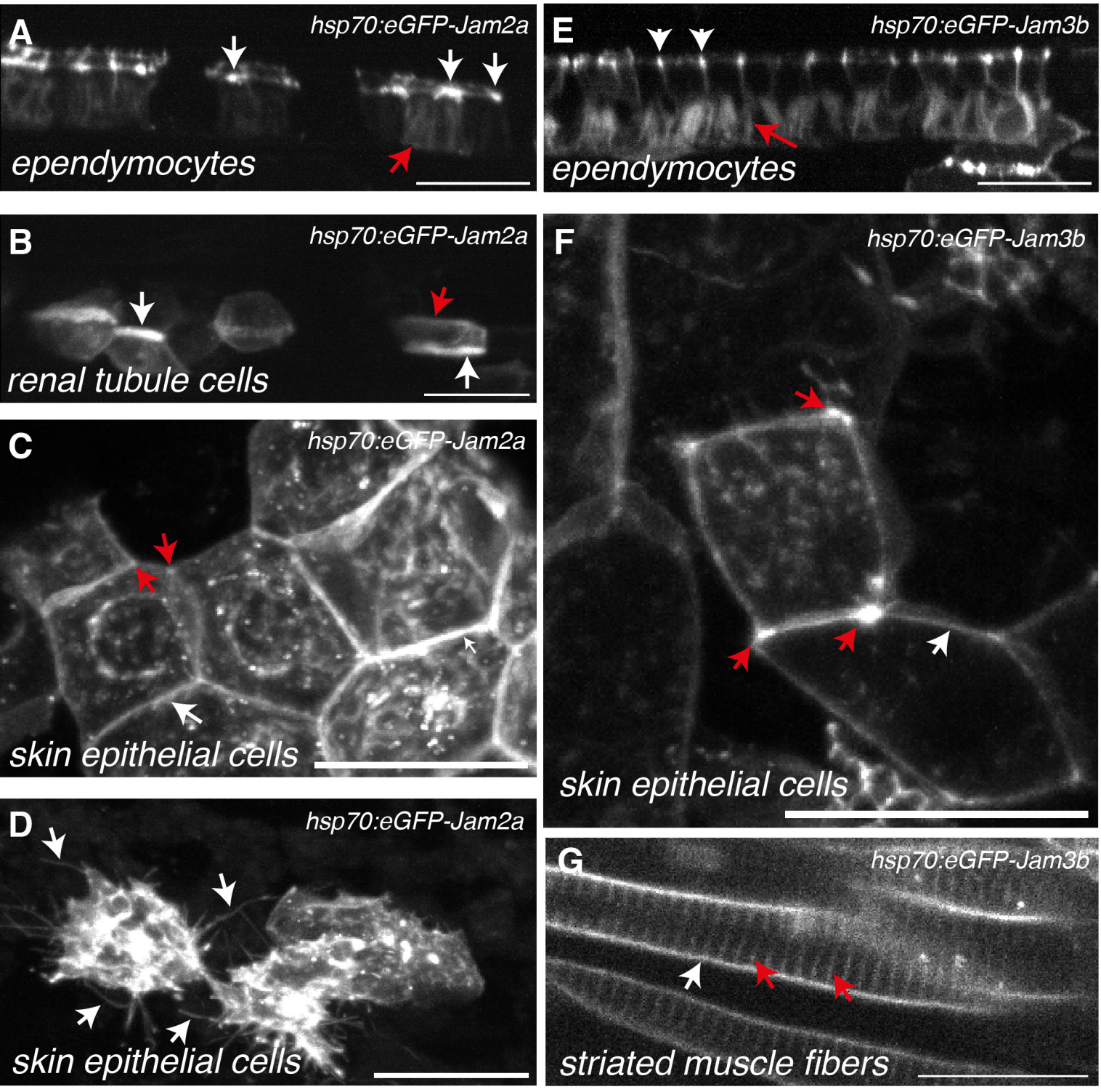

Figure 6

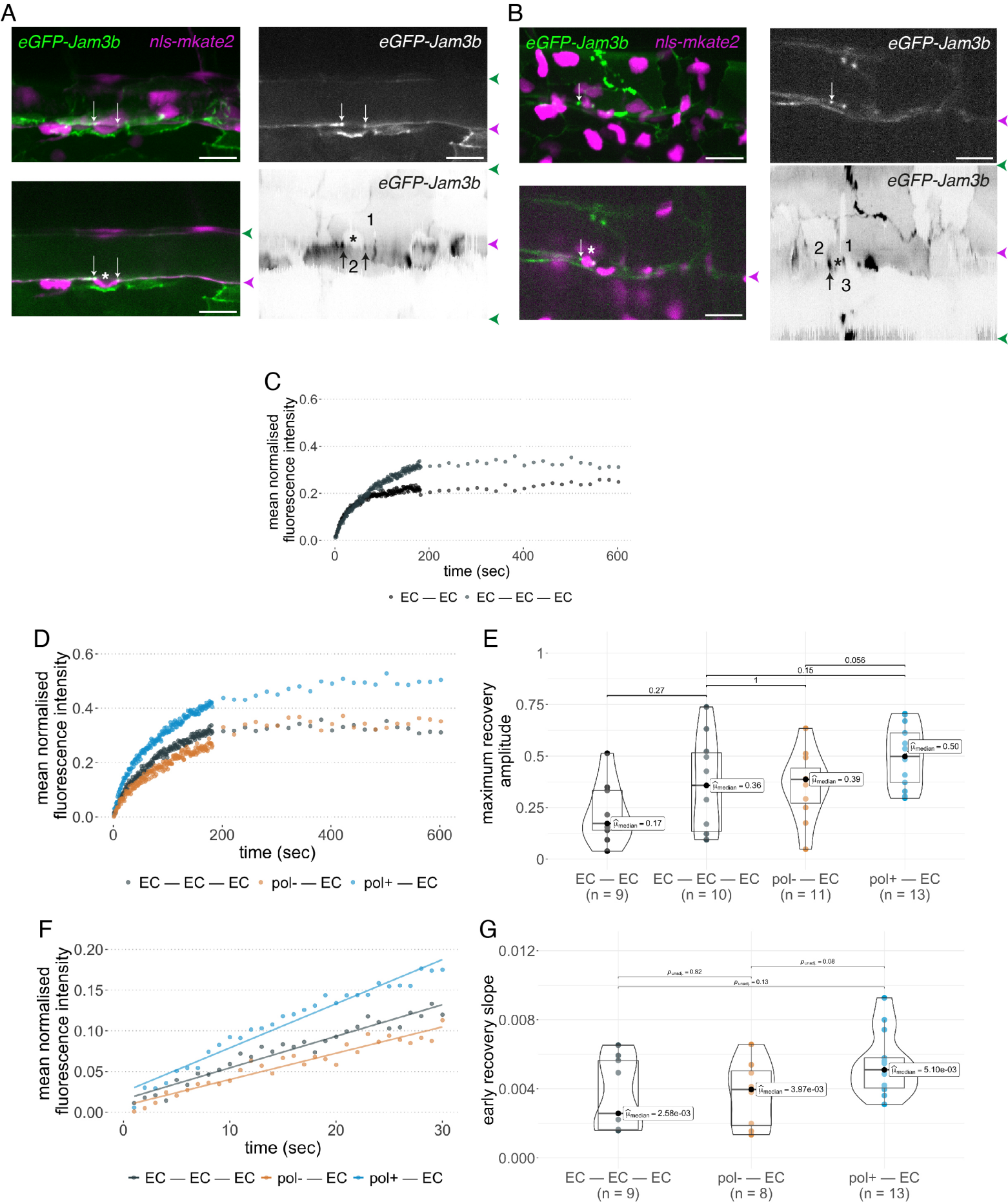
A
eGFP-Jam3b
nls-mkate2
eGFP-Jam3b
eGFP-Jam3b
1
2
B
eGFP-Jam3b
nls-mkate2
eGFP-Jam3b
eGFP-Jam3b
2
1
3
C
mean normalised fluorescence intensity
time (sec)
EC — EC
EC — EC — EC
D
mean normalised fluorescence intensity
time (sec)
EC — EC — EC
pol- — EC
pol+ — EC
E
maximum recovery amplitude
0.27
1
0.15
0.056
EC — EC (n = 9)
EC — EC — EC (n = 10)
pol- — EC (n = 11)
pol+ — EC (n = 13)
F
mean normalised fluorescence intensity
time (sec)
EC — EC — EC
pol- — EC
pol+ — EC
G
early recovery slope
EC — EC — EC (n = 9)
pol- — EC (n = 8)
pol+ — EC (n = 13)

Figure 6 - figure supplement 1

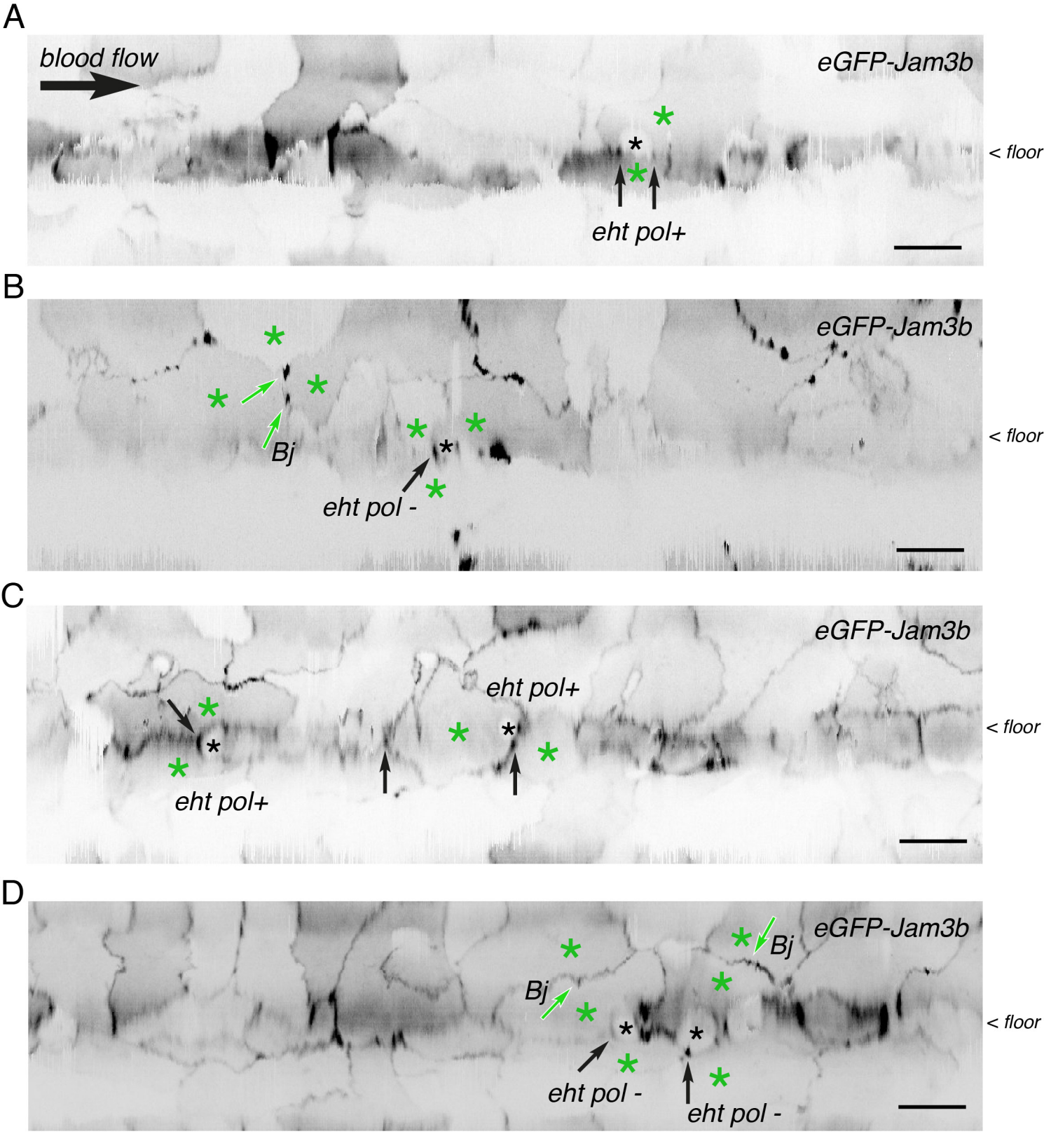

Figure 7

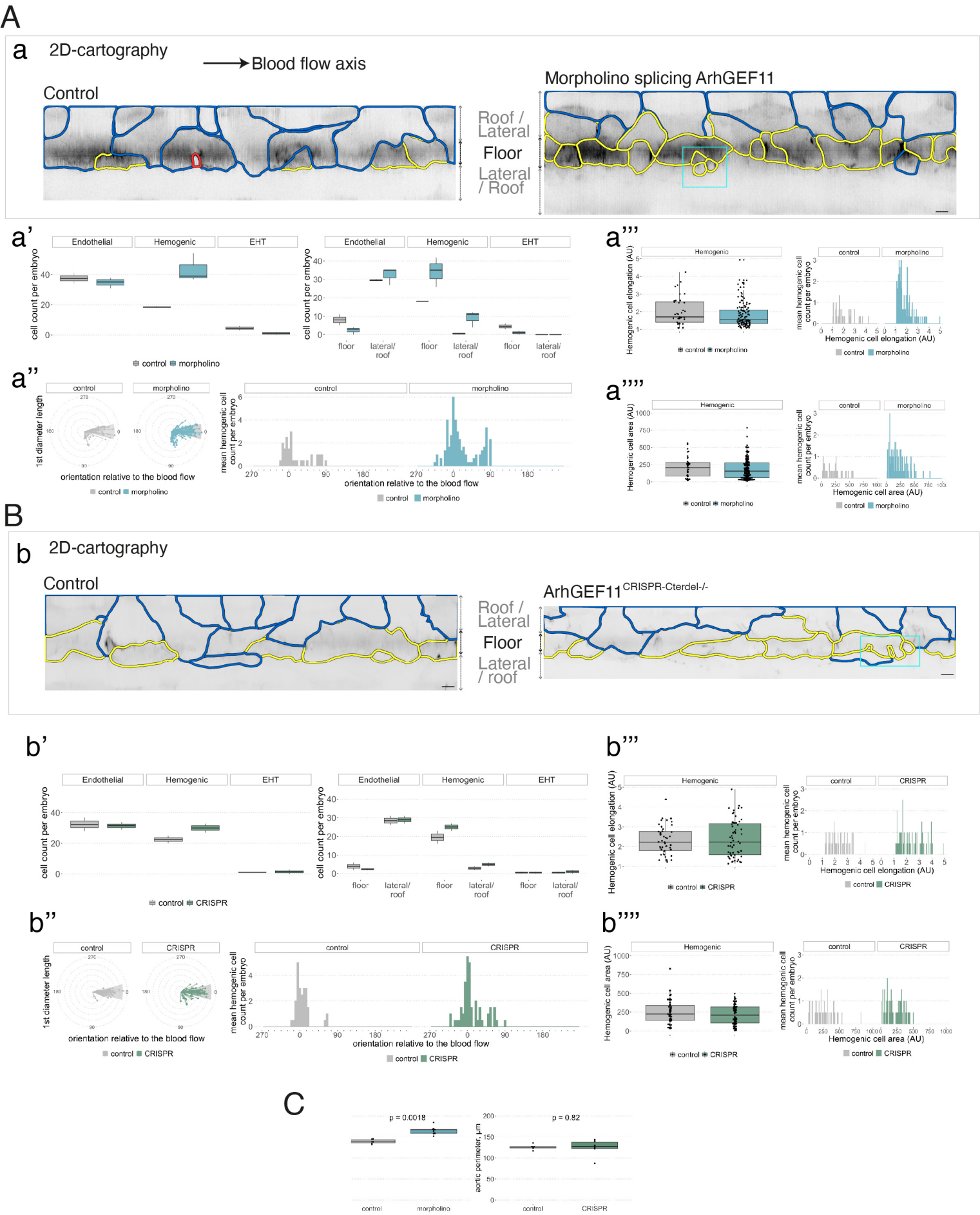
A
a
2D-cartography
Blood flow axis
Control
Morpholino splicing ArhGEF11
Roof / Lateral
Floor
Lateral / Roof
a'
Endothelial
Hemogenic
EHT
cell count per embryo
control
morpholino
floor
lateral/ roof
a''
1st diameter length
orientation relative to the blood flow
mean hemogenic cell count per embryo
a'''
Hemogenic cell elongation (AU)
a''''
Hemogenic cell area (AU)
B
b
2D-cartography
Control
ArhGEF11CRISPR-Cterdel-/-
Roof / Lateral
Floor
Lateral / roof
b'
CRISPR
b''
b'''
b''''
C
p = 0.0018
p = 0.82
aortic perimeter, µm

Figure 7 - figure supplement 1

A

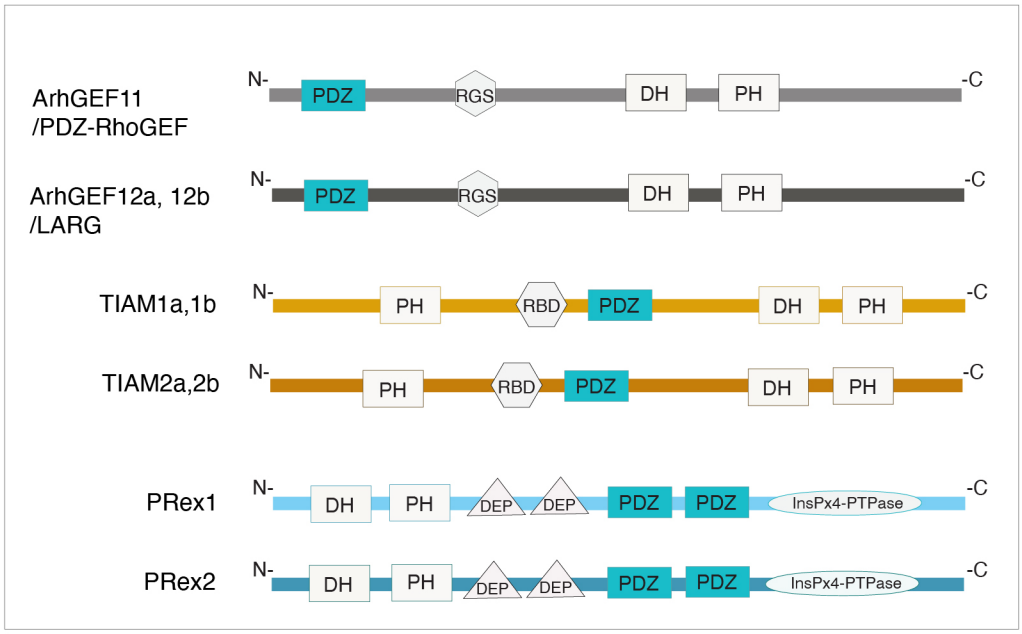

B

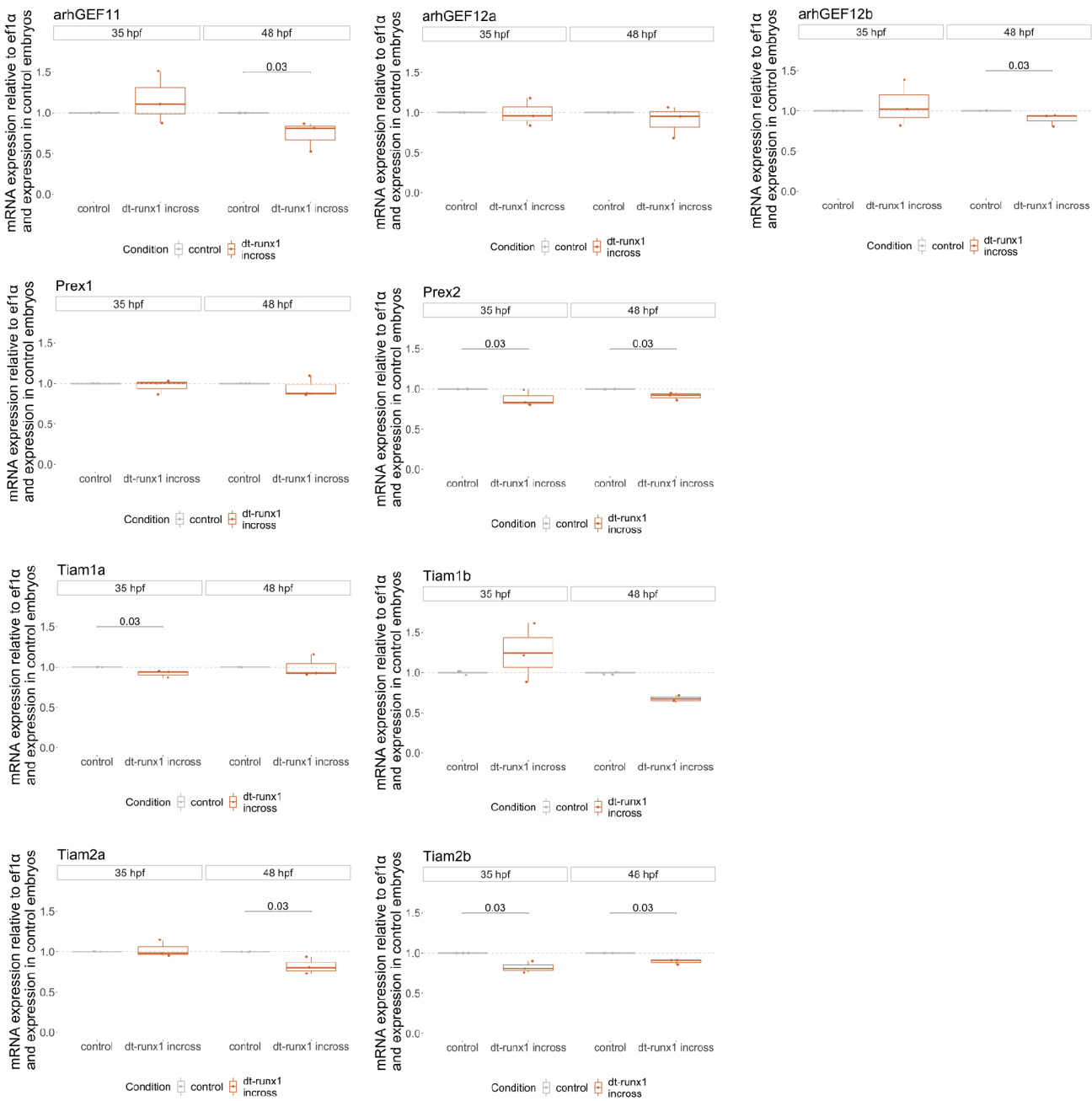

Figure 7 - figure supplement 2

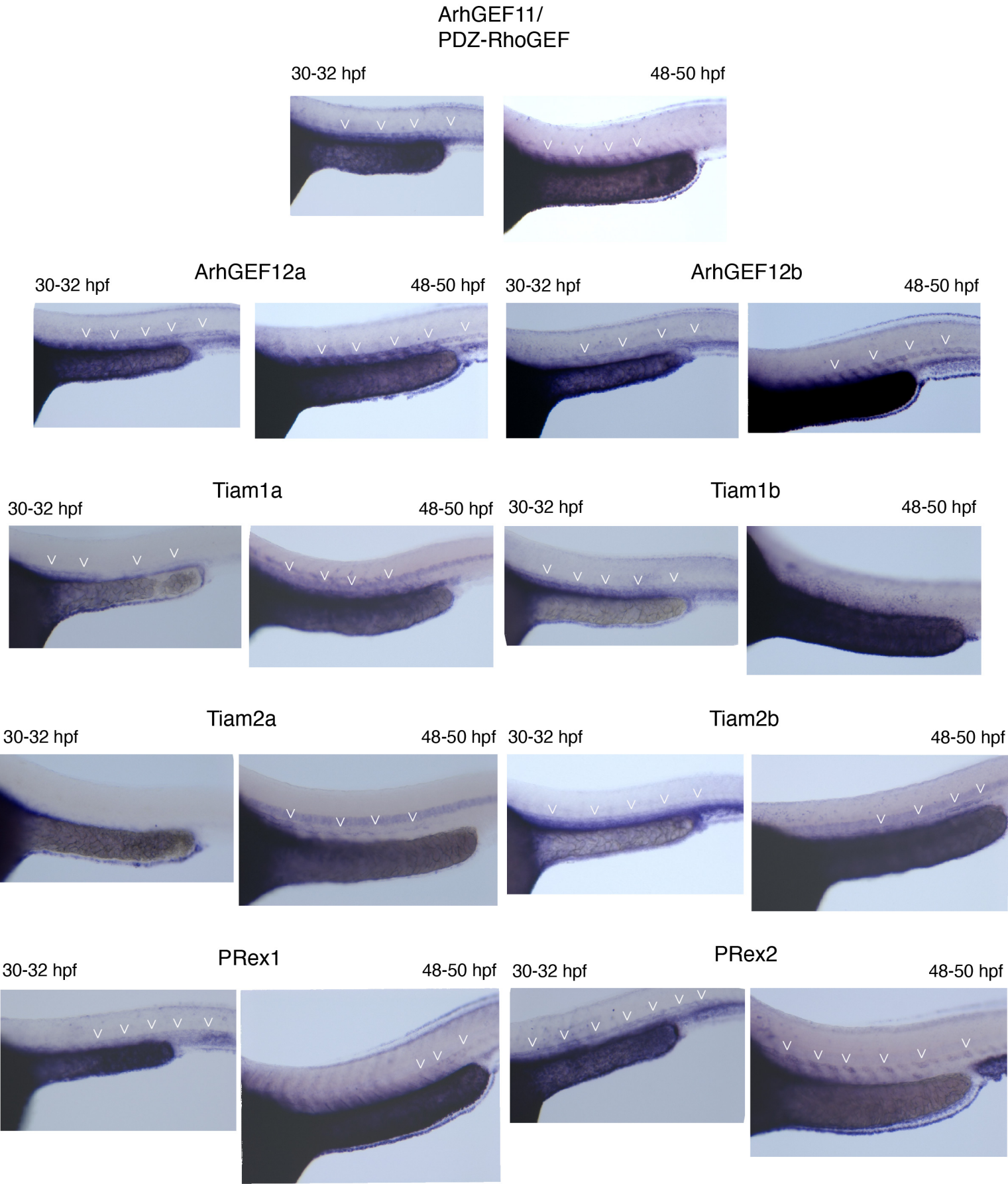

Figure 7 - figure supplement 3

A

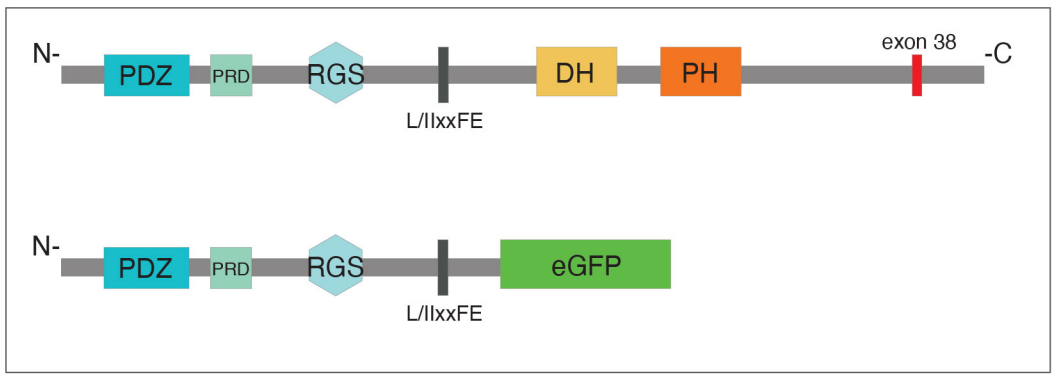

B

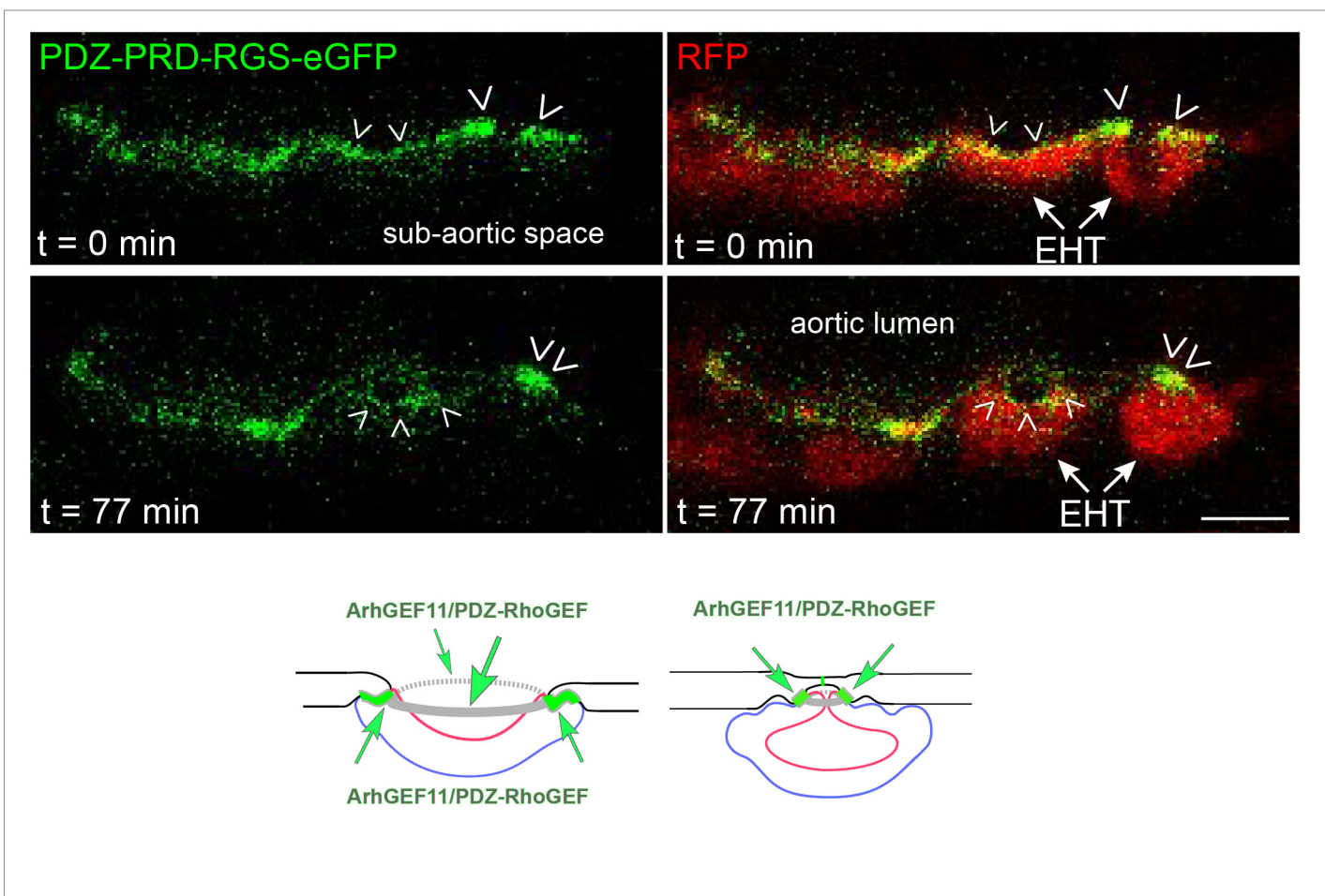

Figure 7 - figure supplement 4

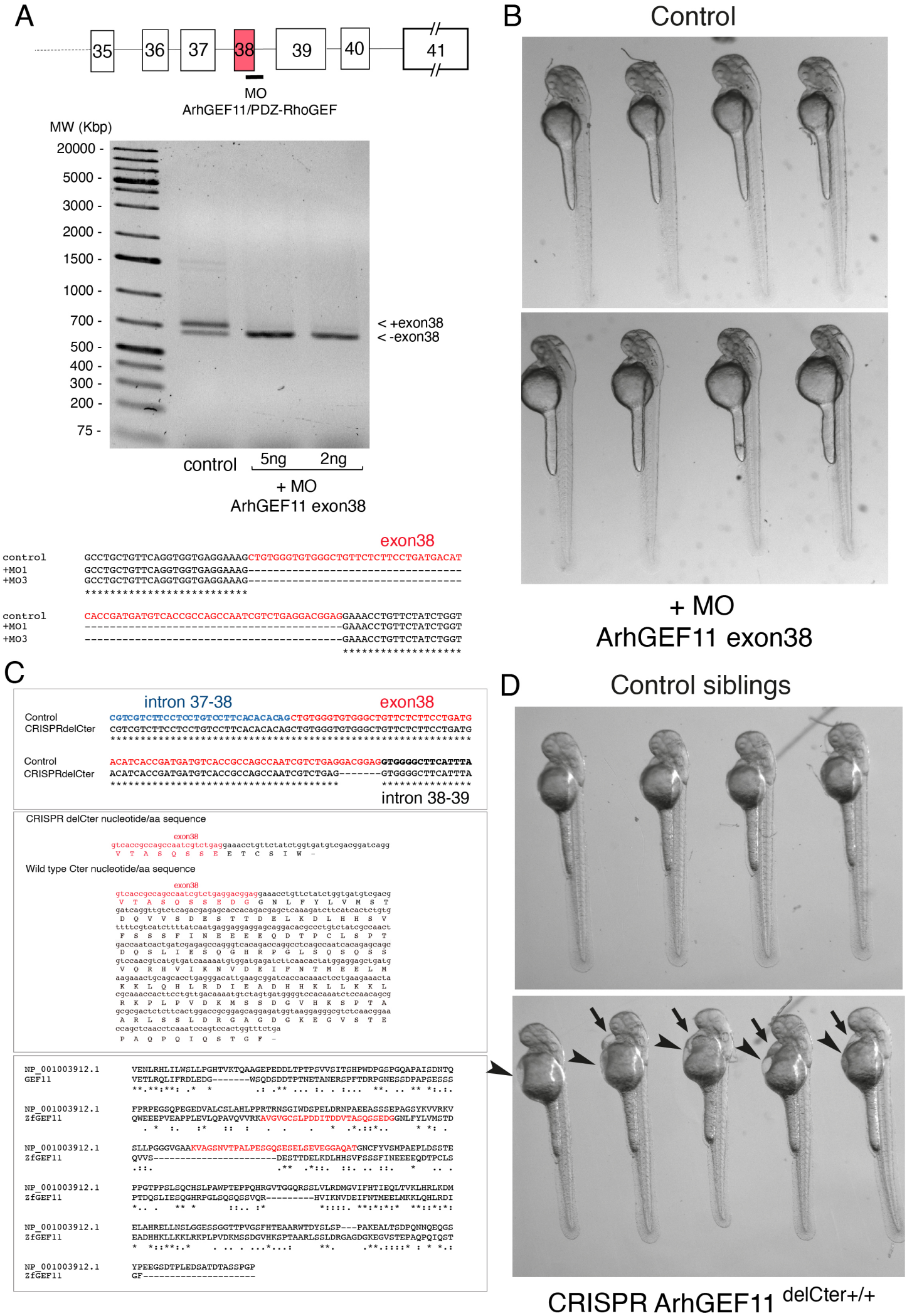

Figure 7 - supplemental 5

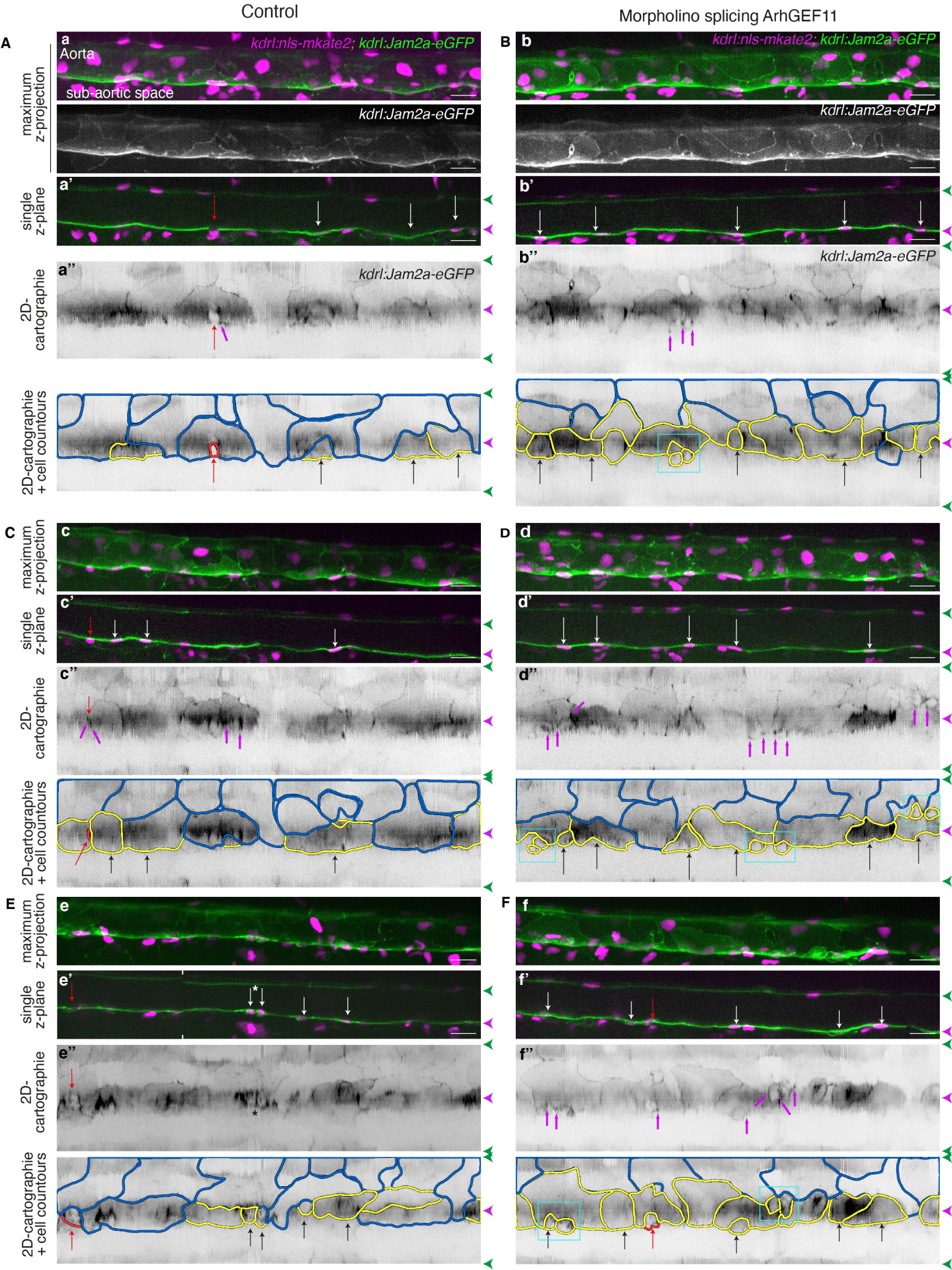

Figure 7 - supplement 6

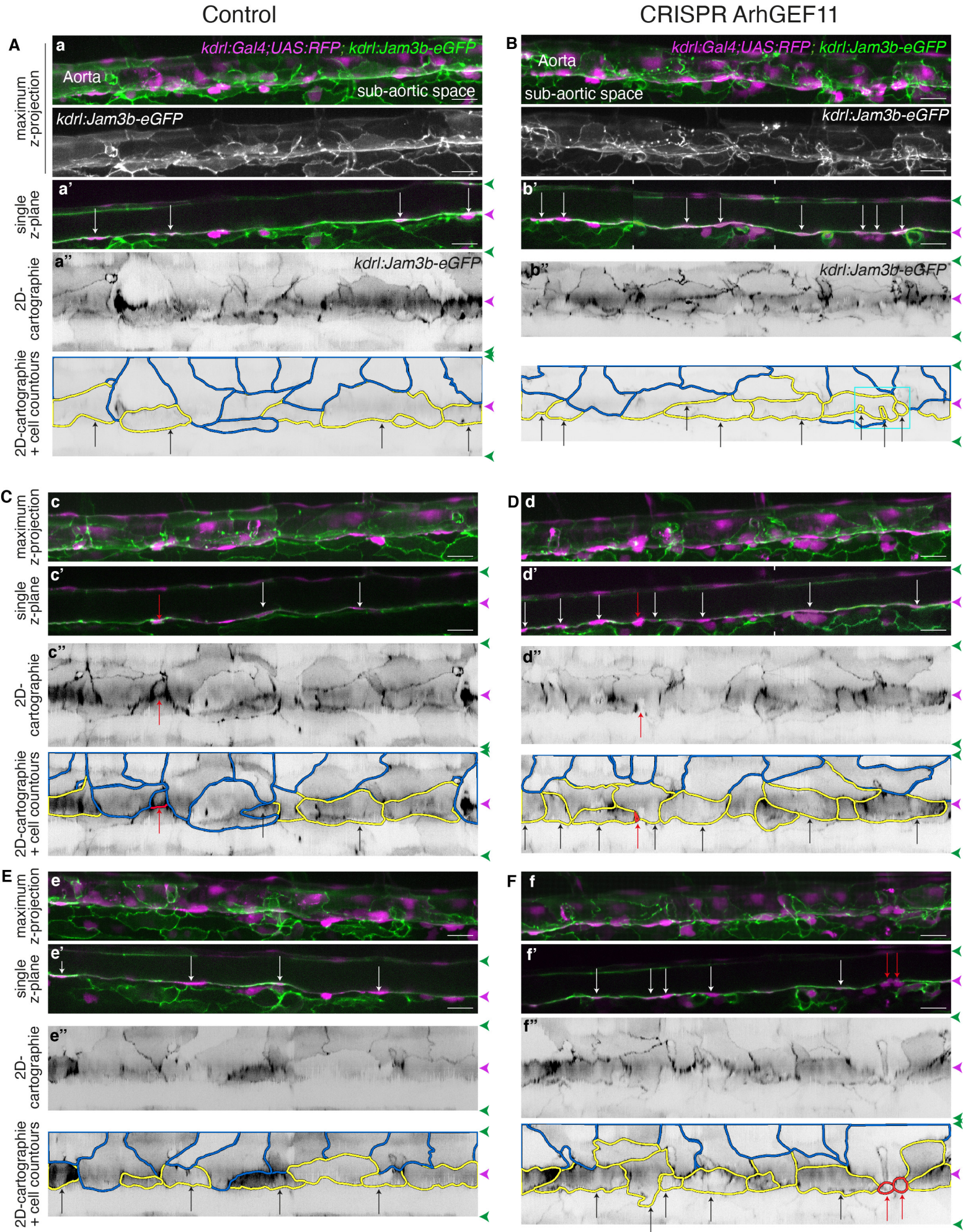

Figure 8

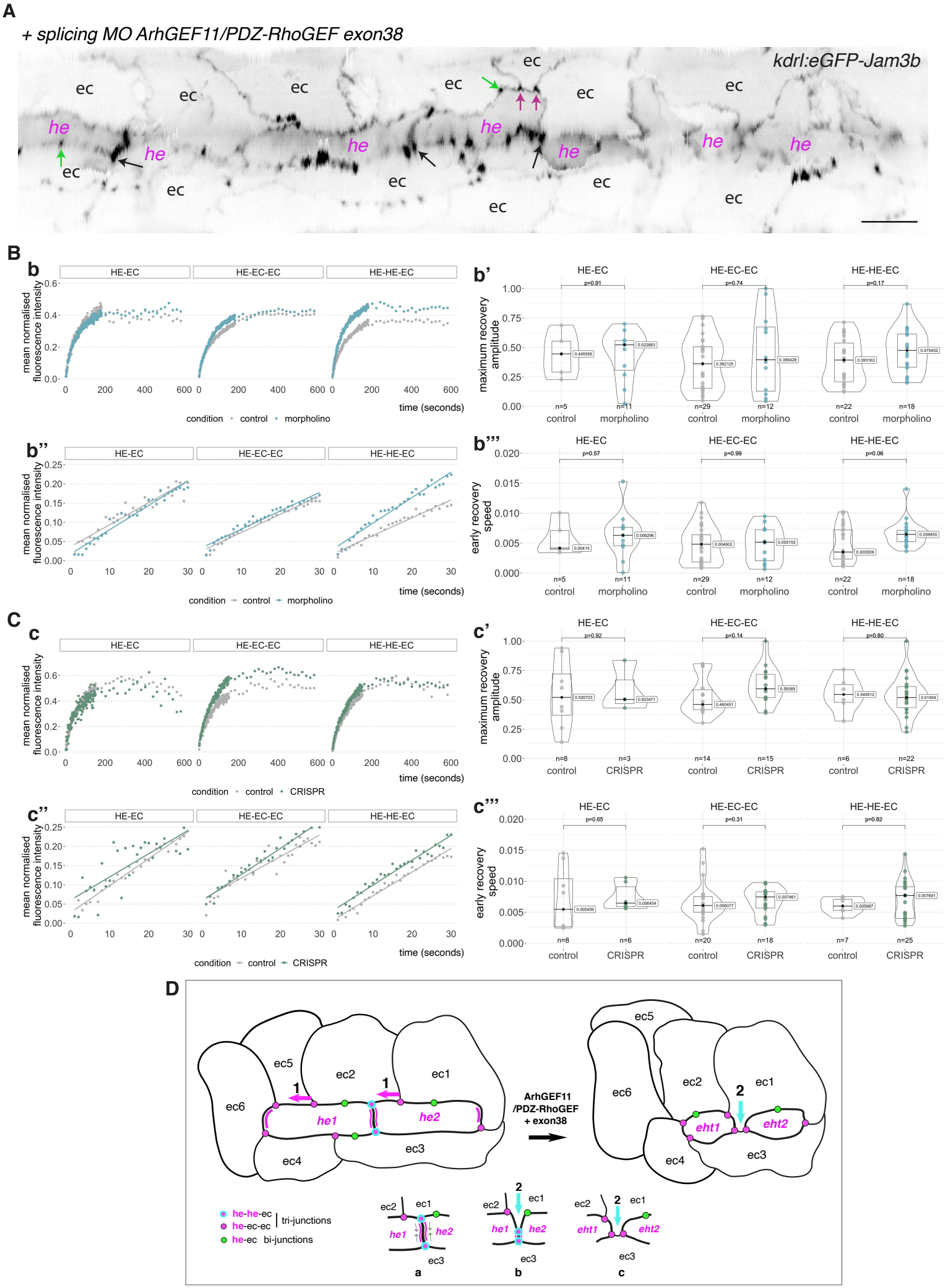
A
+ splicing MO ArhGEF11/PDZ-RhoGEF exon38
kdrl:eGFP-Jam3b
ec
he
B
b
HE-EC
HE-EC-EC
HE-HE-EC
mean normalised fluorescence intensity
time (seconds)
condition control morpholino
b'
maximum recovery amplitude
control
morpholino
b''
b'''
early recovery speed
C
c
condition control CRISPR
c'
c''
c'''
D
ec1
ec2
ec3
ec4
ec5
ec6
he1
he2
eht1
eht2
ArhGEF11 /PDZ-RhoGEF + exon38
he-he-ec
he-ec-ec
tri-junctions
he-ec bi-junctions
a
b
c